

UC Davis

UC Davis Electronic Theses and Dissertations

Title

Applications of Mesoporous Hafnium Oxide for Crude Oil Spill Remediation, and Per-and Polyfluoroalkyl Substances Composting, Adsorption, and Electrochemical Oxidation

Permalink

<https://escholarship.org/uc/item/8x20k2pr>

Author

Hussain, Fatima Adil

Publication Date

2022

Peer reviewed|Thesis/dissertation

Applications of Mesoporous Hafnium Oxide for Crude Oil Spill Remediation, and Per-and
Polyfluoroalkyl Substances Composting, Adsorption, and Electrochemical Oxidation

By

FATIMA ADIL HUSSAIN
DISSERTATION

Submitted in partial satisfaction of the requirements for the degree of

DOCTOR OF PHILOSOPHY

in

Chemistry

in the

OFFICE OF GRADUATE STUDIES

of the

UNIVERSITY OF CALIFORNIA

DAVIS

Approved:

Jesús M. Velázquez, Chair

William H. Casey

Susan M. Kauzlarich

Committee in Charge

2022

بِسْمِ اللَّهِ الرَّحْمَنِ الرَّحِيمِ

In the name of Allah the most Beneficent the most Merciful.

Dedication

I would like to dedicate this work to my mother, Mahjabeen, who made countless sacrifices so that I could pursue my dreams. This excerpt from the book entitled ‘As-Sahifa Al-Kamilah Al-Sajjadiyya’ by Imam Ali Zayn Al-Abidin is a reminder of your sacrifices:

“The right of your mother is that you know that she carried you where no one carries anyone, she gave to you of the fruit of her heart that which no one gives to anyone, and she protected you with all her organs. She did not care if she went hungry as long as you ate, if she was thirsty as long as you drank, if she was naked as long as you were clothed, if she was in the sun as long as you were in the shade. She gave up sleep for your sake, she protected you from heat and cold, all in order that you might belong to her. You will not be able to show her gratitude, unless through God's help and giving success.”

To my beloved husband Miqdad Raza, whose love & support throughout this journey has kept me going. I love you and this is for you.

Acknowledgements

I would like to begin by thanking God for all the blessings I have received, and the incredible opportunity to pursue my Ph.D. in Chemistry at UC Davis. I want to thank my advisor, Professor Jesús Velázquez, whose continuous support, commitment, guidance, and faith pushed me to achieve things I never thought I could. Thank you for always being there to talk and allowing me to grow as a scientist in your group. I am grateful for the support from Dr. Ivonne Ferrer, who guided me through the initial stages of my project and continued to be a mentor to me. I am also grateful to all past and present members of the Velázquez lab; Dr. Joseph Perryman, Dr. Andy Lam, Forrest Hyler, Julio Zamora, Courtney Craig, Kabian Ritter, Brian Wuille Bille, Rowan Brower, Jessica Ortiz-Rodríguez, Rose Smiley, Kingston Robinson, and Ankita Kumari. You all made our lab environment one of growth and support. I am so grateful I got to spend all this time with you all, and for everything you all have done for me.

I would also like to thank my dissertation committee members; Professor Bill Casey and Professor Susan Kauzlarich. Professor Casey has been a source of support and encouragement for me from the day I met him for my first ever advising appointment as a first year graduate student, to the moments in office hours for the CHE 240 (Advanced Analytical Chemistry) course, during my qualifying exam as well as my third year seminar, and even during the writing stages of my dissertation. Thank you for all your chemical insights and words of encouragement. Professor Kauzlarich, thank you for all your support in moving my research projects forward, assisting with Thermogravimetric Analysis (TGA) measurements, and in the help and advice during the writing stages of my dissertation.

During my Ph.D. journey I had the opportunity to collaborate with many amazing scientists and engineers at UC Davis. I want to acknowledge Dr. Maureen Kinyua from the Civil & Environmental Engineering department, and her students; Yihan Zhang, Gandhar Pandit, Jessica Hazard, Myar Abou Alfotouh, and Konane Gurfield. You all were instrumental in moving project goals forward. I also want to thank Professor Marie Heffern and her student Samuel Janisse for all their help with Liquid Chromatography-Mass

Spectrometry (LC-MS) measurements. I also want to thank collaborators outside UC Davis, including Professor Graham Peaslee at University of Notre Dame and his students Molly DeLuca and Arthur Alvarez for all their support with Particle-Induced Gamma Ray Emission (PIGE) spectroscopy measurements. I want to thank Will Kelly, Grey Kelly, and Chloe Kelly of the Napa Recycling and Composting Facility for helping with our commercial scale composting experiments. I want to acknowledge the California Department of Resources, Recycling, and Recovery (CalRecycle) for not only funding my projects, but also for the great advice and mentorship I received from the contract managers including Robert Contreras, Danielle Osborne, and Martine Boswell.

I would like to thank the Staff at UC Davis that work tirelessly to ensure smooth operations in the Department of Chemistry and beyond. Special thanks to Brad Wolf and Minh Hoang, you both were always there for graduate students no matter what our request was. Thank you for taking the time to answer my many questions, plan social events to uplift our spirits, and for supporting my graduate school career. I have worked closely with many general chemistry dispensary staff over the years and have enjoyed learning from them. Thanks to William Huang, Charito Pamplona, Darian Buckman, Lauren Pederson, and the General Chemistry safety teaching assistants (TA's); Ami Rose, Anita Vinjamuri, Ashley Fagundes, and Jayce Taylor. Thank you Professor Bryan Enderle for allowing me to develop my teaching skills and mentoring me through the process. I want to acknowledge staff members and TA's from the Nuclear Magnetic Resonance (NMR) facility, Dr. Andrew Thron from the Advanced Materials Characterization and Testing laboratory (AMCaT), Professor Ricardo Castro and his students from the NEAT consortium (Nano and New Materials in the Environment, Energy, Agriculture and the Environment), Paul Hrvatin from the chemistry instrumentation lab, and Scott Berg, the best facilities engineer. Thanks to Marleen and all the custodial staff that work hard to ensure we have a clean space to work in.

This work would not be possible without the love and support of my family. My mother Mahjabeen has sacrificed so much for me to pursue my dreams and I am so grateful to be her daughter. Thank you for allowing me to pursue my passion no matter what, for the weekly phone calls, and loving text messages.

Thanks to my Uncles Munawer, Aziz, and Imran, your words of encouragement always cheered me up. Thanks to my sister Zainab for her love and support. Thanks to my grandparents, Firoza & Mohamed Ali, for making so many sacrifices and leaving their home so that their children and grandchildren could aim to pursue dreams they never could have. Thanks to my second family the Razas (Mohsin, Mahejabin, Mohib, and Muhammad) for your love, prayers, and support. Finally, to the love of my life and my better half, my husband Miqdad Raza, you have seen me at my best and at my worst yet you never left my side. You supported me in this journey every day and I am happy to share my successes with you.

I want to thank all my friends who served as my support system on this journey. Diedra Shorty, Robert Duffie, Zheng Ju, and Saheli (Linda) Chatterjee. Thanks for all the game nights, for celebrating my birthday with me, and all the kind messages over the years. Special shoutout to my squad from the Bay Area; Sarah Hussain, Narjis Sheikh, Zahra Abbas, Naseem Rangwala, Zainab Mirza, and Amani Shoubber. You all have been an immense source of support and encouragement for me and I am grateful for it.

Copyright and Publication Information

This dissertation is based on the following publications:

1. Hussain, F.A., Zamora, J., Ferrer, I.M., Kinyua, M., Velázquez, J.M., Adsorption of crude oil from crude oil–water emulsion by mesoporous hafnium oxide ceramics, *Environ. Sci. Water Res. Technol*, 2020,**6**, 2035-2042.
2. Hussain, F.A., Pandit, G., Kinyua, M., Velázquez, J.M. Understanding Compostability of Food Service Packaging and Per- and Polyfluoroalkyl Substances, *California Department of Resources, Recycling, and Recovery (CalRecycle)*, 2021, submitted
3. Hussain, F.A., Janisse, S.E., Heffern, M.C., Kinyua, M., Velázquez, J.M. Adsorption of Perfluorooctanoic Acid from Water by pH-modulated Brønsted Acid and Base Sites in Mesoporous Hafnium Oxide Ceramics, *iScience*, 2022, submitted

Abstract

Water is an essential resource for all living organisms, yet it is contaminated with a wide variety of toxins that are harmful to human beings and the marine ecosystem. The two main contaminants discussed in this dissertation will be crude oil and per- and polyfluoroalkyl substances (PFAS). Crude oil enters the marine ecosystem when there is a crude oil spill on the surface of the ocean. The application of dispersant molecules causes the oil to be broken into smaller droplets which travel deeper into the ocean leading to further contamination. While crude oil affects large bodies of water, PFAS enter our drinking water streams by industrial waste, groundwater contamination, and leachate. PFAS are fluorinated carbon chains with a terminal functional group ranging from carboxylic acids, sulfuric acids, and alcohols. Unlike crude oil these molecules do not absorb visible light, and can't be seen in drinking water but are still very toxic. There is a need for developing robust, mechanically and chemically stable adsorbent materials to treat these contaminants in our water sources. This dissertation discusses the sol-gel synthesis of an understudied ceramic mesoporous hafnium oxide (MHO) for the adsorption of crude oil as well as PFAS. The MHO is chemically stable due to the variety of surface functional groups, thermally stable due to the fact that it is synthesized at high temperature (700°C), and has a bimodal pore network with both macropores (>50 nm), and mesopores (2-50 nm) that allow for rapid water flux and entrapment of contaminants respectively.

Chapter 1 aims to provide an introduction to challenges faced by our marine environments today by discussing effects of crude oil spills on the marine ecosystem, and impacts of per-and polyfluoroalkyl substances (PFAS) on our environment. The chapter reviews current technologies used to address crude oil spills and PFAS contamination. Finally it addresses some knowledge gaps in current adsorbent materials for water remediation, as well as describing favorable materials that can begin addressing these gaps. Foundational information on sol-gel synthesis of mesoporous hafnium oxide (MHO) ceramics is discussed in detail.

Chapter 2 describes the ability of monolithic mesoporous hafnium oxide ceramics as an adsorbent

to sequester crude oil from crude oil-water emulsions. The MHO ceramic monolith is incorporated in a vacuum filtration setup and evaluated in comparison to other commercially available crude oil adsorbents. This chapter shows that MHO can remove 99.9% crude oil from crude oil-water emulsions at acidic, neutral, and alkaline pH. The MHO ceramic monolith could be regenerated by calcination which furthers the sustainability of these materials.

Chapter 3 begins to describe PFAS remediation through biodegradation and composting of PFAS containing food service products. This work highlights results from both bench-scale and commercial-scale composting of FSP as a function of moisture content and inoculum. A moisture content of 60% was ideal for composting, whereas there was no difference in degradation with different inoculums. Unfortunately, PFAS containing FSP degraded at a fraction of the rate of non-PFAS containing FSP. Due to high moisture content during composting, PFAS from FSP dissolves in the water and can leach into groundwater sources. MHO monoliths were used to filter PFAS from water and we observed that longer chain hydrophobic PFAS had higher removal efficiencies than shorter chain PFAS.

Chapter 4 discusses the adsorption of the most common PFAS molecule found in water, perfluorooctanoic acid (PFOA) on to powders of MHO using pH-modulated Bronsted acid and base sites on the surface. The kinetics and adsorption behavior of PFOA on the surface of MHO as a function of charged species on the surface are discussed. The adsorption followed a two-step model, where the first step was rapid, and the second step was much slower. The ideal pH for adsorption of PFOA by MHO is an acidic pH of 2.3 as the surface is positively charged at this pH, and the PFOA molecule exists as an anion. Finally the regeneration of spent MHO powders via calcination is discussed.

Chapter 5 presents future work for PFOA treatment using electrochemical oxidation. Preliminary results using platinum mesh, nickel foil, and glassy carbon as working electrodes is presented. These electrodes showed PFOA destruction to carbon dioxide gas and unidentified fluorinated species. The degradation rates of PFOA drastically increased in more alkaline pH due to increased hydroxide radicals concentration, that are necessary for PFOA oxidation.

Table of Contents

Dedication.....	iii
Acknowledgements	iv
Copyright and Publication Information.....	vii
Abstract.....	viii
Table of Contents.....	x
List of Tables	xii
List of Figures.....	xiii
1 Chapter 1: Introduction.....	1
Background.....	1
Environmental Impacts of Crude Oil Spills	3
Remediation of Crude Oil Spills	4
Per- and Polyfluoroalkyl Substances Structure & Physicochemical Properties.....	6
Remediation of Per- and Polyfluoroalkyl Substances	9
Knowledge Gaps in Adsorbents for Water Remediation	13
Sol-gel Synthesis of Mesoporous Hafnium Oxide Ceramic Monoliths	14
References	16
2 Chapter 2: Adsorption of Crude Oil from Crude Oil–Water Emulsion by Mesoporous Hafnium Oxide Ceramics	25
Abstract.....	25
Introduction	25
Materials & Methods.....	28
Results and Discussion.....	31
Conclusions	49
Acknowledgements	49
References	50

3	Chapter 3: Understanding Fate of Per- and Polyfluoroalkyl Substances (PFAS) During Composting of Food Service Products.....	57
	Abstract.....	57
	Introduction	57
	Materials & Methods	59
	Results & Discussion.....	68
	Conclusions	83
	Acknowledgements	83
	References	84
4	Chapter 4: Adsorption of Perfluorooctanoic Acid from Water by pH-modulated Brønsted Acid and Base Sites in Mesoporous Hafnium Oxide Ceramics.....	90
	Abstract.....	90
	Introduction	90
	Materials & Methods	93
	Results & Discussion.....	96
	Conclusions	113
	Acknowledgements	113
	References	114
5	Chapter 5: Electrochemical Oxidation of Perfluorooctanoic Acid.....	122
	Abstract.....	122
	Introduction	122
	Materials & Methods	124
	Results & Discussion.....	127
	Conclusions	138
	Acknowledgements	138
	References	138

List of Tables

Table 1.1 Examples of Perfluoroalkyl Substances and Polyfluoroalkyl Substances	7
Table 2.1 Comparison of MHO Ceramic with Various Oil Sorbent Materials	41
Table 3.1 Details of Reactors in Bench-Scale Experimental Setup	62
Table 3.2 Summary of PFAS Detected Through FTIR, ¹⁹ F NMR, LC-MS.....	69
Table 3.3 Degradation of FSPs at T-3 and T-24 Days Using Food Waste Inoculum During Commercial-Scale Composting.....	73
Table 4.1 Kinetic Parameters of PFOA Adsorption on MHO.....	100
Table 4.2 Comparison of Our Work on PFOA Adsorption by MHO with Other State-of-the-Art Adsorbents.....	102
Table 4.3 Constants of Langmuir and Freundlich models of PFOA Adsorption on MHO.....	103
Table 5.1 Summary of PFOA Degraded during EO using 100 ppm of PFOA at pH 4.1 with Nickel, Platinum, and Glassy Carbon Anodes.....	129

List of Figures

Figure 1.1 Figure depicting the interconnected relationship between water and energy, described by the DOE as the water-energy nexus.	2
Figure 1.2 Graphic depicting various phenomenon occurring during a crude oil spill including evaporation and oxidation of volatile species, dissolution and dispersion of hydrophilic components, biodegradation using bacteria and fungi, and finally sedimentation to the marine floor.	4
Figure 1.3 Illustration of electrochemical oxidation pathway of PFAS in solution directly at the anode and indirectly at the cathode.	13
Figure 1.4 Illustrating active sites present on the surface of MHO; Lewis acid site (left), Brønsted acid site (center), and Brønsted base site (right).	14
Figure 1.5 Schematic illustrating each step of the sol-gel synthesis of monolith of mesoporous hafnium oxide ceramic.	16
Figure 2.1 Three main active sites on the surface of hafnium oxide: Lewis acid site (left), Brønsted acid site (middle), and Brønsted base site (right).....	27
Figure 2.2 a) Funnel with MHO ceramic attached using shrinking tube, b) Experimental set up for oil sequestration experiment.....	30
Figure 2.3 a) Free standing MHO ceramic with a diameter of 1 cm, b) SEM image of MHO ceramic illustrating network of macropores and mesopores, c) XRD pattern with major diffraction peaks indexed for MHO ceramic (top) overlaid with the published spectrum for MHO with heat treatment at 700 °C (bottom, ICSD Collection Code 27313).....	32
Figure 2.4 a) Low magnification and b) high magnification SEM image of melamine sponge purchased from He Andi used in filtration of crude oil-water emulsions.....	33
Figure 2.5 a) Low magnification and b) high magnification SEM image of grade 1 cellulose filter paper purchased from Sigma-Aldrich used in filtration of crude oil-water emulsions.	33
Figure 2.6 a) Low magnification and b) high magnification SEM image of wine filter purchased from Buon Vino used in filtration of crude oil-water emulsions.....	34
Figure 2.7 a) Image of crude oil-in-water emulsion in vials before and after filtration via MHO ceramic monolith in neutral pH, b) overlay GC-MS chromatograms of crude oil-in-water emulsion before sequestration and recovered liquid after sequestration using grade 1 cellulose filter paper, melamine sponge, commercial wine filter, and MHO ceramic monolith.....	35

Figure 2.8 a) Image of liquid in vials before and after filtration via MHO ceramic monolith in acidic pH, b) Overlaid GC-MS chromatograms of liquid-oil mixture before sequestration (green) and recovered liquid after sequestration using commercial wine filter (purple) and MHO ceramic monolith (black).....	36
Figure 2.9 a) Image of liquid in vials before and after filtration via MHO ceramic monolith in basic pH, b) Overlaid GC-MS chromatograms of liquid-oil mixture before sequestration (green) and recovered liquid after sequestration using commercial wine filter (purple) and MHO ceramic monolith (black).....	36
Figure 2.10 a) Top view of MHO ceramic before sequestration, b) top view of MHO ceramic after sequestration of crude oil-in-water emulsion in neutral pH, c) ¹ H NMR spectrum of crude oil-in-water emulsion before and after sequestration with MHO ceramic.	37
Figure 2.11 ¹ H NMR spectrum of blank solution consisting of deuterated methanol, deuterated chloroform with tetramethylsilane (99.5% + 0.05%), and nanopure water.....	38
Figure 2.12 a) Top view of MHO ceramic before sequestration, b) Top view of MHO ceramic after sequestration of crude oil-water emulsion in acidic pH, c) ¹ H NMR spectrum of liquid before and after sequestration with MHO ceramic.....	39
Figure 2.13 a) Top view of MHO ceramic before sequestration, b) Top view of MHO ceramic after sequestration of crude oil-water emulsion in basic pH, c) ¹ H NMR spectrum of liquid before and after sequestration with MHO ceramic.....	39
Figure 2.14 ¹ H NMR spectrum of liquid before and after sequestration with commercial wine filter in a) Neutral pH, b) Acidic pH, c) Basic pH.	40
Figure 2.15 a) TGA of MHO ceramic before sequestration (black) and after crude oil sequestration (red) in neutral pH under argon, b) Illustrating the change in color of MHO before filtration, after filtration of crude oil-water emulsions, and after heating to remove crude oil.....	42
Figure 2.16 a) TGA of wine filter before sequestration (black) and after crude oil sequestration (red) in neutral pH under argon, b) Illustrating the change in color of wine filter before filtration, after filtration of crude oil-water emulsions, and after heating to remove crude oil.....	43
Figure 2.17 a) Monodentate coordination of one oxygen atom to one hafnium ion, b) Bidentate chelating of two oxygen atoms to one hafnium ion, c) Bidentate bridging of two oxygen atoms to two hafnium ions, and d) ATR-FTIR spectrum of MHO ceramic before sequestration, after sequestration in neutral pH, and after calcination.....	45
Figure 2.18 ATR-FTIR spectrum of crude oil with major peaks labelled.....	46
Figure 2.19 ATR-FTIR spectrum of MHO ceramic before sequestration, after sequestration in acidic pH, and after calcination.	47

Figure 2.20 ATR-FTIR spectrum of MHO ceramic before sequestration, after sequestration in basic pH, and after calcination.	48
Figure 3.1 Illustration of A) schematic of the reactor, and B) reactor with synthetic food waste and cow manure.	61
Figure 3.2 Aerated composting pile at Napa Recycling Facility with biofilter layer, mesh bags with FSP samples, and feedstock + inoculum.....	63
Figure 3.3 a) Funnel with MHO ceramic attached using shrinking tube, b) vacuum filtration setup for PFAS removal.	67
Figure 3.4 Average percent degradation of five different FSP tested during bench-scale composting using cow manure at 45% moisture content (blue) and 60% moisture content (orange).	70
Figure 3.5 Change in fluorine concentration on the fiber plate over 24 days of bench-scale composting using cow manure at 45% moisture content (blue) and 60% moisture content (orange).	71
Figure 3.6 Average percent degradation of six different FSP tested during commercial-scale composting at 60% moisture content using food waste (red) and old compost (gold).	74
Figure 3.7 Change in fluorine concentration on a) the fiber plate , b) PLA lined bagasse clamshell over 24 days of commercial-scale composting at 60% moisture content using food waste (red) and old compost (gold).....	75
Figure 3.8 a) ESEM image of MHO monolith illustrating both macropores and mesopores, b) XRD pattern of experimentally synthesized MHO (black) overlaid with literature value of MHO (ICSD 57385), c) FTIR spectrum illustrating functional groups on surface of MHO.	77
Figure 3.9 a) ESEM image of Ni-MOF-74 illustrating aggregates of elongated crystals, b) XRD pattern of Ni-MOF-74 synthesized and overlaid with published pattern (CCDC 1494751), c) ESEM image of Mg-MOF-74 depicting aggregates of elongated crystals, d) XRD pattern of Mg-MOF-74 synthesized and overlaid with published pattern (CCDC 1863524).....	78
Figure 3.10 ¹⁹ F NMR spectra showing terminal CF ₃ peak of PFAS molecule before and after filtration using MHO monolith with a) PFBA, b) PFHxA, c) PFOA.....	80
Figure 3.11 FTIR spectra of a) MHO before filtration, MHO after filtration with PFBA, and PFBA standard, b) MHO before filtration, MHO after filtration with PFHxA, and PFHxA standard, c) MHO before filtration, MHO after filtration with PFOA, and PFOA standard, d) Inset of MHO before filtration, MHO after filtration with PFOA, and PFOA standard from 800-1800 cm ⁻¹	82
Figure 4.1 Three main active sites on the surface of hafnium oxide: Lewis acid site (left), Brønsted acid site (middle), and Brønsted base site (right).....	92

Figure 4.2 a) ESEM image depicting particles of MHO with mesopores. b) XRD pattern with diffraction peaks for monoclinic MHO ceramic synthesized (top) overlaid with the published spectrum for monoclinic MHO ceramic (bottom, ICSD Collection Code 57385), c) pH_{PZC} determination of MHO using pH drift method, d) Nitrogen gas adsorption isotherm used to determine BET surface area..... 97

Figure 4.3 a) Rate of PFOA adsorption on MHO at pH 2.3 using 1.25 g MHO ceramic, 50 mL of 1000 ppm PFOA, over a period of 12 hours. Two-step adsorption process delineated using a red dotted line. b) Adsorption behavior of PFOA on MHO ceramic illustrating the rapid transfer of PFOA from solution to surface of MHO as well as slower diffusion of PFOA into the mesopores of MHO. c) Decrease in area of the terminal CF_3 peak in ^{19}F NMR of PFOA during adsorption on MHO. d) Pseudo-second-order model fit of the adsorption of PFOA on MHO. 98

Figure 4.4 a) Structure of PFOA with different types of Fluorine numbered, b) ^{19}F NMR spectrum of PFOA with TFA (internal standard) with F_1 labelled, c) ^{19}F NMR spectrum with F_2 - F_7 labelled..... 99

Figure 4.5 Pseudo-first-order model of adsorption of 1000 ppm PFOA on 1.25 g of MHO..... 100

Figure 4.6 Adsorption of PFOA on MHO ceramic fitted using the Langmuir isotherm, and the Freundlich isotherm at 25°C. 103

Figure 4.7 a) Rate of adsorption of PFOA on MHO at pH 2.3, 4.3, and 6, b) Decrease in area of CF_3 peak in ^{19}F NMR of PFOA during adsorption on MHO at pH 2.3, pH 4.3, and pH 6.3. 104

Figure 4.8 a) Illustration of PFOA adsorption on MHO at pH 2.3, 4.3, and 6.3, b) Description of MHO surface charge and PFOA charge as a function of pH. At $pH < 4.7$ MHO is positively charged with conjugate acid active sites, at $pH = 4.7$ MHO has a neutrally charged surface, and at $pH > 4.7$ MHO is negatively charged with conjugate base active sites. pK_a of PFOA is 0.5-3.8. At $pH < pK_a$ the molecule does not dissociate in solution, at $pH = pK_a$ the molecule is in equilibrium with the deprotonated anion, and $pH > pK_a$ the PFOA exists mostly as the deprotonated anion in solution. 106

Figure 4.9 FTIR of MHO ceramic after PFOA adsorption at pH 2.3, pH 4.3, and pH 6.3 in the range of a) 1450-1800 cm^{-1} , b) 950-1450 cm^{-1} 108

Figure 4.10 TGA of MHO ceramic before adsorption (black) and after PFOA adsorption at pH 2.3 (red) under argon. 109

Figure 4.11 FTIR spectra of MHO before adsorption, PFOA standard, MHO after adsorption of PFOA, and MHO after calcination at 500°C from a) 650-4000 cm^{-1} , b) 950-1800 cm^{-1} 111

Figure 4.12 a) XRD of MHO before adsorption (black), after calcination (purple), and from Inorganic Crystal Structure Database, b) SEM image of MHO after calcination showing similar mesoporous morphology as MHO before adsorption..... 112

Figure 5.1 Illustration of schematic of three electrode cell setup with the counter electrode (graphite) on the left side separated by a cation anion exchange membrane, the right side is the working compartment side with the stir bar, reference electrode of Ag/AgCl, argon gas purge needle, and needle that is connected directly to the GC.....	126
Figure 5.2 Depiction of direct oxidation of PFOA at the anode, and indirect oxidation of PFOA via OH• in bulk solution.....	128
Figure 5.3 Results from electrochemical oxidation of 100 ppm PFOA in 0.1M Na ₂ SO ₄ at a potential of 1.92V vs. Ag/AgCl using platinum for 21 hours by ¹⁹ F NMR using liquid aliquot from a) working electrode compartment, b) counter electrode compartment, and c) gas chromatography of the headspace on the working electrode compartment.....	131
Figure 5.4 Results from electrochemical oxidation of 100 ppm PFOA in 0.1M Na ₂ SO ₄ at a potential of 1.60V vs. Ag/AgCl using nickel for 21 hours by ¹⁹ F NMR using liquid aliquot from a) working electrode compartment, b) counter electrode compartment, and c) gas chromatography of the headspace on the working electrode compartment.....	132
Figure 5.5 Results from electrochemical oxidation of 100 ppm PFOA in 0.1M Na ₂ SO ₄ at a potential of 2.30V vs. Ag/AgCl using glassy carbon for 21 hours by ¹⁹ F NMR using liquid aliquot from a) working electrode compartment, b) counter electrode compartment, and c) gas chromatography of the headspace on the working electrode compartment.....	133
Figure 5.6 Results from electrochemical oxidation of 100 ppm PFOA in 0.1M Na ₂ SO ₄ at a potential of 1.92V vs. Ag/AgCl at pH 5.1 using platinum for 21 hours by ¹⁹ F NMR using liquid aliquot from a) working electrode compartment, b) counter electrode compartment, and c) gas chromatography of the headspace on the working electrode compartment.....	135
Figure 5.7 Results from electrochemical oxidation of 100 ppm PFOA in 0.1M Na ₂ SO ₄ at a potential of 1.60V vs. Ag/AgCl at pH 5.1 using nickel for 21 hours by ¹⁹ F NMR using liquid aliquot from a) working electrode compartment, b) counter electrode compartment, and c) gas chromatography of the headspace on the working electrode compartment.....	136
Figure 5.8 Description of PFOA molecule in solution as a function of pH. pK _a of PFOA is 0.5-3.8. At pH<pK _a the molecule does not dissociate in solution, at pH=pK _a the molecule is in equilibrium with the deprotonated anion, and pH>pK _a the PFOA exists mostly as the deprotonated anion in solution.	137

1 Chapter 1: Introduction

Background

Water is an essential resource for all living organisms, from marine wildlife in the ocean to human beings living on land. Despite 70% of the earth's surface being covered in water only 2.5% of it is potable.¹ In 2012, the United State's Department of Energy (DOE) developed the Water-Energy Nexus to direct next steps to address issues with water and energy availability.² The DOE's Water-Energy Nexus: challenges and opportunities report found that water and energy are interdependent as water is used in energy generation, and energy is used in water treatment and transport as illustrated in **Figure 1.1**. Changes in temperature, precipitation, and oil and gas exploration threaten existing energy and water infrastructure. For example, generating natural gas and oil through hydraulic fracturing and horizontal drilling impacts regional water quality and availability.³ Therefore, exploring new and efficient adsorbent materials for water remediation applications will make our waters cleaner, and in turn save energy. The work presented herein will focus on evaluating adsorbent materials for the advancement of water treatment technologies for two types of contaminants specifically, crude oil from large spills in the ocean and per- and polyfluoroalkyl substances (PFAS) found in leachate from composting facilities.

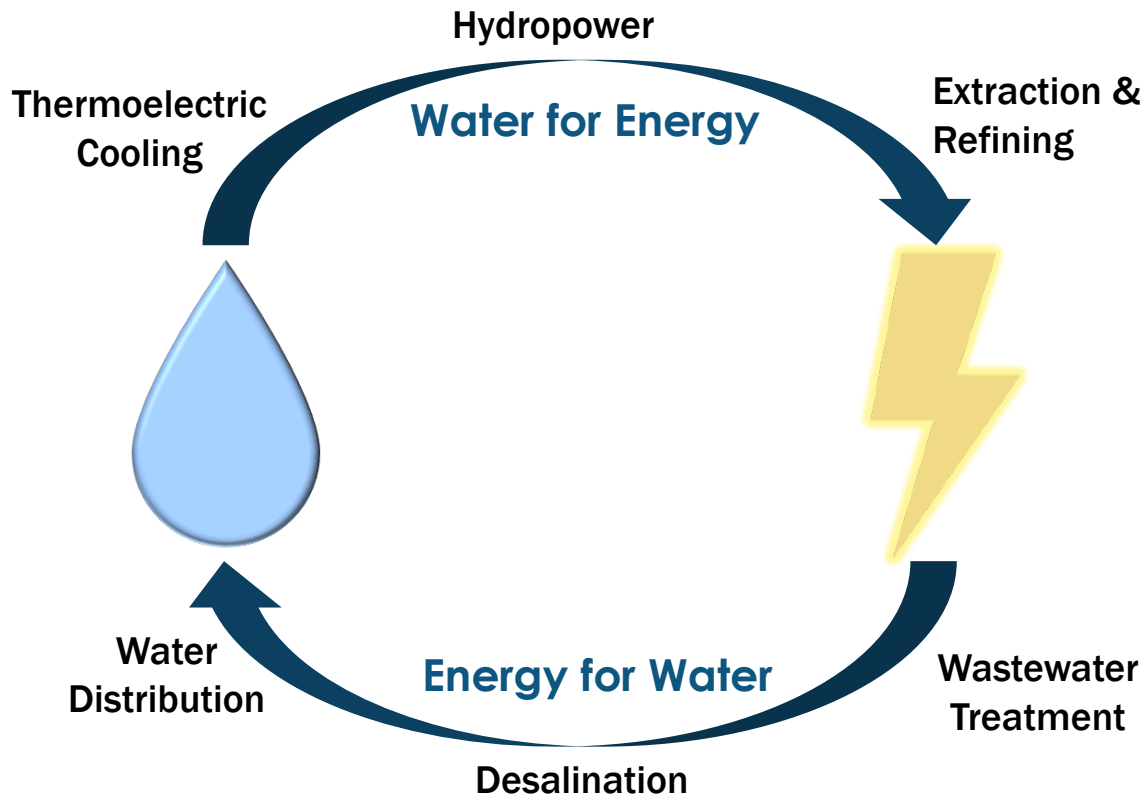


Figure 1.1 Figure depicting the interconnected relationship between water and energy, described by the DOE as the water-energy nexus.

Environmental Impacts of Crude Oil Spills

Crude oil spills are defined as the accidental or deliberate release of oil into the marine environment during transport, exploration, or storage.⁴ Crude oil consists mostly of hydrocarbons (98%) as well as other elements such as nitrogen (0.5%), sulfur (0.5%), oxygen (0.5%), and metals (0.5%) such as nickel, copper, and iron.⁵ Crude oil spills have detrimental impacts on wildlife such as birds whose wings become too heavy to fly away in a crude oil spill, and fish that are poisoned by the crude oil spilled in the ocean.⁶ This in turn affects other marine activities like fishing, tourism, and agriculture.⁷ It also affects people in the area who depend on fishing for their livelihood and sustenance.⁸ It can lead to acute health issues like headaches, nausea, rashes, and fatigue. There have also been more chronic health issues observed such as respiratory disorders, endocrine abnormalities, and psychological disorders.⁹ The cost to clean up crude oil spills is also a huge economic burden. After the Exxon Valdez spill in Alaska, the EPA established the Oil Pollution Act (OPA) of 1990 to respond to oil spills, and required oil storage facilities to have emergency oil spill response plans.¹⁰ According to the OPA judicial sanctions, the penalty per day of a crude oil spill is \$25000, and \$1000 per barrel.¹¹ Therefore, developing rapid methods to clean up oil spills is of the utmost importance.

To understand how to clean up oil spills, it is important to first understand what happens on the marine surface when there is a crude oil spill, these occurrences are shown in **Figure 1.2**. When crude oil spills on the surface some more volatile components of the crude oil may evaporate, some may get oxidized when exposed to air. Moreover, biodegradation of aliphatic hydrocarbon chains as well as aromatic components of crude oil can occur using microbial communities in the ocean such as *Gordonia* and *Bacillus* bacteria, and fungi like *Candida* and *Fusarium*. Finally, some hydrophilic components of crude oil can begin to dissolve or disperse and form smaller droplets that travel deeper into the ocean. Eventually crude oil droplets sediment into the ocean permanently causing irreparable harm to the marine floor.¹²

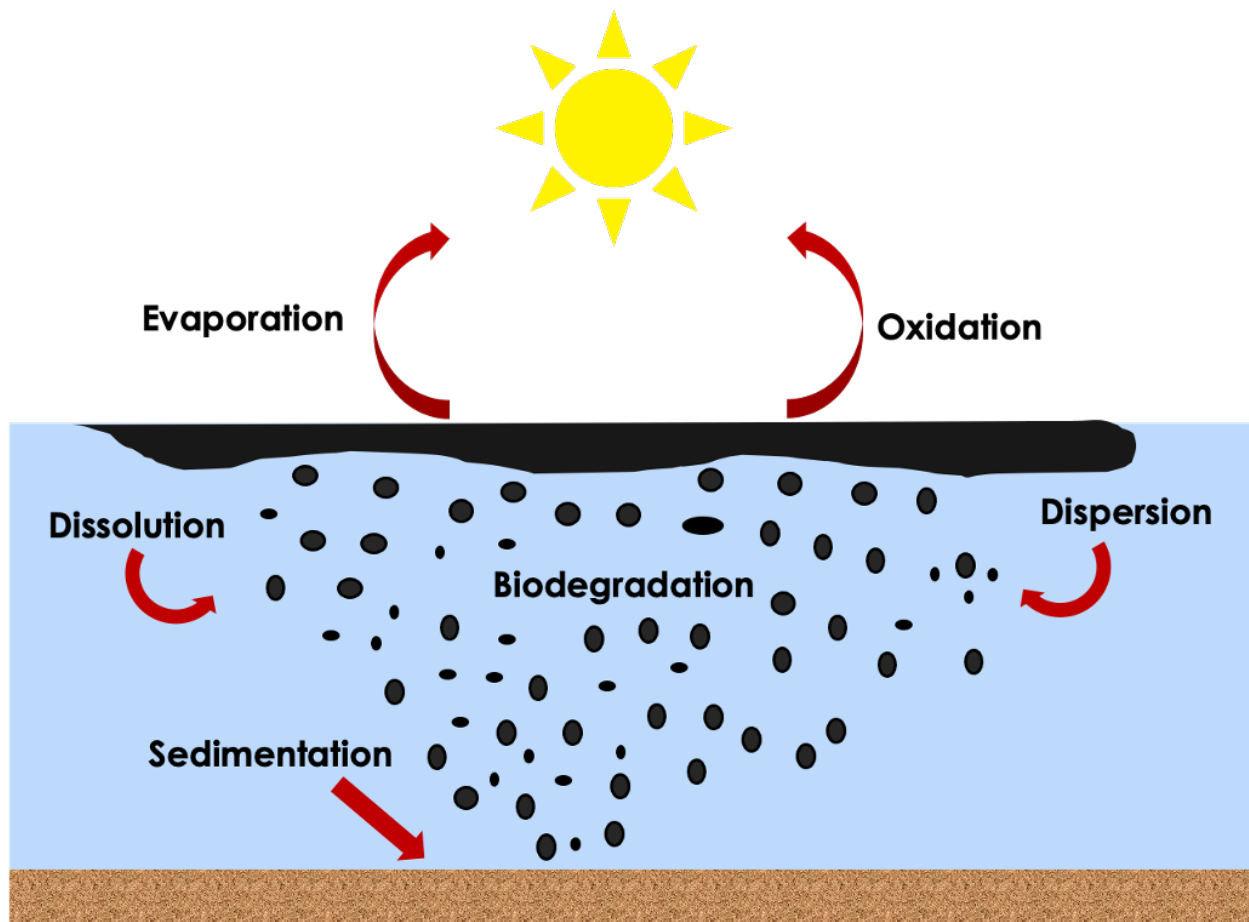


Figure 1.2 Graphic depicting various phenomenon occurring during a crude oil spill including evaporation and oxidation of volatile species, dissolution and dispersion of hydrophilic components, biodegradation using bacteria and fungi, and finally sedimentation to the marine floor.

Remediation of Crude Oil Spills

Environmental remediation is the removal of contaminants from water to protect human health and vulnerable ecosystems. For the initial stages of remediation of crude oil spills in the ocean mechanical methods are used to contain the spill and prevent spreading to the shores. Booms are floating devices that are deployed to contain the oil that can later be adsorbed with the help of skimmers.¹³ Skimmers are also buoyant devices that can separate crude oil from water. Three different kinds of skimmers will be discussed, suction, weir, and oleophilic skimmers. Suction skimmers as the name suggests use vacuum to sequester crude oil from the surface, whereas weir skimmers use gravitational force. Oleophilic (oil-attracting) skimmers are a relatively new skimmer that have components such as belts, disks, and chains that are

oleophilic. Skimmers have limitations since they are prone to clogging and are costly due to the labor associated with their deployment. It is also harmful for the people deploying them as they are more prone to exposure to crude oil and its negative health effects.¹⁴

Chemical surfactant molecules are an alternative to mechanical methods as they prevent the spread of the crude oil spill and minimize spill impacts.¹⁵ Surfactant molecules such as Corexit EC9500A and Corexit EC9527A are used due to their hydrophobic tail and hydrophilic head. Corexit surfactants are commercially available and made up of 50% hydrocarbons, 40% glycols, and 10% dioctylsulfosuccinate. The molecules break apart the layer of crude oil to surfactant stabilized droplets of crude oil in water. This would increase the ability of the oil droplet undergo biodegradation by fungi or bacteria in the ocean.¹⁶ However, not all the oil is degraded in the ocean, some droplets travel deeper and sediment into the bed of the ocean permanently. In addition, these surfactant molecules are toxic and have detrimental effects on microzooplankton among various and vulnerable marine microbial communities.¹⁷

Using adsorbents for crude oil in water emulsions is facile, economically feasible, and non-toxic to the environment or people.¹⁸ There are a wide variety of adsorbents available for crude oil spill clean-up ranging from agricultural waste, to synthetic polymers, and inorganic nanomaterials. Some examples of agricultural waste used to clean up crude oil spills include corn stalks,¹⁹ rice husks,²⁰ and sugarcane bagasse²¹. Every year 5.5 billion tons of agricultural waste is produced globally, making these materials extremely abundant.²² These materials are affordable, environmentally friendly, and biodegradable. However, they are not very mechanically robust and can't be reused after adsorption. Agricultural waste is also very hydrophilic which means that it can adsorb water as well as crude oil.²³ On the contrary, synthetic polymers such as polyurethane²⁴ and polypropylene²⁵ are hydrophobic and oleophilic which ameliorates the crude oil adsorption. This also makes the adsorbents buoyant and allows for crude oil adsorption from the surface. However, these polymers are not biodegradable and must be disposed of in a landfill or incinerated, both of which lead to toxic gas emissions. To this end, inorganic nanomaterials have been synthesized and used for crude oil spill remediation. Carbon nanotubes are appropriate for crude oil spills due to their

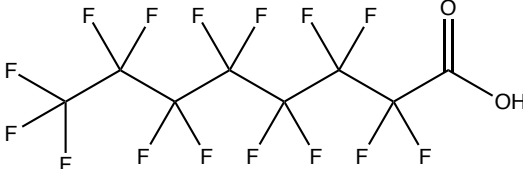
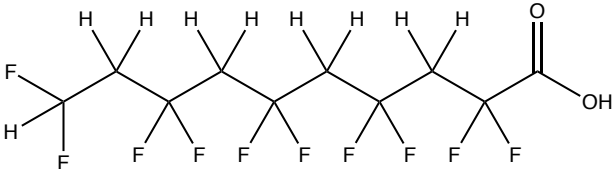
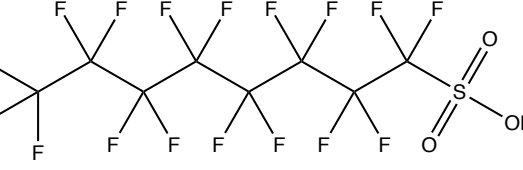
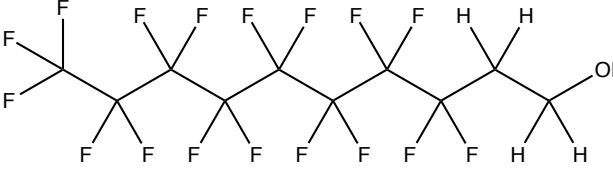
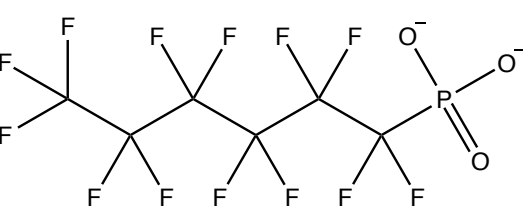
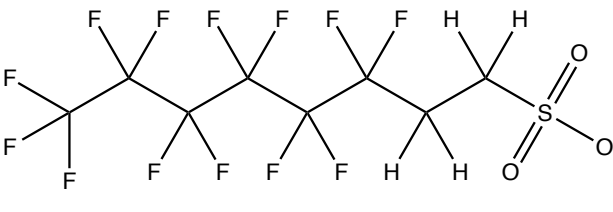
hydrophobic nature and their ability to be modified with nanoparticles and magnetic composites.²⁶ Nanoparticles of iron oxide are also commonly used specifically the paramagnetic magnetite (Fe_3O_4) and maghemite. These magnetic nanoparticles are oleophilic and can be dispersed in an oil spill and recovered easily using a magnetic field.²⁷ Mesoporous metal oxides, such as silica, are also attractive for crude oil spills due to their large surface area and porosity, but silica is not extremely stable and can swell when exposed to organic solvents making it a challenge to regenerate and reuse spent adsorbents.²⁸ Silica is also hydrophilic which limits the oil adsorption, however recently studies have shown that silica coated with oleic acid increases the oleophilicity of the molecule and can lead to increase oil adsorption.²⁹

Per- and Polyfluoroalkyl Substances Structure & Physicochemical Properties

Every five years the EPA publishes a contaminant candidate list (CCL) that includes recent water contaminants ranging from pharmaceuticals, metals, and even per-and polyfluoroalkyl substances (PFAS).³⁰ PFAS are a large group of over 4000 synthetic industrial chemicals which have been found in the environment from ground water, to soil, and even the ocean.³¹ The hydrogens in the hydrocarbon backbone are replaced by fluorine atoms, and can be described as $\text{C}_n\text{F}_{2n+1}$ for perfluorinated substances.³² PFAS can be further organized by the different functional groups which give rise to different characteristics and physical properties. The polyfluorinated substances are often the precursors for PFAAs (perfluoroalkyl acids). PFAAs include compounds like perfluoroalkyl sulfonic acids (PFSAs), perfluorocarboxylic acids (PFCAs), polyfluoroalkyl phosphoric acid diesters (diPAPs), perfluorophosphinates (PFPiAs), and perfluorophosphonates (PFPAs). PFAAs can usually contain between 2 to 18 carbons. Polyfluoroalkyl substances comprise of a far more diverse group than the perfluoroalkyl substances because it contains the carbon-hydrogen and carbon-fluorine bonds in the carbon chain. There are also various functional groups that can be anionic, cationic, neutral, or zwitterionic. Polyfluorinated compounds include fluorotelomer alcohols (FTOHs), fluorotelomer sulfonic acids, polyfluorinated alkyl phosphates, and many others.

Polyfluorinated compounds have many fluorines and perfluorinated compounds are fully fluorinated as shown in **Table 1.1** below.³³

Table 1.1 Examples of Perfluoroalkyl Substances and Polyfluoroalkyl Substances

Perfluoroalkyl Substances	Polyfluoroalkyl substances
	
Perfluorooctanoic acid (PFOA)	Polyfluorinated carboxylic acid
	
Perfluorooctanesulfonic acid (PFOS)	8:2 Fluorotelomer alcohol (FTOH)
	
C6 Perfluorophosphonate	6:2 Fluorotelomer sulfonic acid

All PFAS have very stable carbon-fluorine bonds with a bond energy of 485 kJ/mol which is relatively high in comparison to carbon-carbon bonds with a bond energy of 346 kJ/mol, carbon-nitrogen bonds of 305 kJ/mol, and even carbon-oxygen bonds of 358 kJ/mol.³⁴ The PFAAs are amphiphilic (both hydrophobic and hydrophilic) as they contain a perfluoroalkyl group which is hydrophobic and an anionic carboxylate or sulfonate group which is hydrophilic. Such amphiphilic properties make PFAAs useful for coatings and surfactants. The perfluorinated carbon chain is also lipophobic which makes it resist oil, grease, and other non-polar components.³⁵

Properties of PFAS depend on chain-length and functional groups. Short-chain PFAS have a carbon chain length which is 7 carbons or less for carboxylic acids and 5 carbons or less for sulfonic acids. Therefore, the long-chain PFAS have a carbon chain which is 8 carbons or more for carboxylic acids and 6 carbons or more for sulfonic acids.³⁶ When compared to long-chain PFAS, the short-chain PFAS affect human health as they tend to have shorter half-lives in blood, however they are more mobile, and hence not easily removed from water. For example, perfluorohexanoic acid (PFHxA) a short chain PFAS has a human half-life of 32 days,³⁷ whereas perfluorooctanoic acid (PFOA) has a half-life of 3.8 years.³⁸

Per- and Polyfluoroalkyl Substances Regulations

In 2006 EPA implemented the PFAS stewardship program. The program had two goals; one was for the companies involved to reduce all PFOA materials including chemical precursors that can breakdown to form PFOA by 2010. The second goal was to have eliminated these chemicals from emissions and products by 2015. The eight major companies that participated were Arkema, Asahi, BASF Corporation, Clariant, Daikin, 3M, DuPont, and Solvay Solexis. Most companies met these goals by completely stopping the manufacturing and importing of long-chain PFAS and transitioned to other chemicals.³⁹ Other efforts to monitor PFAS in the industry is by Chemical Data Reporting, which requires manufacturers and importers of PFOS to report if they meet certain production volume thresholds (usually 25,000 pounds) at a single site. The last time the manufacturing of PFOS was reported to EPA as part of this collection effort was 2002.⁴⁰ Even though manufacture and import of PFOA and PFOS has phased out in the United States as part of these programs, there may still be existing stock that is used. In addition to these programs, the EPA has issued regulations known as Significant New Use Rules (SNURs) that requires manufacturers to notify the EPA of new uses of such chemicals before they are on the market. The regulation also specifies that the company needs to notify the EPA at least 90 days before beginning any such activity, which would allow the EPA time to review the plan and make any necessary changes to the products and chemicals used.⁴¹ The most recent health advisory from the US EPA states that the levels for PFOA and PFOS alone in drinking water should not exceed 70 ng/L or 70 ppt (parts per trillion). This is also the limit for combined PFOA and

PFOS in drinking water.⁴² However, the California EPA submitted a draft report in July 2021 proposing even lower concentrations of PFOA in drinking water to 0.007 ppt and 1 ppt for PFOS.⁴³

Remediation of Per- and Polyfluoroalkyl Substances

PFAS can leach into soil and groundwater from compostable products that contain PFAS. They can also end up in groundwater, leachates, and drinking water from industrial facilities using PFAS. Three different techniques to remove PFAS from the environment will be discussed; Composting, Adsorption, and Electrochemical oxidation. Composting and electrochemical oxidation are destructive removal techniques, whereas adsorption is a non-destructive removal method.

Composting

There is a growing interest and effort from the waste management industry to divert food waste from landfills and recycle organic waste through composting. Composting is a biochemical process that converts organic waste in the presence of oxygen into carbon dioxide, heat, water, and a stable organic substance that can be recovered as a soil amendment or organic fertilizer.⁴⁴ Composting involves microbial organisms, such as worms and millipedes, breaking down the bulk of organic matter by mechanical means while microorganisms, such as bacteria and fungi, chemically convert the remaining organic matter to end products of carbon dioxide, heat, water, and compost.⁴⁵ While carbon dioxide is a product of this aerobic process, studies have shown that greenhouse gas (GHG) emissions from food waste decomposition in landfills are significantly higher than GHG emissions from composting due to methane's greater global warming potential,⁴⁶ thus further demonstrating the importance of proper disposal of food waste in aerobic composting facilities. The resulting compost can be used as a soil amendment that enhances soil properties by increasing soil buffering capacity and moisture holding capacity, providing essential nutrients for plants, stimulating biological activity, and improving soil structure.⁴⁷ Composting is a reliable waste treatment option for organic waste with a valuable product; however, composting can only be successful if the process

is effectively managed.⁴⁸ Since food waste can be highly variable depending on its source, it is important to study multiple parameters of the composting process to ensure an optimized system with a stable product.

Food Service Packaging Product (FSP) is a broad term for compostable bioplastics and fibers. This includes cups, bowls, lids, plates, containers, cutlery, overwrap, laminated film and fast-food wraps and delicatessen containers. FSP has physical and mechanical properties that expand the shelf life of food. Physical properties protect the food from tensile forces and tears and provide a barrier to oxygen, carbon dioxide, anhydride, and odorous compounds. Mechanical properties allow these products to act as heat sealants and prevent microbial contamination.⁴⁹ Composting these products is difficult as they are often coated with PFAS which are environmentally persistent and create an additional layer for microbial degradation making it more energy-intensive and time-consuming to breakdown.

A wide variety of microbes have been explored for the biodegradation of PFAS using the microbial infallibility hypothesis which states that if there is energy to be gained from a compound, a microorganism will figure out how to extract it and create a niche for itself.⁵⁰ While degradation of PFAS is a challenge, the microbes function by identifying a weak spot in the molecule that could be more susceptible to degradation. For example, a double bond which is more electron rich, and henceforth more reactive than a C-F bond.⁵¹ One example of a bacteria that has been studied is *Dehalococcoides*. The degradation of PFAS with *Dehalococcoides* is accompanied by lactate which acts as an electron donor whereas the PFAS act as electron acceptors. The *Dehalococcoides* are able to degrade 100% of an unsaturated PFAS (E)-perfluoro(4-methylpent-2-enoic acid) after 130 days.⁵² The more common PFAS such as PFOA and PFOS have no vulnerable area for microbial degradation, however A6, a strain of the microbe *Acidimicrobium*, which is found in the wetlands of New Jersey has been investigated for the degradation of PFOA and PFOS. Researchers found that after 100 days the *Acidimicrobium* was able to degrade PFOA and PFOS by 60%.⁵³ The limitations of current microbes being studied for PFAS degradation is the incubation time needed for the degradation of PFAS, as mentioned above the *Dehalococcoides* required 130 days for degradation and the *Acidimicrobium* required 100 days. Along with long degradation times these microbes are also not

selective so in the presence of a wide variety of nutrients and halogenated compounds in compost the degradation efficiency of microbial communities towards PFAS may be reduced.⁵⁴

Adsorption

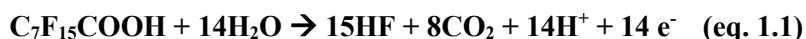
Adsorption is a non-destructive method to remove contaminants from water. The processes that drive the adsorption of PFAS in solution on to the adsorbent are related to hydrophobicity and electrostatic interactions. The hydrophobic interaction between the PFAS and the adsorbent increases as chain length of PFAS increases, this phenomenon will be discussed in more detail in Chapter 3. Studies with kaolinite ($\text{Al}_2\text{Si}_2\text{O}_5(\text{OH})_4$) as an adsorbent have shown that when there is a mixture of PFAS, the longer chain length PFAS which are more hydrophobic have higher removal efficiency than shorter PFAS.⁵⁵ Electrostatic interaction between the adsorbent and contaminant are driven by the charge on the adsorbent and the contaminant molecule. In the case of PFAS, the electrostatic interactions occur due to the head group on the PFAS molecule (e.g. carboxylate, sulfate, phosphate, etc). Depending on the pH of the solution, PFAS molecules will exist as anions in solution and can have electrostatic attractions with positively charged adsorbent surfaces. Many studies have shown that PFAS adsorption is preferred at low pH, if pH is higher than the point of zero charge of the adsorbent the surface will be negatively charged and there will be electrostatic repulsions which decreases adsorption.⁵⁶ Therefore, the pH of adsorption is very critical for PFAS remediation as will be discussed in more detail in Chapter 4 of this work.

The most commonly studied adsorbent for PFAS adsorption is activated carbon. Activated carbon (AC) is affordable, can be regenerated after adsorption, and extremely abundant as it can be produced from various natural sources such as coconut shells, wood, and coal. The adsorption of PFAS onto AC is driven by physical mass transfer from the liquid to the solid typically by Van der Waals interactions. Van der Waals interactions occur when electron clouds from PFAS are in contact with electron clouds from the surface of the adsorbent. Therefore, the removal efficiency is higher for the longer chain PFAS as they are more hydrophobic and have increased Van der Waals interactions with AC.⁵⁷ In contrast, anion exchange (AIX)

resins such as Purolite A600 and Purofine PFA694, remove PFAS by physical mass transfer as well as electrostatic interactions. The positively charged AIX resins attracts the negatively charged PFAS anion in solution. Due to this dual interaction AIX resins can remove PFAS at a higher rate than the AC, however, AIX resins are only made for single use and methods to regenerate them are still being developed.⁵⁸ Metal oxide adsorbents have also been evaluated for PFAS adsorption.^{59,60} Boehmite (AlOOH) has shown increased PFAS removal efficiency at acidic pH (pH 4) due to the fact that the surface of the adsorbent is positively charged since the point of zero charge for boehmite is at pH 8.4.⁶¹ This increases electrostatic attraction between PFAS anions in solution and the positively charged adsorbent surface. These changes in surface charge have motivated the applications of metal oxides for PFAS removal.

Electrochemical Oxidation

Electrochemical oxidation is a treatment technology that uses electrical current to oxidize persistent pollutants including PFAS making it a destructive treatment method. Through this process PFAS are converted into carbon dioxide, fluoride ions, shorter chain PFAS, and in some cases hydrofluoric acid.⁶² Electrochemical oxidation can occur directly at the anode by electron transfer from the PFOA molecule to the anode, whereas during indirect electrochemical oxidation the PFAS molecule are degraded in solution by the power of electrochemically created radicals such as the hydroxide radical originating from the cathode.⁶³ Both these reaction pathways are shown in **Figure 1.3**. The overall degradation reaction for PFOA⁶⁴ can be written as shown in **eq 1.1**:



The degradation of PFOA is a sequence of reactions each of which involves only one electron, to completely mineralize PFOA a total of 14 electrons is needed.⁶⁵ The most common type of anode material studied for PFOA electrochemical oxidation is boron-doped diamond (BDD) anodes. BDD has shown 99.5% degradation efficiency for PFOA over a duration of 4 hours.⁶⁶ Despite BDD being non-corrosive and

commercially available, the cost of the BDD anode is approximately \$7125/m².⁶⁷ Ceramic materials like Magnéli phase titanium suboxides (Ti₄O₇) are conductive and have comparatively lower production costs, however, the time needed to completely degrade PFOA was 17 hours.⁶⁸ PFOA degradation was also observed via electrochemical activation of peroxymonosulfate (indirect oxidation) at the Ti/SnO₂-Pb anode, the degradation time in this instance was much shorter as it only required 2 hours.⁶⁹

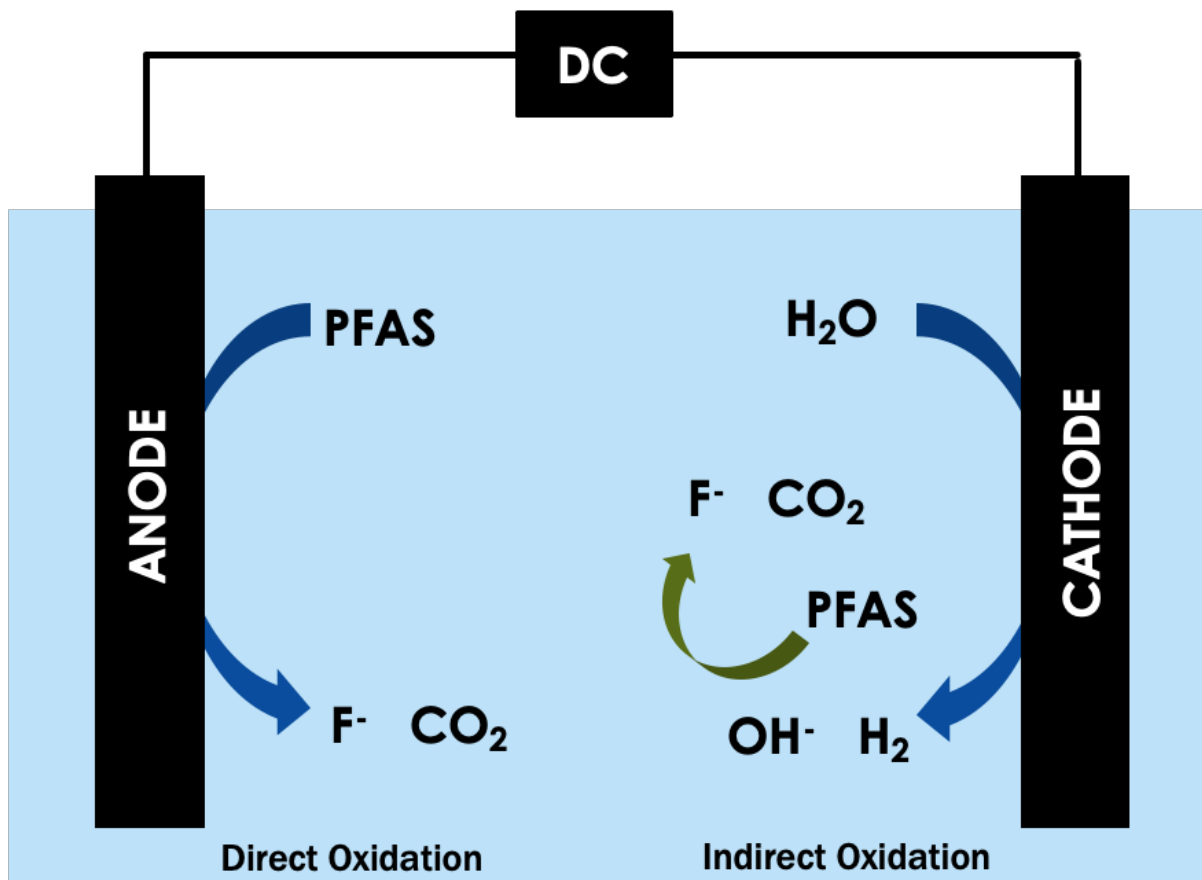


Figure 1.3 Illustration of electrochemical oxidation pathway of PFAS in solution directly at the anode and indirectly at the cathode.

Knowledge Gaps in Adsorbents for Water Remediation

Based on aforementioned remediation technologies, there is a need for robust mechanically and chemically stable adsorbents for the adsorption of contaminants from water. Be it the removal of emulsified crude oil from the ocean, or the removal of more recent contaminants of interest like PFAS from drinking water. This work attempts to address these knowledge gaps using an underexplored material for water remediation,

mesoporous hafnium oxide (MHO) ceramics. The surface of mesoporous hafnium oxide has a few active sites that allow it to perform in extreme pH conditions illustrated in **Figure 1.4**. These active sites are; Lewis acid sites originating from unoccupied hafnium d orbitals, Brønsted acid sites which donate a proton in basic media resulting in a negatively charged conjugate base active site, and Brønsted base sites which accept a proton in acidic media resulting in a positively charged conjugate acid active site.⁷⁰ MHO does not shrink or swell in organic or ionic solvents, unlike polymeric based materials, which is necessary for adsorption of hydrophobic crude oil, and PFAS molecules that tend to ionize in solution. The MHO monolith is bimodal which means it has both macropores (>50 nm) and mesopores (2-50 nm). This bimodal pore structure makes the material ideal for filtration applications as it allows for the entrapment of contaminants, such as PFAS and crude oil, using the mesopores without reducing the flux of the clean water through the macropores.⁷¹

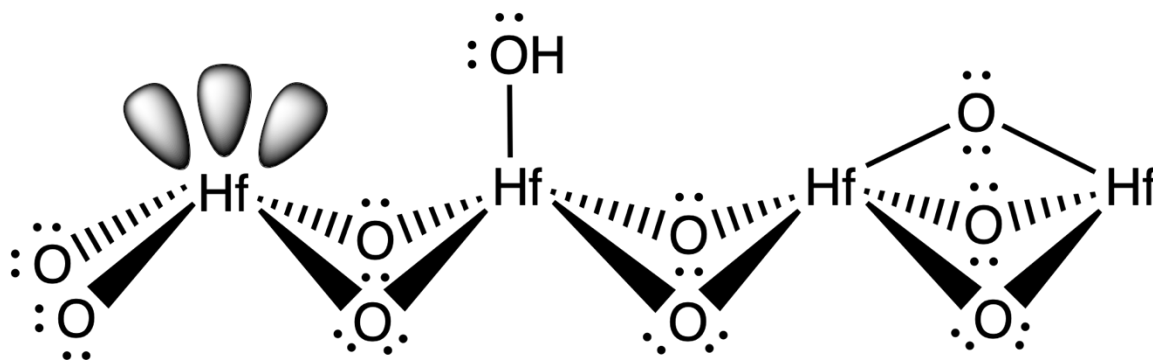


Figure 1.4 Illustrating active sites present on the surface of MHO; Lewis acid site (left), Brønsted acid site (center), and Brønsted base site (right).

Sol-gel Synthesis of Mesoporous Hafnium Oxide Ceramic Monoliths

Transition metal oxides possess ideal functional groups and have properties that make them stable and favorable for water remediation applications.⁷² Recently, sol-gel synthesis of free-standing monoliths of transition metal oxides have been explored for creating robust materials. Sol-gel synthesis involves the hydrolysis of a metal salt followed by polycondensation to form a ‘sol’. Then the particles form colloids that are slowly polymerized into a ‘gel’ which undergoes aging, washing, and heat treatment to form the

desired metal oxide.⁷³ Herein, the steps needed to form monoliths of mesoporous hafnium oxide (MHO) ceramics will be detailed. In the initial hydrolysis step we use Hafnium (IV) tetrachloride as the metal precursor. This is an exothermic reaction that produces hafnium oxihydride and hydrochloric acid as shown in **eq. 1.2**:



At this stage, *N*-methylformamide (NMF) is added as a porogen, it also affects the gelation and porosity of the final product which in turn affects the surface area and pore size. Once added to the solution, NMF hydrolyses to form formic acid and methyl ammonium which increases the pH of the solution and accelerates polycondensation resulting in phase separation.⁷⁴ The hydrolysis reaction of NMF is shown in **eq. 1.3** below:



The above process takes three days, then polyethylene oxide (PEO, MW 100,000) is added to further induce phase separation and start the formation of the network of pores.⁷⁵ Finally, propylene oxide (PPO) is added to induce polycondensation and gelation through an epoxide ring opening reaction as show in **eq. 1.4**.⁷⁶



The white gel was allowed to age for three days at 50°C. The gelation step determines the final shape and size of the monolith. The monolith was then washed with ultrapure water ($\geq 18.2 \text{ M}\Omega\cdot\text{cm}$), methanol, acetone, hexanes, and pentane to remove any excess reagents produced during the synthesis. This order of solvents was chosen based on polarity and miscibility of solvents. This order of solvents was also shown to prevent cracking of the monolith during the heating stage, specifically low surface tension solvents such as hexanes and pentanes have been used to reduce capillary tension during the heating stage.⁷⁷ After the solvent exchange, the monolith was heated in a muffle furnace starting at 50°C and slowly ramping all the way to

700°C as that is the temperature needed to form robust monoclinic hafnium oxide. A schematic summarizing the sol-gel synthesis process of MHO is illustrated in **Figure 1.5** below.

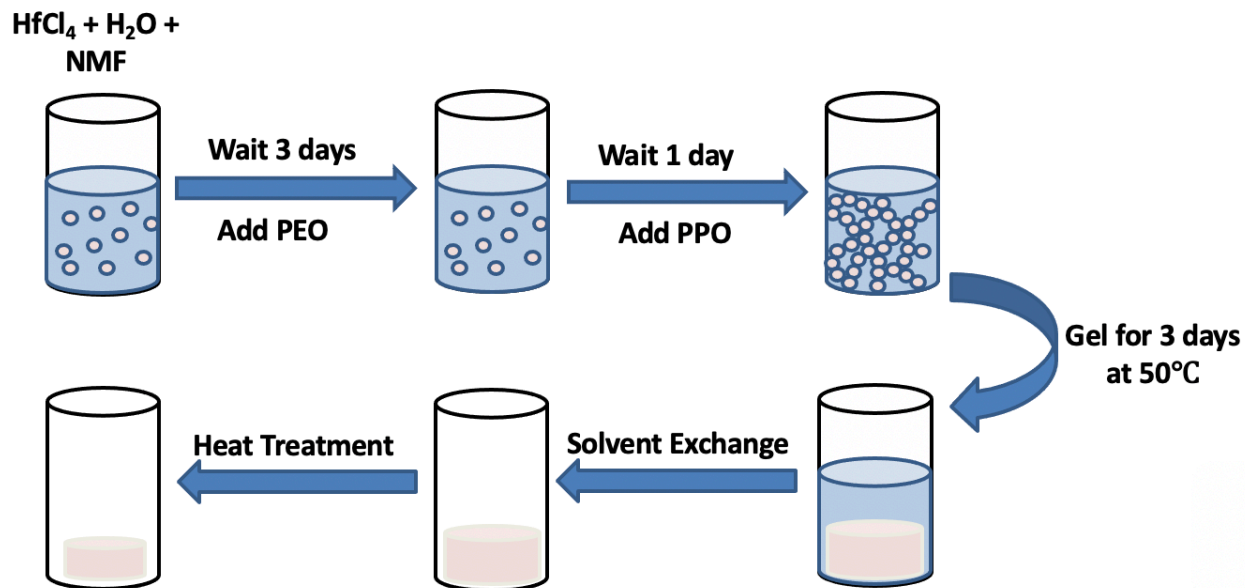


Figure 1.5 Schematic illustrating each step of the sol-gel synthesis of monolith of mesoporous hafnium oxide ceramic.

References

- 1 T. Oki and S. Kanae, Global Hydrological Cycles And World Water Resources, *Science* (80-.), 2006, **313**, 1068–1072.
- 2 A. M. Hamiche, A. B. Stambouli and S. Flazi, A Review Of The Water-Energy Nexus, *Renew. Sustain. Energy Rev.*, 2016, **65**, 319–331.
- 3 H. Hatzenbuehler and T. Centner, Regulation Of Water Pollution From Hydraulic Fracturing In Horizontally-Drilled Wells In The Marcellus Shale Region, USA, *Water*, 2012, **4**, 983–994.
- 4 S. Othumpangat and V. Castranova, in *Encyclopedia of Toxicology*, Elsevier, 2014, pp. 677–681.
- 5 S. Sarikoç, in *Diesel and Gasoline Engines*, IntechOpen, 2020.
- 6 I. M. K. Saadoun, in *Emerging Pollutants in the Environment - Current and Further Implications*,

- InTech, 2015.
- 7 E. S. Osuagwu and E. Olaifa, Effects Of Oil Spills On Fish Production In The Niger Delta, *PLoS One*, 2018, **13**, e0205114.
 - 8 N. Andrews, N. J. Bennett, P. Le Billon, S. J. Green, A. M. Cisneros-Montemayor, S. Amongin, N. J. Gray and U. R. Sumaila, Oil, Fisheries And Coastal Communities: A Review Of Impacts On The Environment, Livelihoods, Space And Governance, *Energy Res. Soc. Sci.*, 2021, **75**, 102009.
 - 9 B. S. Levy and W. J. Nassetta, The Adverse Health Effects Of Oil Spills: A Review Of The Literature And A Framework For Medically Evaluating Exposed Individuals, *Int. J. Occup. Environ. Health*, 2011, **17**, 161–168.
 - 10 T. J. Schoenbaum, Liability For Damages In Oil Spill Accidents: Evaluating The USA And International Law Regimes In The Light Of Deepwater Horizon, *J. Environ. Law*, 2012, **24**, 395–416.
 - 11 B. E. Ornitz and M. A. Champ, in *Oil Spills First Principles*, Elsevier, 2002, pp. 493–552.
 - 12 A. J. Pete, B. Bharti and M. G. Benton, Nano-Enhanced Bioremediation For Oil Spills: A Review, *ACS ES&T Eng.*, 2021, **1**, 928–946.
 - 13 P. E. Ndimele, A. O. Saba, D. O. Ojo, C. C. Ndimele, M. A. Anetekhai and E. S. Erondy, in *The Political Ecology of Oil and Gas Activities in the Nigerian Aquatic Ecosystem*, Elsevier, 2018, pp. 369–384.
 - 14 A. Dhaka and P. Chattopadhyay, A Review On Physical Remediation Techniques For Treatment Of Marine Oil Spills, *J. Environ. Manage.*, 2021, **288**, 112428.
 - 15 R. C. Prince, Oil Spill Dispersants: Boon Or Bane?, *Environ. Sci. Technol.*, 2015, **49**, 6376–6384.
 - 16 S. Kleindienst, J. H. Paul and S. B. Joye, Using Dispersants After Oil Spills: Impacts On The Composition And Activity Of Microbial Communities, *Nat. Rev. Microbiol.*, 2015, **13**, 388.

- 17 R. Almeda, C. Hyatt and E. J. Buskey, Toxicity Of Dispersant Corexit 9500A And Crude Oil To Marine Microzooplankton, *Ecotoxicol. Environ. Saf.*, 2014, **106**, 76–85.
- 18 M. Zamparas, D. Tzivras, V. Dracopoulos and T. Ioannides, Application Of Sorbents For Oil Spill Cleanup Focusing On Natural-Based Modified Materials: A Review, *Molecules*, 2020, **25**, 4522.
- 19 M. Husseien, A. A. Amer, A. El Maghraby and N. Hamedallah, Oil Spill Removal From Water By Using Corn Stalk: Factors Affecting Sorption Process, *Int. J. Environ. Waste Manag.*, 2015, **16**, 281.
- 20 A. Bazargan, J. Tan, C. W. Hui and G. McKay, Utilization Of Rice Husks For The Production Of Oil Sorbent Materials, *Cellulose*, 2014, **21**, 1679–1688.
- 21 R. Behnood, B. Anvaripour, N. Jaafarzadeh and M. Farasati, Oil Spill Sorption Using Raw And Acetylated Sugarcane Bagasse, *J. Cent. South Univ.*, 2016, **23**, 1618–1625.
- 22 M. R. Cherubin, D. M. da S. Oliveira, B. J. Feigl, L. G. Pimentel, I. P. Lisboa, M. R. Gmach, L. L. Varanda, M. C. Morais, L. S. Satiro, G. V. Popin, S. R. de Paiva, A. K. B. dos Santos, A. L. S. de Vasconcelos, P. L. A. de Melo, C. E. P. Cerri and C. C. Cerri, Crop Residue Harvest For Bioenergy Production And Its Implications On Soil Functioning And Plant Growth: A Review, *Sci. Agric.*, 2018, **75**, 255–272.
- 23 N. Kumar, S. S. Amritphale, J. C. Matthews and J. G. Lynam, Oil Spill Cleanup Using Industrial And Agricultural Waste-Based Magnetic Silica Sorbent Material: A Green Approach, *Green Chem. Lett. Rev.*, 2021, **14**, 632–639.
- 24 H. Li, L. Liu and F. Yang, Oleophilic Polyurethane Foams For Oil Spill Cleanup, *Procedia Environ. Sci.*, 2013, **18**, 528–533.
- 25 A. Alassod, M. Gibril, S. R. Islam, W. Huang and G. Xu, Polypropylene/Lignin Blend Monoliths Used As Sorbent In Oil Spill Cleanup, *Heliyon*, 2020, **6**, e04591.
- 26 T. A. Abdullah, T. Juzsakova, S. A. Hafad, R. T. Rasheed, N. Al-Jammal, M. A. Mallah, A. D.

- Salman, P. C. Le, E. Domokos and M. Aldulaimi, Functionalized Multi-Walled Carbon Nanotubes For Oil Spill Cleanup From Water, *Clean Technol. Environ. Policy*, , DOI:10.1007/s10098-021-02104-0.
- 27 H. Singh, N. Bhardwaj, S. K. Arya and M. Khatri, Environmental Impacts Of Oil Spills And Their Remediation By Magnetic Nanomaterials, *Environ. Nanotechnology, Monit. Manag.*, 2020, **14**, 100305.
- 28 S. Mendiratta and A. A. A. Ali, Recent Advances In Functionalized Mesoporous Silica Frameworks For Efficient Desulfurization Of Fuels, *Nanomaterials*, 2020, **10**, 1116.
- 29 A. Sadeghpour, F. Pirolt and O. Glatter, Submicrometer-Sized Pickering Emulsions Stabilized By Silica Nanoparticles With Adsorbed Oleic Acid, *Langmuir*, 2013, **29**, 6004–6012.
- 30 K. Karim, S. Guha and R. Beni, Potable Water In The United States, Contaminants And Treatment: A Review, *Voice Publ.*, 2020, **06**, 183–198.
- 31 C. Death, C. Bell, D. Champness, C. Milne, S. Reichman and T. Hagen, Per- And Polyfluoroalkyl Substances (PFAS) In Livestock And Game Species: A Review, *Sci. Total Environ.*, 2021, **774**, 144795.
- 32 M. J. Bentel, Y. Yu, L. Xu, Z. Li, B. M. Wong, Y. Men and J. Liu, Defluorination Of Per- And Polyfluoroalkyl Substances (PFASs) With Hydrated Electrons: Structural Dependence And Implications To PFAS Remediation And Management, *Environ. Sci. Technol.*, 2019, **53**, 3718–3728.
- 33 A. O. De Silva, C. N. Allard, C. Spencer, G. M. Webster and M. Shoeib, Phosphorus-Containing Fluorinated Organics: Polyfluoroalkyl Phosphoric Acid Diesters (DiPAPs), Perfluorophosphonates (PFPAAs), And Perfluorophosphinates (PFPIAs) In Residential Indoor Dust, *Environ. Sci. Technol.*, 2012, **46**, 12575–12582.
- 34 A. B. Lindstrom, Introduction to Per- and Polyfluoroalkyl Substances (PFAS) In Food Service

- Ware,
http://www.responsiblepurchasing.org/webinars/toxics_food_service_ware_webinar_slides_111617.pdf, (accessed October 10, 2018).
- 35 I. Ross, J. McDonough, J. Miles, P. Storch, P. Thelakkat Kochunarayanan, E. Kalve, J. Hurst, S. S. Dasgupta and J. Burdick, A Review Of Emerging Technologies For Remediation Of PFASs, *Remediat. J.*, 2018, **28**, 101–126.
- 36 R. C. Buck, J. Franklin, U. Berger, J. M. Conder, I. T. Cousins, P. de Voogt, A. A. Jensen, K. Kannan, S. A. Mabury and S. P. van Leeuwen, Perfluoroalkyl And Polyfluoroalkyl Substances In The Environment: Terminology, Classification, And Origins, *Integr. Environ. Assess. Manag.*, 2011, **7**, 513–541.
- 37 M. H. Russell, H. Nilsson and R. C. Buck, Elimination Kinetics Of Perfluorohexanoic Acid In Humans And Comparison With Mouse, Rat And Monkey, *Chemosphere*, 2013, **93**, 2419–2425.
- 38 G. W. Olsen, J. M. Burris, D. J. Ehresman, J. W. Froehlich, A. M. Seacat, J. L. Butenhoff and L. R. Zobel, Half-Life Of Serum Elimination Of Perfluorooctanesulfonate, Perfluorohexanesulfonate, And Perfluorooctanoate In Retired Fluorochemical Production Workers, *Environ. Health Perspect.*, 2007, **115**, 1298–1305.
- 39 N. M. Brennan, A. T. Evans, M. K. Fritz, S. A. Peak and H. E. von Holst, Trends In The Regulation Of Per- And Polyfluoroalkyl Substances (PFAS): A Scoping Review, *Int. J. Environ. Res. Public Health*, 2021, **18**, 10900.
- 40 J. Glüge, M. Scheringer, I. T. Cousins, J. C. DeWitt, G. Goldenman, D. Herzke, R. Lohmann, C. A. Ng, X. Trier and Z. Wang, An Overview Of The Uses Of Per- And Polyfluoroalkyl Substances (PFAS), *Environ. Sci. Process. Impacts*, 2020, **22**, 2345–2373.
- 41 W. S. Dean, H. A. Adejumo, A. Caiati, P. M. Garay, A. S. Harmata, L. Li, E. E. Rodrigues and S. Sundar, Policy Analysis: A Framework For Regulation Of New And Existing PFAS By EPA, *J.*

Sci. Policy Gov.

- 42 A. Cordner, V. Y. De La Rosa, L. A. Schaidler, R. A. Rudel, L. Richter and P. Brown, Guideline Levels For PFOA And PFOS In Drinking Water: The Role Of Scientific Uncertainty, Risk Assessment Decisions, And Social Factors, *J. Expo. Sci. Environ. Epidemiol.*, 2019, **29**, 157–171.
- 43 OEHHA, *Proposed Public Health Goals for Perfluorooctanoic Acid and Perfluorooctane Sulfonic Acid in Drinking Water*, 2021.
- 44 Z. Li, H. Lu, L. Ren and L. He, Experimental And Modeling Approaches For Food Waste Composting: A Review, *Chemosphere*, 2013, **93**, 1247–1257.
- 45 S. E. Vergara and W. L. Silver, Greenhouse Gas Emissions From Windrow Composting Of Organic Wastes: Patterns And Emissions Factors, *Environ. Res. Lett.*, 2019, **14**, 124027.
- 46 X. F. Lou and J. Nair, The Impact Of Landfilling And Composting On Greenhouse Gas Emissions – A Review, *Bioresour. Technol.*, 2009, **100**, 3792–3798.
- 47 J. Barthod, C. Rumpel and M.-F. Dignac, Composting With Additives To Improve Organic Amendments. A Review, *Agron. Sustain. Dev.*, 2018, **38**, 17.
- 48 C. O. Onwosi, V. C. Igbokwe, J. N. Odimba, I. E. Eke, M. O. Nwankwoala, I. N. Iroh and L. I. Ezeogu, Composting Technology In Waste Stabilization: On The Methods, Challenges And Future Prospects, *J. Environ. Manage.*, 2017, **190**, 140–157.
- 49 V. Siracusa, P. Rocculi, S. Romani and M. D. Rosa, Biodegradable Polymers For Food Packaging: A Review, *Trends Food Sci. Technol.*, 2008, **19**, 634–643.
- 50 X. Lim, Can Microbes Save Us From PFAS?, *ACS Cent. Sci.*, 2021, **7**, 3–6.
- 51 E. Shahsavari, D. Rouch, L. S. Khudur, D. Thomas, A. Aburto-Medina and A. S. Ball, Challenges And Current Status Of The Biological Treatment Of PFAS-Contaminated Soils, *Front. Bioeng. Biotechnol.*, , DOI:10.3389/fbioe.2020.602040.

- 52 Y. Yu, K. Zhang, Z. Li, C. Ren, J. Chen, Y.-H. Lin, J. Liu and Y. Men, Microbial Cleavage Of C–F Bonds In Two C 6 Per- And Polyfluorinated Compounds Via Reductive Defluorination, *Environ. Sci. Technol.*, 2020, **54**, 14393–14402.
- 53 S. Huang and P. R. Jaffé, Defluorination Of Perfluorooctanoic Acid (PFOA) And Perfluorooctane Sulfonate (PFOS) By Acidimicrobium Sp. Strain A6, *Environ. Sci. Technol.*, 2019, **53**, 11410–11419.
- 54 B. Ji, P. Kang, T. Wei and Y. Zhao, Challenges Of Aqueous Per- And Polyfluoroalkyl Substances (PFASs) And Their Foreseeable Removal Strategies, *Chemosphere*, 2020, **250**, 126316.
- 55 L. Zhao, J. Bian, Y. Zhang, L. Zhu and Z. Liu, Comparison Of The Sorption Behaviors And Mechanisms Of Perfluorosulfonates And Perfluorocarboxylic Acids On Three Kinds Of Clay Minerals, *Chemosphere*, 2014, **114**, 51–58.
- 56 E. Gagliano, M. Sgroi, P. P. Falciglia, F. G. A. Vagliasindi and P. Roccaro, Removal Of Poly- And Perfluoroalkyl Substances (PFAS) From Water By Adsorption: Role Of PFAS Chain Length, Effect Of Organic Matter And Challenges In Adsorbent Regeneration, *Water Res.*, 2020, **171**, 115381.
- 57 C. J. Liu, D. Werner and C. Bellona, Removal Of Per- And Polyfluoroalkyl Substances (PFASs) From Contaminated Groundwater Using Granular Activated Carbon: A Pilot-Scale Study With Breakthrough Modeling, *Environ. Sci. Water Res. Technol.*, 2019, **5**, 1844–1853.
- 58 V. Franke, M. Ullberg, P. McCleaf, M. Wålander, S. J. Köhler and L. Ahrens, The Price Of Really Clean Water: Combining Nanofiltration With Granular Activated Carbon And Anion Exchange Resins For The Removal Of Per- And Polyfluoroalkyl Substances (PFASs) In Drinking Water Production, *ACS ES&T Water*, 2021, **1**, 782–795.
- 59 M. Van den Bergh, A. Krajnc, S. Voorspoels, S. R. Tavares, S. Mullens, I. Beurroies, G. Maurin, G. Mali and D. E. De Vos, Highly Selective Removal Of Perfluorinated Contaminants By

- Adsorption On All-Silica Zeolite Beta, *Angew. Chemie*, 2020, **132**, 14190–14194.
- 60 Y. Wu, Y. Li, A. Tian, K. Mao and J. Liu, Selective Removal Of Perfluorooctanoic Acid Using Molecularly Imprinted Polymer-Modified TiO₂ Nanotube Arrays, *Int. J. Photoenergy*, 2016, **2016**, 1–10.
- 61 F. Wang, C. Liu and K. Shih, Adsorption Behavior Of Perfluorooctanesulfonate (PFOS) And Perfluorooctanoate (PFOA) On Boehmite, *Chemosphere*, 2012, **89**, 1009–1014.
- 62 B. N. Nzeribe, M. Crimi, S. Mededovic Thagard and T. M. Holsen, Physico-Chemical Processes For The Treatment Of Per- And Polyfluoroalkyl Substances (PFAS): A Review, *Crit. Rev. Environ. Sci. Technol.*, 2019, **49**, 866–915.
- 63 S. Sukeesan, N. Boontanon and S. K. Boontanon, Improved Electrical Driving Current Of Electrochemical Treatment Of Per- And Polyfluoroalkyl Substances (PFAS) In Water Using Boron-Doped Diamond Anode, *Environ. Technol. Innov.*, 2021, **23**, 101655.
- 64 C. Fang, M. Megharaj and R. Naidu, Electrochemical Advanced Oxidation Processes (EAOP) To Degrade Per- And Polyfluoroalkyl Substances (PFASs), *J. Adv. Oxid. Technol.*, , DOI:10.1515/jaots-2017-0014.
- 65 R. A. Marcus, On The Theory Of Electron-Transfer Reactions. VI. Unified Treatment For Homogeneous And Electrode Reactions, *J. Chem. Phys.*, 1965, **43**, 679–701.
- 66 J. N. Uwayezu, I. Carabante, T. Lejon, P. van Hees, P. Karlsson, P. Hollman and J. Kumpiene, Electrochemical Degradation Of Per- And Poly-Fluoroalkyl Substances Using Boron-Doped Diamond Electrodes, *J. Environ. Manage.*, 2021, **290**, 112573.
- 67 B. P. Chaplin, The Prospect Of Electrochemical Technologies Advancing Worldwide Water Treatment, *Acc. Chem. Res.*, 2019, **52**, 596–604.
- 68 S. Liang, R. “David” Pierce, H. Lin, S.-Y. D. Chiang and Q. “Jack” Huang, Electrochemical Oxidation Of PFOA And PFOS In Concentrated Waste Streams, *Remediat. J.*, 2018, **28**, 127–134.

- 69 K. Wang, D. Huang, W. Wang, Y. Ji and J. Niu, Enhanced Perfluorooctanoic Acid Degradation By Electrochemical Activation Of Peroxymonosulfate In Aqueous Solution, *Environ. Int.*, 2020, **137**, 105562.
- 70 J. De Roo, F. Van den Broeck, K. De Keukeleere, J. C. Martins, I. Van Driessche and Z. Hens, Unravelling The Surface Chemistry Of Metal Oxide Nanocrystals, The Role Of Acids And Bases, *J. Am. Chem. Soc.*, 2014, **136**, 9650–9657.
- 71 R. Kohns, N. Anders, D. Enke and U. Tallarek, Influence Of Pore Space Hierarchy On The Efficiency Of An Acetylcholinesterase-Based Support For Biosensorics, *Adv. Mater. Interfaces*, 2021, **8**, 2000163.
- 72 G. A. Seisenbaeva, G. Daniel, V. G. Kessler and J.-M. Nedelec, General Facile Approach To Transition-Metal Oxides With Highly Uniform Mesoporosity And Their Application As Adsorbents For Heavy-Metal-Ion Sequestration, *Chem. - A Eur. J.*, 2014, **20**, 10732–10736.
- 73 R. Yarbrough, K. Davis, S. Dawood and H. Rathnayake, A Sol–Gel Synthesis To Prepare Size And Shape-Controlled Mesoporous Nanostructures Of Binary (II–VI) Metal Oxides, *RSC Adv.*, 2020, **10**, 14134–14146.
- 74 B. Gaweł, K. Gaweł and G. Øye, Sol-Gel Synthesis Of Non-Silica Monolithic Materials, *Materials (Basel)*, 2010, **3**, 2815–2833.
- 75 J.-L. Blin, A. Léonard, Z.-Y. Yuan, L. Gigot, A. Vantomme, A. K. Cheetham and B.-L. Su, Hierarchically Mesoporous/Macroporous Metal Oxides Templated From Polyethylene Oxide Surfactant Assemblies, *Angew. Chemie Int. Ed.*, 2003, **42**, 2872–2875.
- 76 A. E. Danks, S. R. Hall and Z. Schnepf, The Evolution Of ‘Sol–Gel’ Chemistry As A Technique For Materials Synthesis, *Mater. Horizons*, 2016, **3**, 91–112.
- 77 H. Colón, X. Zhang, J. K. Murphy, J. G. Rivera and L. A. Colón, Allyl-Functionalized Hybrid Silica Monoliths, *Chem. Commun.*, 2005, 2826.

2 Chapter 2: Adsorption of Crude Oil from Crude Oil–Water

Emulsion by Mesoporous Hafnium Oxide Ceramics

Abstract

Crude oil spills are extremely toxic and cause harm to marine wildlife, people living in the area, and is extremely difficult to clean-up. Dispersants applied after an oil spill convert the oil on the surface to smaller droplets that travel deeper into the ocean, causing more damage to wildlife and marine ecosystems. We report a mesoporous hafnium oxide (MHO) ceramic synthesized *via* a sol–gel process that has exhibited 99.9% removal capacity of crude oil from an oil-in-water emulsion at a concentration of 3 mg mL⁻¹. The as-prepared MHO ceramic was regenerated after crude oil sequestration *via* calcination at 800 °C under ambient conditions. The scalability of the synthetic method and thermal stability of the MHO ceramic material makes it a promising, underexplored, and reusable adsorbent for efficient oil spill clean-up.

Introduction

Oil spills are a serious threat to marine life in an already vulnerable biosphere. For example, increased CO₂ emissions have caused elevated ocean temperatures, leading to coral reef bleaching and mortality.¹ Furthermore, local wildlife such as birds have also been adversely impacted by hypothermia as their feathers become covered in crude oil.² Humans can also be affected by oil spills through respiratory problems, skin irritation, and even cancer depending on the length and type of exposure.³ Over 5 million tons of crude oil are transported annually by sea, and introduced to coastal waters that are extremely vulnerable to oil spills. Additionally, waste disposal, energy sources, accidents, and the production of oil are sources of water contamination. In 2010, the Deepwater horizon spill released 5 million barrels of oil worth 6 billion USD.⁴ More recently, the Sanchi spill in 2018 in East China released ~1 million barrels of oil.⁵

As a response to oil spills, dispersants such as hydrophobically modified chitosan⁶ and halloysite clay nanotubes⁷ are sprayed over the spill area to prevent oil from spreading on the surface. These dispersants are composed of hydrophilic and lipophilic active sites and surround oil with the hydrophilic head facing outwards which helps stabilize the oil into small droplets. This allows for the oil droplets to move below the surface, making it seem like the surface is clean. However, this in turn leads to oil sedimentation in the ocean bed and negatively impacts aquatic life since the oil particles are not adsorbed by dispersants for subsequent removal.⁸⁻¹¹

Adsorption is a preferred clean-up method because it is affordable, facile, and environmentally feasible.¹² There is a growing interest in the use of sorbent and reusable materials that are non-toxic to avoid further contamination of water. Some examples include agricultural waste (banana peels, palm fiber, rice husks),¹²⁻¹⁴ polymeric materials coated on foams and sponges,¹⁵⁻¹⁸ and aerogels made from carbon based materials such as cellulose¹⁹ and graphene.²⁰ However, the lack of mechanical stability of these materials in harsh chemical environments limits their application.²¹ Porous metal oxide ceramic materials such as silica, titania, hafnia, and zirconia are interesting candidates due to their relatively hydrophilic surfaces, which gives these materials particular advantages over hydrophobic ones. Their hydrophilic properties allow water to permeate, which prevents clogging by viscous and heavy oils. These materials also prevent the formation of a water layer under an oil layer as it will allow the water to permeate.²²⁻²⁴

MHO monoliths with pores of different length scales are an attractive alternative to particles or pressed pellets, as they are thermally stable, mechanically robust, and allow for higher liquid mass transfer than powders.²⁵⁻²⁸ The density of the MHO is slightly greater than that of water 1.1 g cm^{-3} . This characteristic, in addition to its hydrophilic nature, leads to strong enough interaction with water molecules to break surface tension and sink below the surface. This lack of buoyancy hinders the suitability for using MHO in batch adsorption experiments, although it is well suited for fixed-bed filtration experiments.

Hafnium oxide, a group IV transition metal oxide, is chemically and thermally stable due to the high coordination number of hafnium. Hafnium can coordinate to seven oxygen atoms, whereas silicon can only coordinate to four. The strength of the Hf-O bonds as well as the ionicity makes hafnium oxide resistant to chemical degradation in extreme pH conditions, a highly desirable property for materials that will be exposed to harsh oil-removal conditions. Additionally, hafnium oxide contains three active sites on the surface: Brønsted base sites which accept a proton in basic media, Brønsted acid sites which donate a proton in acidic media, and Lewis acid sites originating from unoccupied hafnium d orbitals as shown in **Figure 2.1**. This broad network of bonding further contributes to the mechanical strength of hafnium oxide.²⁹

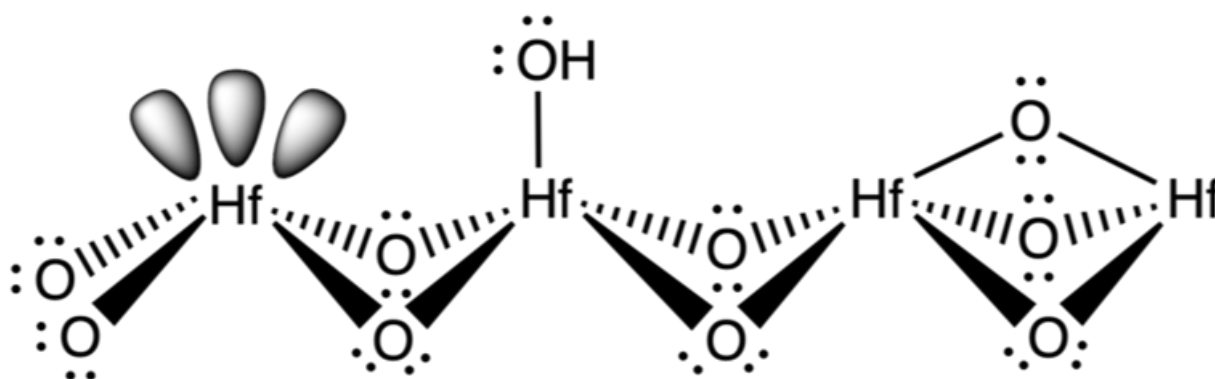


Figure 2.1 Three main active sites on the surface of hafnium oxide: Lewis acid site (left), Brønsted acid site (middle), and Brønsted base site (right).

The objective of this study is to investigate the efficiency of MHO for crude oil removal from crude oil-in-water emulsions. Sol-gel synthesis has been used for the synthesis of MHO to be integrated as a filter to sequester crude oil from crude oil-in-water emulsions in a wide pH range. Liquid aliquots have been analysed using chromatography and spectroscopy techniques. Regeneration of the MHO was studied through calcination and thermogravimetric analysis.

Materials & Methods

Chemicals and materials

Hafnium(IV) tetrachloride (HfCl_4 , 98%), methanol, acetone, hexanes, and pentane were all HPLC Plus (>99.9%). Sulfuric acid (95.0–98.0%), hydrochloric acid (HCl, 35.0–37.0%), deuterated methanol (CD_3OD), and deuterated chloroform (CDCl_3) with tetramethylsilane (TMS) (99.95% + 0.05%) were used as purchased from Sigma-Aldrich. Poly(ethylene oxide) (MW 100 000) was purchased from Polysciences Inc. Propylene oxide (99.5%) was purchased from Acros Organics. *N*-Methyl formamide (99%) and sodium hydroxide pellets (NaOH, 98%) were purchased from Alfa Aesar. Light crude oil (API > 31) was obtained from an un-disclosed oil refinery within northern California. Ultrapure water (resistivity >18.2 M Ω) used for synthesis and crude oil water mixes was obtained from a Thermo Scientific Barnstead E-Pure Ultrapure water purification system. Various porous materials were purchased for comparison purposes including melamine sponge (He Andi, pore size 150 μm), Whatman grade 1 cellulose filter paper (Sigma-Aldrich, pore size 11 μm), and a commercial wine filter (Buon Vino, no. 2, pore size 1 μm).

2.1.1 Synthesis of MHO ceramic monolith

MHO ceramic monoliths were synthesized using the sol–gel method.³⁰ Prior to MHO synthesis, 20 mL scintillation glass vials were treated in sequence with 0.1 M NaOH for 1 hour, 0.1 M HCl for 1 hour, and Rain-x overnight. After removing the Rain-x, vials were rinsed with methanol three times and dried in an oven. Herein, we use hafnium(IV) chloride dissolved in ultrapure water in the hydrolysis step. *N*-Methylformamide (NMF) was added as a porogen, to increase the solution pH, and induce phase separation. Polyethylene oxide (PEO, MW 100 000) was added to create a strong pore network. Additionally, propylene oxide was added to induce polymerization, turning the clear liquid to a white gel. The gel was then aged at 50 °C for three days in air. The monolith was washed with ultrapure water, methanol, acetone, hexanes, and pentane to remove any excess reagents left after synthesis. Lastly, the sample underwent heat treatment

in air to 700 °C which yields a crystalline white monolithic ceramic.³⁰ The melamine sponge, cellulose filter paper, and a commercial wine filter with the same pore size as MHO were used for comparison. All materials were tested by vacuum filtration of a crude oil-in-water emulsion.

2.1.2 Structural Characterization of MHO Ceramic

After the synthesis, the crystalline structure and phase purity of the material was determined by powder X-ray diffraction (XRD) using a Bruker D8 Advance diffractometer with Cu K α radiation (1.5406 Å). Experimentally obtained diffraction patterns were then compared to literature patterns from the Inorganic Crystal Structure Database (ICSD) to confirm the structure. The mesostructure of the material was determined by a Thermofisher Quattro Environmental scanning electron microscope (ESEM). The sample was placed on copper tape and operated at an accelerating voltage of 10 keV under low vacuum. The surface of the MHO ceramic was analysed before filtration, after filtration, and after heating to remove crude oil (800 °C) using Fourier transform infrared (FTIR) spectroscopy. The Bruker Tensor 27 FTIR was equipped with an attenuated total reflectance (ATR) pike accessory. The experiment was performed using 16 scans, a resolution of 2 cm⁻¹, and a spectral range of 400–4000 cm⁻¹. Thermogravimetric analysis (TGA) was done using a NETSCH STA 449F3 instrument under high purity argon. It was heated from 20 °C to 800 °C at a rate of 3.0 °C min⁻¹.

2.1.3 Oil Sequestration and MHO Ceramic Regeneration

In a typical oil sequestration experiment, crude oil was mixed with ultrapure water in a vial *via* sonication (Branson 8800, 40 kHz, ambient conditions) for 30 minutes to prepare the oil-in-water emulsion (2–3 mg mL⁻¹, pH 1, 7, and 13).³¹ Sodium hydroxide and sulfuric acid were added to adjust the pH of the solution before adding the crude oil. The MHO ceramic monolith (0.2–0.4 g) was placed directly under the tip of a funnel using a shrinking tube as shown in **Figure 2.2a**. The funnel was then placed in a vacuum filtration setup as shown in **Figure 2.2b**. As previously mentioned, the hydrophilic nature of MHO as well as its

bimodal pore network made it an ideal candidate for filtration of crude oil-in-water emulsions, rather than for adsorption in a batch-type system. The crude oil-in-water emulsion was analysed before and after filtration for comparison. The filtration procedure was repeated with various porous materials such as melamine sponge, grade 1 cellulose filter paper, and commercial wine filter. The MHO ceramic was regenerated after filtration by calcination in air at 800 °C for 10 minutes.

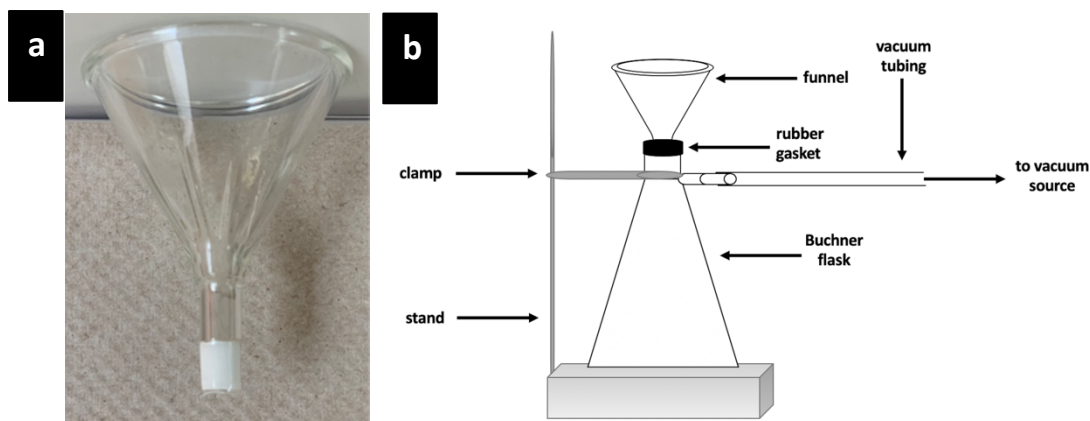


Figure 2.2 a) Funnel with MHO ceramic attached using shrinking tube, b) Experimental set up for oil sequestration experiment.

Qualitative and Quantitative Analysis of Oil Sequestration

The crude oil-in-water emulsion was analysed for crude oil concentration before and after filtration using an Agilent 6890 gas chromatograph equipped with a single quadrupole 5973 mass selective detector. In order to prepare samples suitable for GC-MS the liquids were extracted in pentane. A liquid-liquid extraction was done using 5 mL of the crude oil-in-water emulsion before or after filtration with 2 mL of pentane. The sample was placed in a glass centrifuge tube and centrifuged at 4500 rpm for 30 minutes. The pentane layer was injected in the GC. Compounds were separated on a Chrompack CP5860 (30 m, 0.25 mm ID, 0.25 μm). The chromatograph oven was operated from 40 °C to 300 °C rising at a rate of 10 °C min^{-1} . Helium was used as the carrier gas operating at a pressure of 6.7 psi. An injection volume of 1 μL was used and the injection temperature was 300 °C.³² The mass spectrometer source temperature was 230

°C and the quadrupole temperature was set to 180 °C. The range of ionization was from 50.00 amu to 800.00 amu. The GC provides a qualitative approach to assess removal efficiencies. Nuclear magnetic resonance (NMR) spectroscopy was used for quantitation. ¹H NMR spectroscopy was performed on a Bruker 400 MHz spectrometer. Calibrations were performed with various concentrations of crude oil-in-water emulsions. 100 μL of the emulsion was added to 695 μL of deuterated methanol and 5 μL of CDCl₃ with TMS as an internal standard and mixed well. 400 μL of this matrix is placed in a 300 MHz Wilmad NMR tube for analysis. A presaturation method was used to suppress the signal of water and to allow visualization of the analyte peaks of interest. The area under the crude oil peaks is used to create a calibration to quantitatively determine the amount of oil removed by the material. To calculate the percent removal of crude oil we use **eq. 2.1**:

$$\% \text{ Removal} = \frac{C_0 - C}{C_0} \times 100 \text{ (eq. 2.1)}$$

Where C_0 is the initial concentration of crude oil in water before filtration (mg/mL) and C is the concentration of crude oil in the filtrate.

Results and Discussion

Crystal Structure and Morphology of MHO Ceramic

The MHO ceramic monolith obtained after synthesis is shown in **Figure 2.3a**. The size and shape depend on the gelation vessel, which in this case was a 20 mL scintillation glass vial. **Figure 2.3b** depicts the MHO ceramic bimodal distribution comprised of a network of macropores and mesopores. The macropores are interconnected and appear to be approximately 1.0 μm in diameter based on the SEM. The monoclinic crystalline structure was confirmed by XRD and compared to literature values as shown in **Figure 2.3c**. In comparison, the SEM image for the melamine sponge is shown in **Figure 2.4**. The melamine sponge appears to have a network of macropores that are about 150 μm in diameter, significantly larger than MHO.

The SEM image of the grade 1 cellulose filter paper shown in **Figure 2.5** illustrates fibers stacked on each other rather than a network of pores. The SEM image of the Buon Vino wine filter shown in **Figure 2.6** illustrates cellulose-based fibers stacked on each other, diatoms, and parts that appear to have smaller circular macropores that are less than 1 μm in diameter.

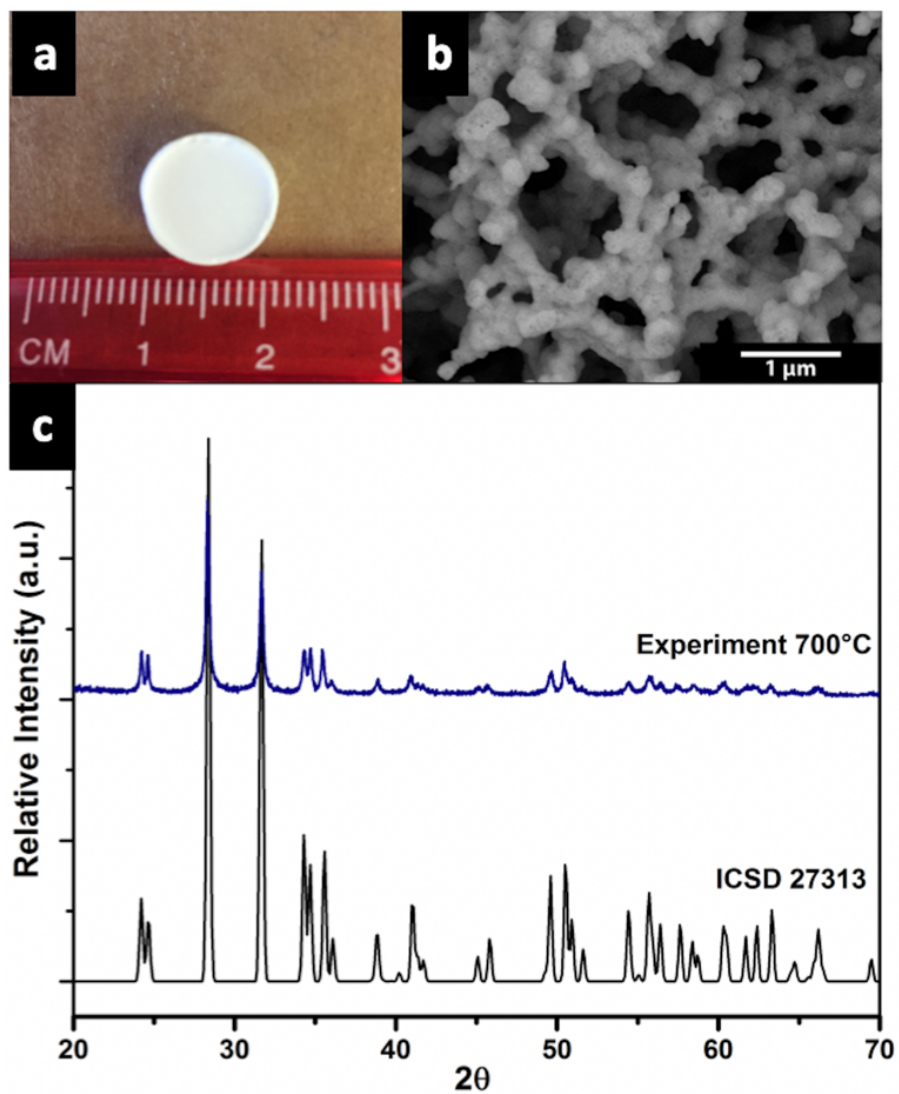


Figure 2.3 a) Free standing MHO ceramic with a diameter of 1 cm, b) SEM image of MHO ceramic illustrating network of macropores and mesopores, c) XRD pattern with major diffraction peaks indexed for MHO ceramic (top) overlaid with the published spectrum for MHO with heat treatment at 700 °C (bottom, ICSD Collection Code 27313).

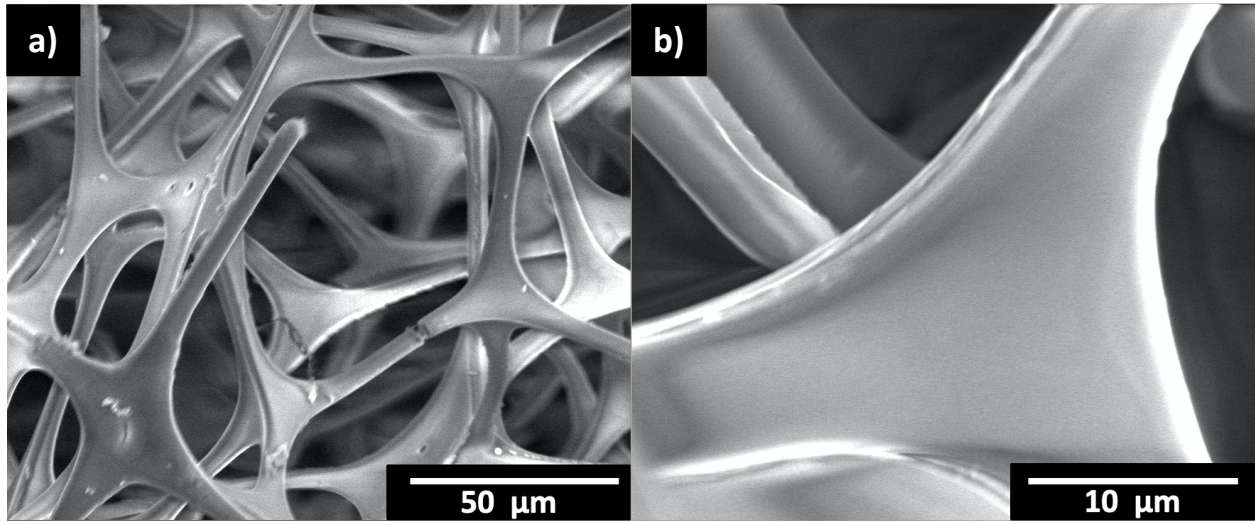


Figure 2.4 a) Low magnification and b) high magnification SEM image of melamine sponge purchased from He Andi used in filtration of crude oil-water emulsions.

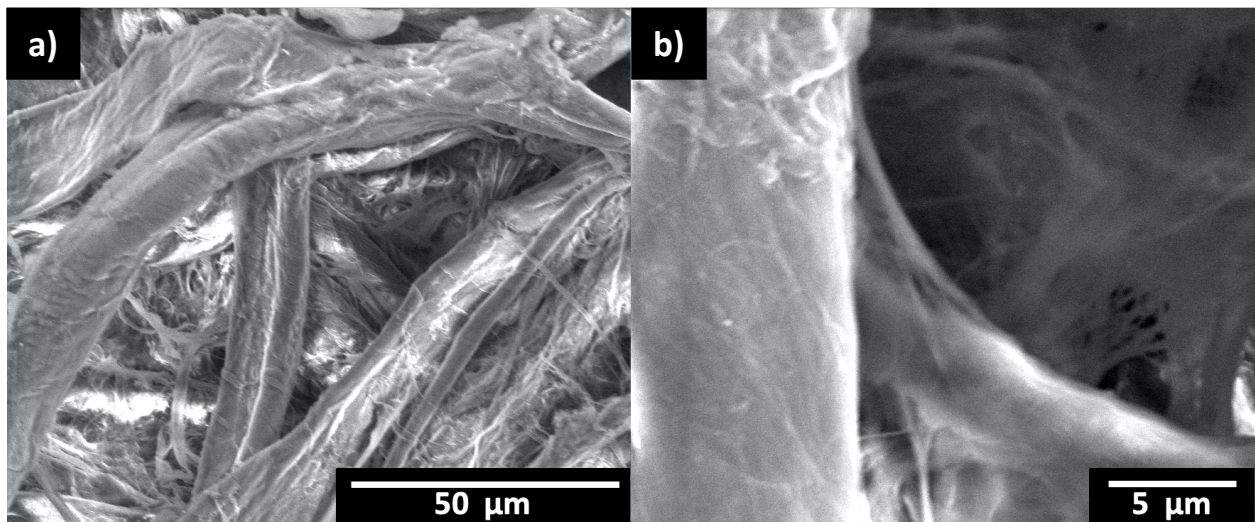


Figure 2.5 a) Low magnification and b) high magnification SEM image of grade 1 cellulose filter paper purchased from Sigma-Aldrich used in filtration of crude oil-water emulsions.

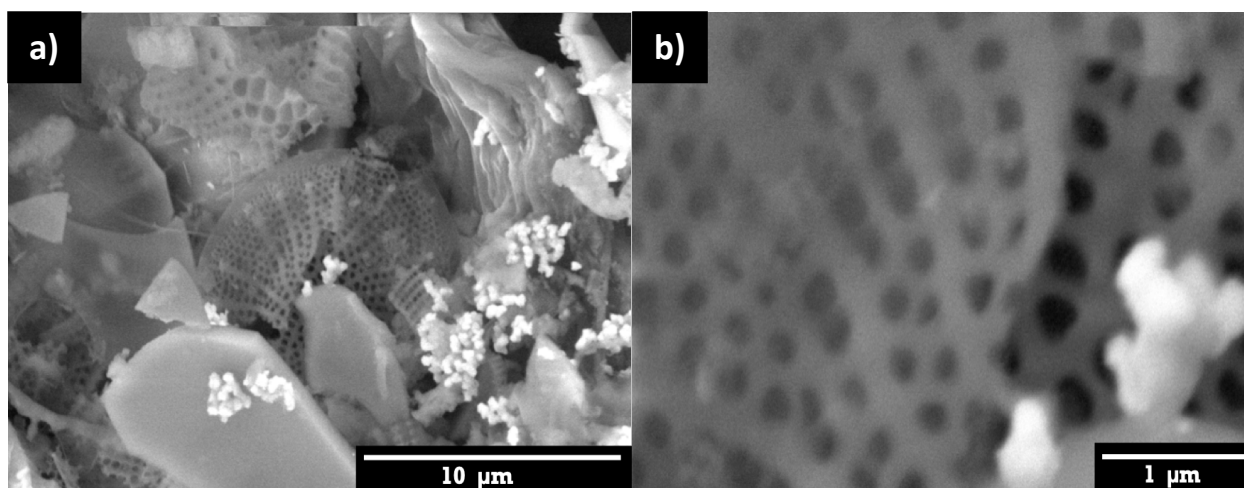


Figure 2.6 a) Low magnification and b) high magnification SEM image of wine filter purchased from Buon Vino used in filtration of crude oil-water emulsions.

Determination of Oil Concentrations Sequestered

To determine the potential of MHO ceramics to sequester oil mixtures of $2\text{--}3\text{ mg mL}^{-1}$ of crude oil in water were prepared. These concentrations are relevant but slightly higher than typical oil spill concentrations.³³⁻

³⁶ In **Figure 2.7a**, we observe a significant reduction in turbidity after filtration was performed using MHO ceramics. GC-MS was used to experimentally support the observation that the oil-in-water emulsion became less turbid after filtration. The resulting chromatogram in **Figure 2.7b** shows that prior to filtration there are numerous peaks at different relative intensities corresponding to various components of the crude oil mainly hydrocarbon chains ranging from C11 to C34. For comparison purposes, filtration with a cellulose-based filter paper and a melamine sponge was performed. As shown in **Figure 2.7b**, all crude oil characteristic peaks were still present after filtrations with each of the materials at similar retention times but with lower intensities. Remarkably, filtrations using MHO ceramic and the commercial wine filter (pore size $1\text{ }\mu\text{m}$) yielded completely clear liquids and there were no crude oil characteristic peaks which is indicative of near 100% removal of crude oil. Similar results were observed with MHO ceramic and the commercial wine filter at extreme acidic (pH 1) and basic conditions (pH 13) as shown in **Figure 2.8** and

Figure 2.9 respectively. To confirm and quantify this near 100% removal of crude oil, the liquid samples were analysed using ^1H NMR spectroscopy.

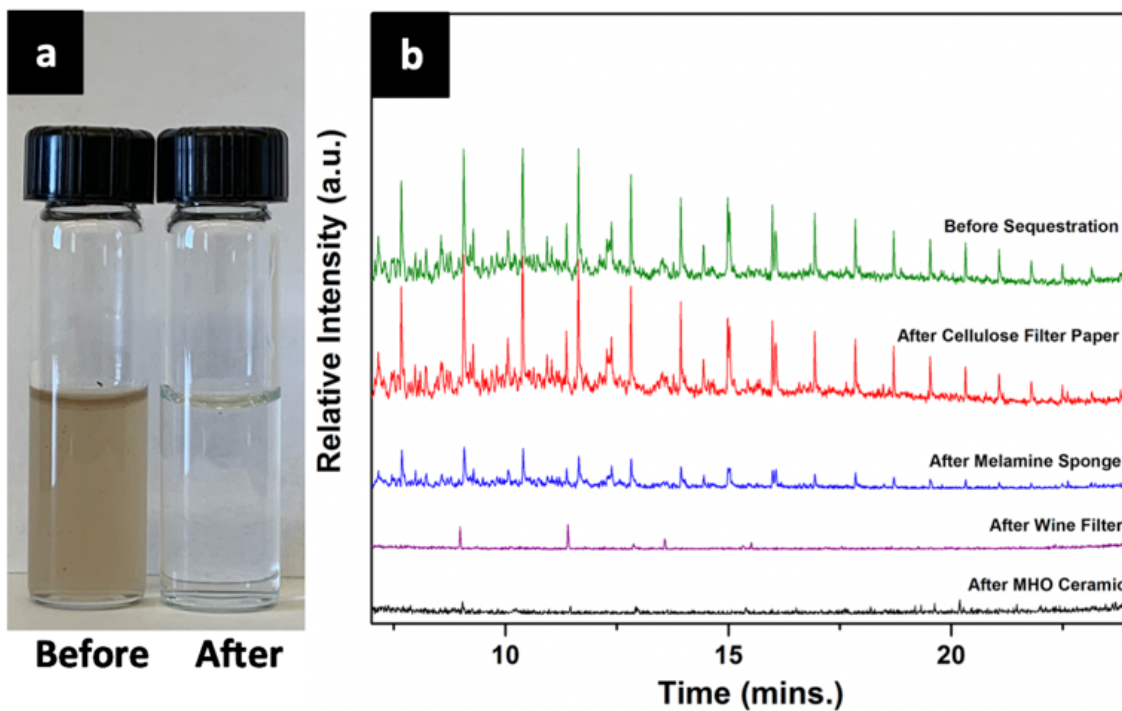


Figure 2.7 a) Image of crude oil-in-water emulsion in vials before and after filtration via MHO ceramic monolith in neutral pH, b) overlay GC-MS chromatograms of crude oil-in-water emulsion before sequestration and recovered liquid after sequestration using grade 1 cellulose filter paper, melamine sponge, commercial wine filter, and MHO ceramic monolith.

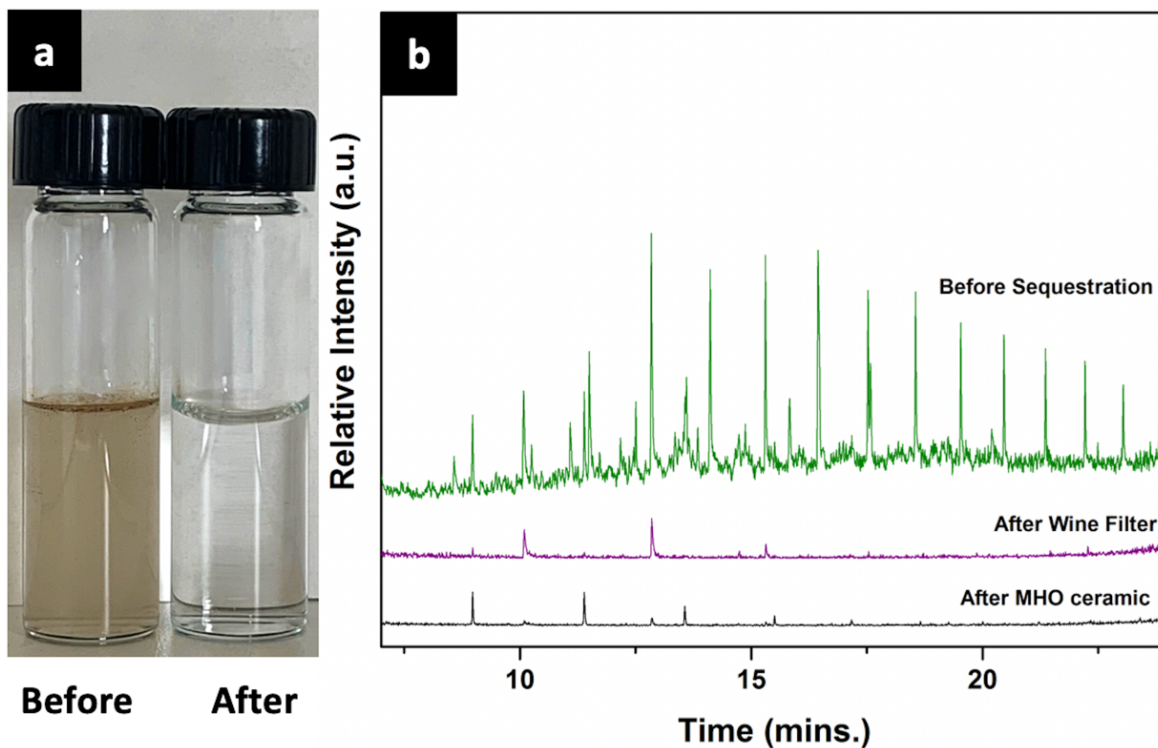


Figure 2.8 a) Image of liquid in vials before and after filtration via MHO ceramic monolith in acidic pH, b) Overlaid GC-MS chromatograms of liquid-oil mixture before sequestration (green) and recovered liquid after sequestration using commercial wine filter (purple) and MHO ceramic monolith (black).

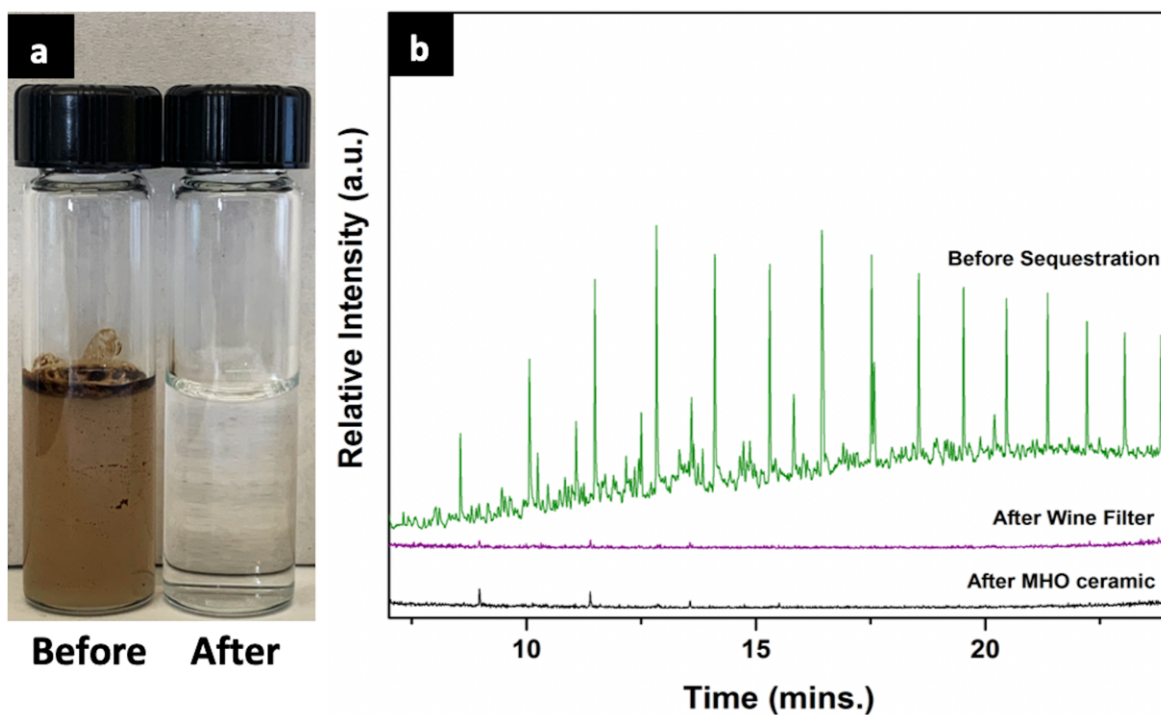


Figure 2.9 a) Image of liquid in vials before and after filtration via MHO ceramic monolith in basic pH, b) Overlaid GC-MS chromatograms of liquid-oil mixture before sequestration (green) and recovered liquid after sequestration using commercial wine filter (purple) and MHO ceramic monolith (black).

Figure 2.10a shows the MHO ceramic before sequestration and **Figure 2.10b** shows the MHO ceramic after sequestration in neutral pH. **Figure 2.10c** illustrates the ^1H NMR spectra detailing crude oil-in-water emulsion before and after filtration. From **Figure 2.10c** we observe crude oil signals at 0.9 ppm for alkyl terminal methyl groups ($\text{R}-\text{CH}_3$) and 1.3 ppm for alkyl methylene groups ($\text{R}-\text{CH}_2-\text{R}$) in the crude oil-in-water emulsion before filtration.^{37,38} After filtration the peak at 0.9 ppm was no longer present and the signal at 1.3 ppm showed diminished relative intensity. This pronounced decrease in relative intensity was determined to correspond to a 99.9% removal of crude oil from water. The peak at 1.15 ppm is due to the solvent mixture (**Figure 2.11**). Other ^1H NMR signals are TMS that appears at 0 ppm and the area remains the same before and after filtration indicating the precision of the calibration.

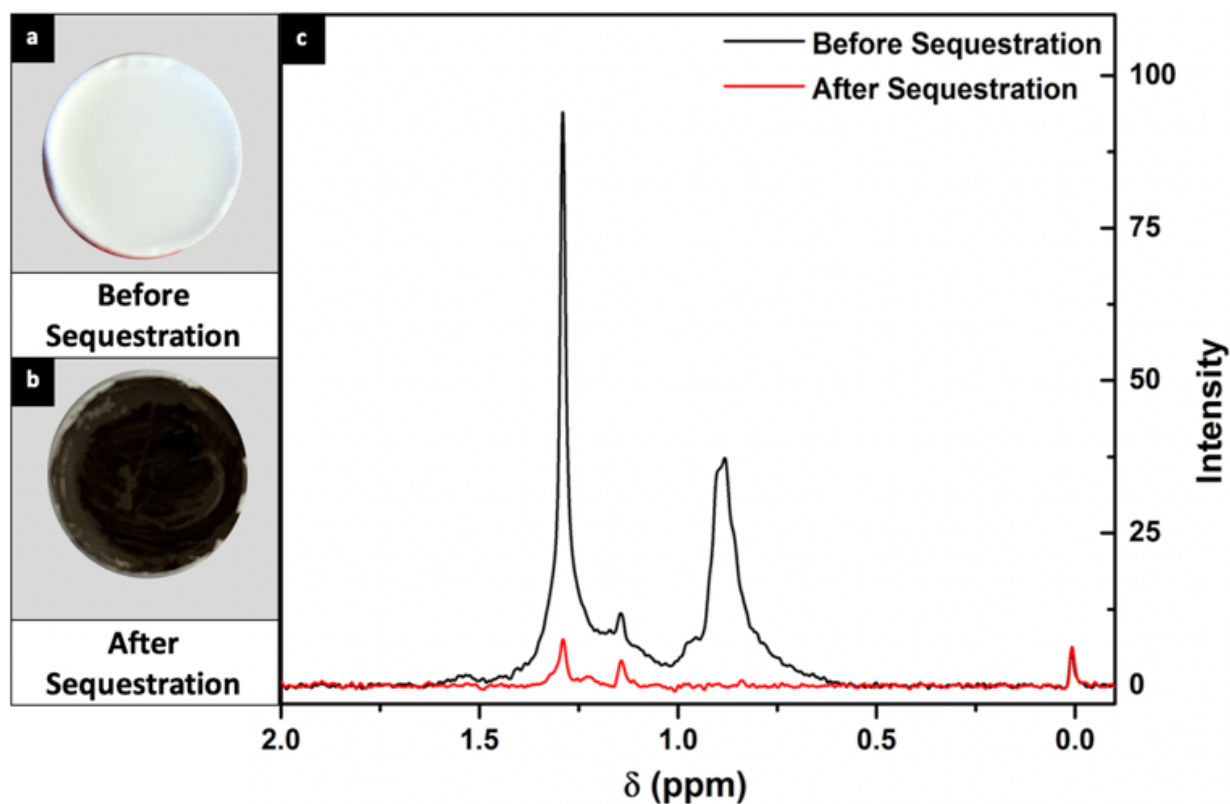


Figure 2.10 a) Top view of MHO ceramic before sequestration, b) top view of MHO ceramic after sequestration of crude oil-in-water emulsion in neutral pH, c) ^1H NMR spectrum of crude oil-in-water emulsion before and after sequestration with MHO ceramic.

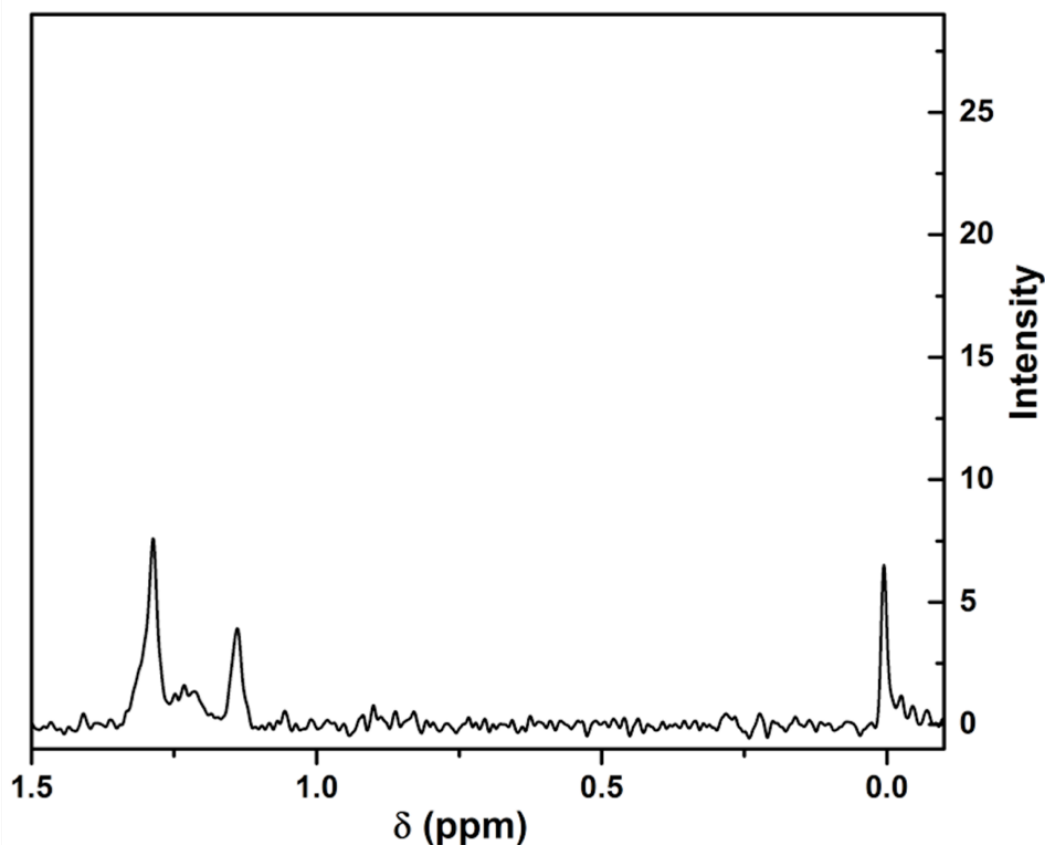


Figure 2.11 ^1H NMR spectrum of blank solution consisting of deuterated methanol, deuterated chloroform with tetramethylsilane (99.5% + 0.05%), and nanopure water.

Similar results were observed in extreme acidic (pH 1) and basic (pH 13) conditions using MHO ceramic and the commercial wine filter (as shown in **Figure 2.12– Figure 2.14**). Altering the pH can influence ionization of the contaminant molecule which can effect sequestration capacities.³⁹ However, changing the pH did not have an effect on crude oil sequestration because of the inert nature of crude oil. Crude oil is mainly composed of long hydrocarbon chains with strong C–C and C–H bonds which are stable in extreme pH. Furthermore, these alkanes do not have any hydrophilic or ionizable groups that can be influenced by change in pH.⁴⁰

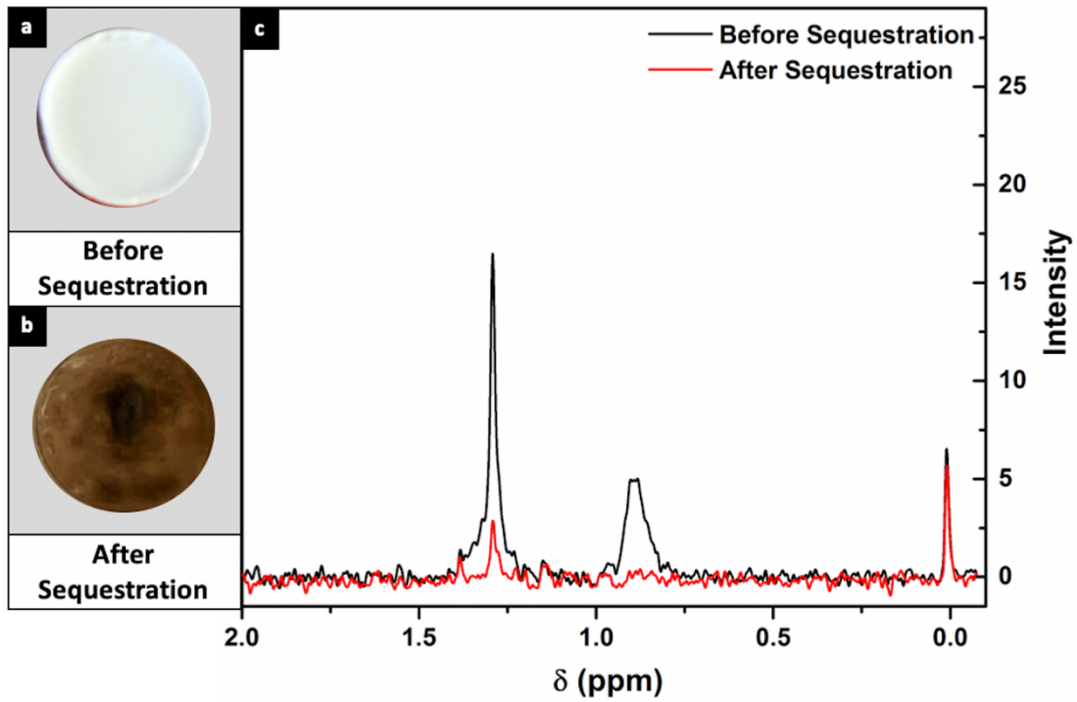


Figure 2.12 a) Top view of MHO ceramic before sequestration, b) Top view of MHO ceramic after sequestration of crude oil-water emulsion in acidic pH, c) ¹H NMR spectrum of liquid before and after sequestration with MHO ceramic.

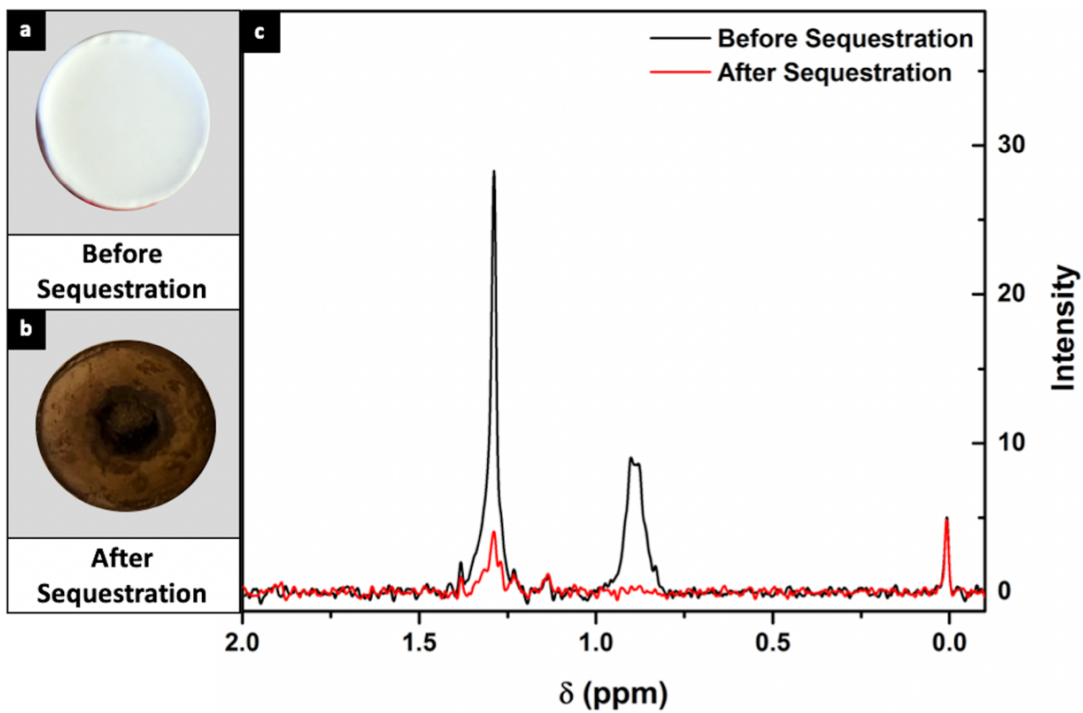


Figure 2.13 a) Top view of MHO ceramic before sequestration, b) Top view of MHO ceramic after sequestration of crude oil-water emulsion in basic pH, c) ¹H NMR spectrum of liquid before and after sequestration with MHO ceramic.

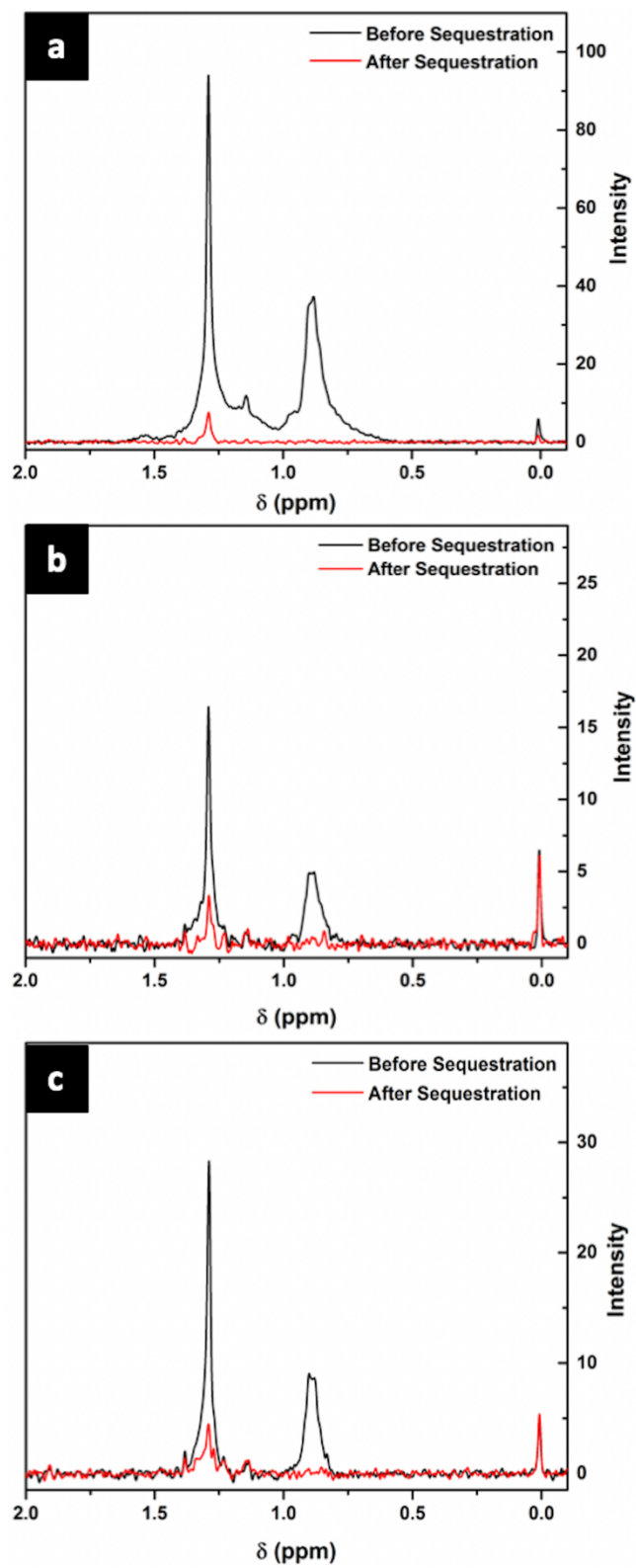


Figure 2.14 ¹H NMR spectrum of liquid before and after sequestration with commercial wine filter in a) Neutral pH, b) Acidic pH, c) Basic pH.

Table 2.1 offers a comparison between MHO ceramic and the cellulose wine filter, another ceramic membrane made of TiO₂,⁴¹ carbon nanotube based material,⁴² magnesium hydroxide formed *in situ*,⁴³ and a polyurethane sponge modified with hydrophobic silica nanoparticles.¹⁶ MHO and the cellulose wine filter have similar removal percentages, although the MHO ceramic is a more promising option as it can be readily regenerated by calcination.

Table 2.1 Comparison of MHO Ceramic with Various Oil Sorbent Materials

Material	% Removal	Emulsified?	Renewable?	Reference no.
Polyurethane sponge modified with hydrophobic silica nanoparticles	92	no	no	16
TiO ₂ membrane	99.56	yes	no	41
Multiwalled carbon nanotube	85	yes	yes	42
In situ formed magnesium hydroxide	99	yes	yes	43
Wine filter	99.9	yes	no	This work
Mesoporous Hafnium Oxide Ceramic	99.9	yes	yes	This work

Regeneration of MHO Ceramic

The reusability of materials used to clean oil spills is imperative, as it decreases the amount of waste produced during the clean-up and enhances the effectiveness of the material deployed. Other materials such as silica-based ceramics⁴⁴ and twisted carbon fiber aerogels⁴⁵ have been successfully regenerated to remove organic contaminants from water by calcination. This is relatively safer than using harsh and toxic chemicals to clean the material, as it does not produce excess toxic liquid waste. To compare the thermal stability and regeneration of MHO ceramic with the commercial wine filter we performed TGA experiments after filtration with the crude oil-in-water emulsion. Both the MHO ceramic and the wine filter were exposed to 800 °C under high purity argon flow. The results of the TGA are shown in **Figure 2.15** for MHO ceramic and **Figure 2.16** for the wine filter. The mass loss observed from heating the bare MHO ceramic before sequestration is 0.3% which is due to the evaporation of water from the hydrophilic surface. After

sequestration of the crude oil-in-water emulsion we see a mass loss of 1.3% which corresponds to the crude oil and some water evaporating from the MHO ceramic. In contrast, the mass loss observed from heating the bare wine filter before sequestration is 46.1% which is due to the degradation of the wine filter. After sequestration of the crude oil-in-water emulsion a mass loss of 48.7% is the result of the wine filter burning as it is not stable under high temperatures. After these experiments, we observed that the MHO ceramic showed its characteristic white color, and the wine filter had turned entirely black.

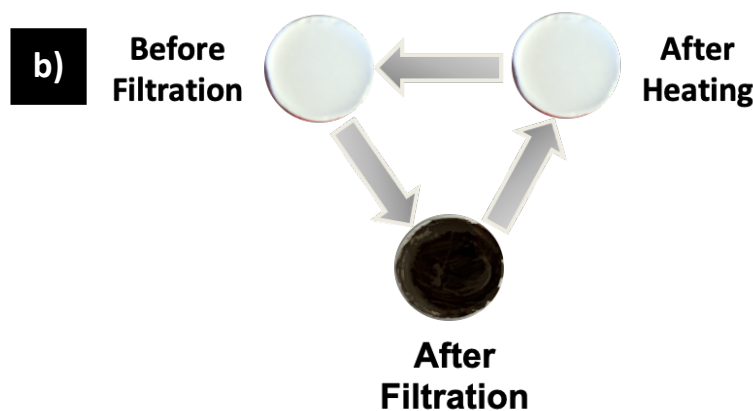
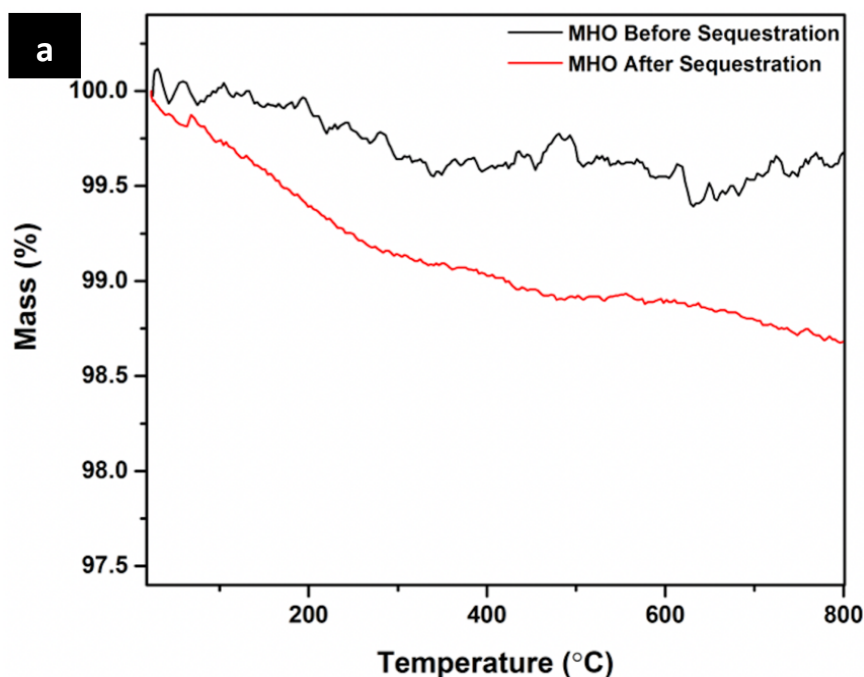


Figure 2.15 a) TGA of MHO ceramic before sequestration (black) and after crude oil sequestration (red) in neutral pH under argon, b) Illustrating the change in color of MHO before filtration, after filtration of crude oil-water emulsions, and after heating to remove crude oil.

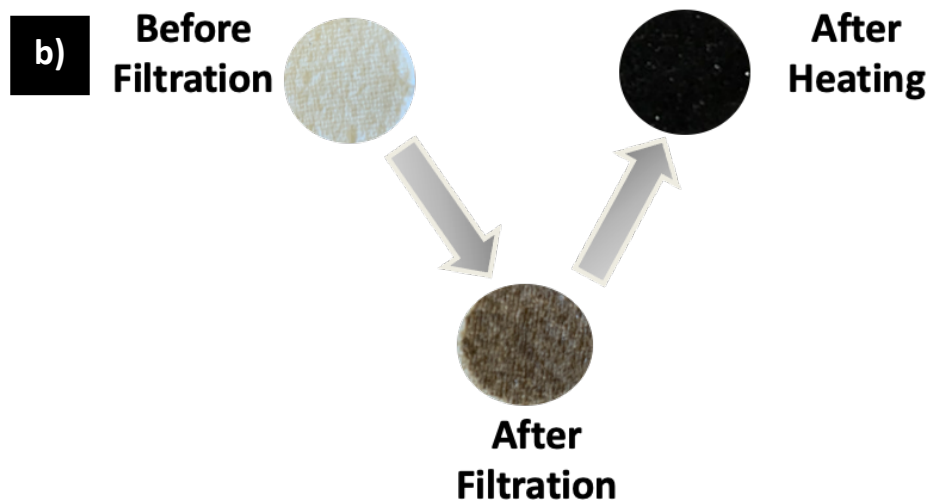
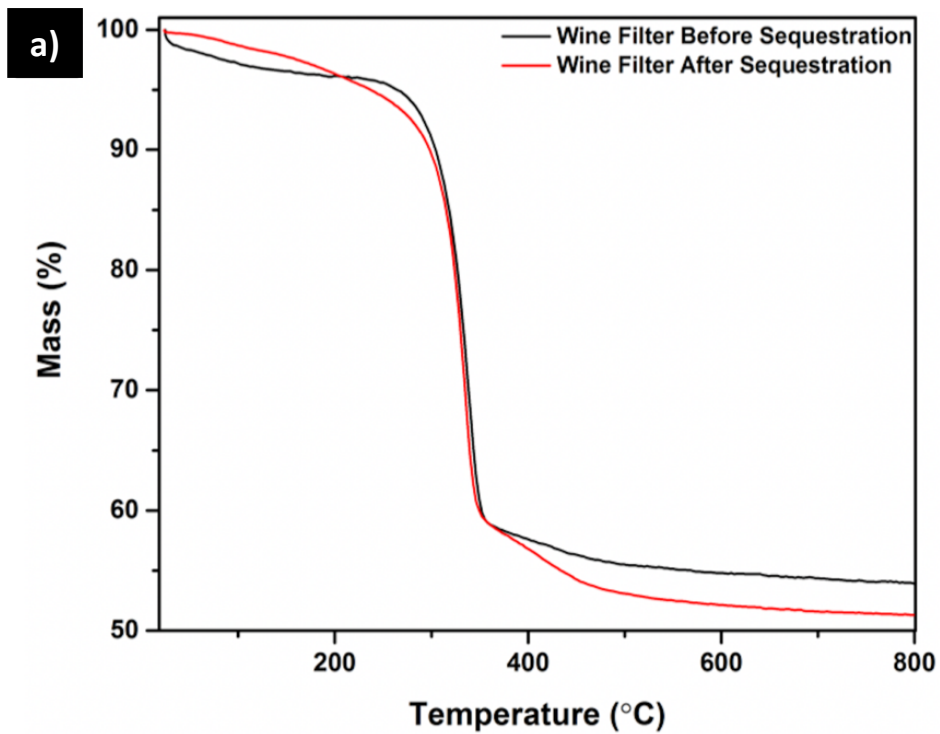


Figure 2.16 a) TGA of wine filter before sequestration (black) and after crude oil sequestration (red) in neutral pH under argon, b) Illustrating the change in color of wine filter before filtration, after filtration of crude oil-water emulsions, and after heating to remove crude oil.

To ensure that MHO ceramic could be regenerated after each filtration FTIR was done on the surface after calcination to confirm that oil was no longer present as shown in **Figure 2.17d**. The FTIR peaks present between 400-800 cm^{-1} represent the monoclinic hafnium oxide peaks of Hf-O and Hf-O₂. During the initial hydrolysis step of the sol-gel synthesis, N-methyl formamide undergoes hydrolysis in water to produce formic acid (HCOOH). As a result, the formate ligands from formic acid coordinate to the Hf ions. The low intensity peaks in the range of 1200-1600 cm^{-1} observed in the MHO ceramic before oil sequestration correspond to symmetric and antisymmetric formate (COO⁻) ligand vibrations on the surface of MHO. The three possible types of bonding of the formate ligand to the hafnium ions on the surface of MHO are shown in **Figure 2.17a-c**. **Figure 2.17a** illustrates a monodentate coordination of one oxygen atom from the formate ligand to one hafnium ion. **Figure 2.17b** is a chelating of two oxygen atoms to one hafnium ion. **Fig 5c** is an example of a bridging of two oxygen atoms to two hafnium ions.⁴⁶ The peak at 1300 cm^{-1} corresponds to monodentate coordination of carbonates as shown in in **Figure 2.17a**. The peak at 1600 cm^{-1} represents bidentate carbonates through either chelating of two oxygen atoms to one hafnium (**Figure 2.17b**) or bridging of two hafnium with two oxygen atoms (**Figure 2.17c**). The chelating bidentate and bridging bidentate convert to one another based on the degree of hydration on the surface. The peak at 2390 cm^{-1} is identified as CO₂. CO₂ interacts with the Lewis acid sites on the surface through σ -coordination from one of the lone pairs on oxygen.⁴⁷ The spectrum from the sample after filtration has the Hf-O and Hf-O₂ peaks from the monoclinic hafnium oxide. The peaks that are present in the sample after sequestration that are not present after calcination are the peaks at 1350 cm^{-1} and 1450 cm^{-1} which correspond to the C-H deformation vibration and the peaks at 2800 cm^{-1} and 2900 cm^{-1} which correspond to the C-H stretching vibration all in aliphatic hydrocarbon chains.⁴⁸ A detailed FTIR spectrum of pure crude oil is depicted in **Figure 2.18**. The spectrum after calcination does not show any of the sharp peaks that were present in the sample after crude oil sequestration. This further proves that there was no crude oil after calcination and MHO ceramic can be regenerated. Similar results were observed in acidic and basic pH as shown in **Figure 2.19** and **Figure 2.20**, respectively.

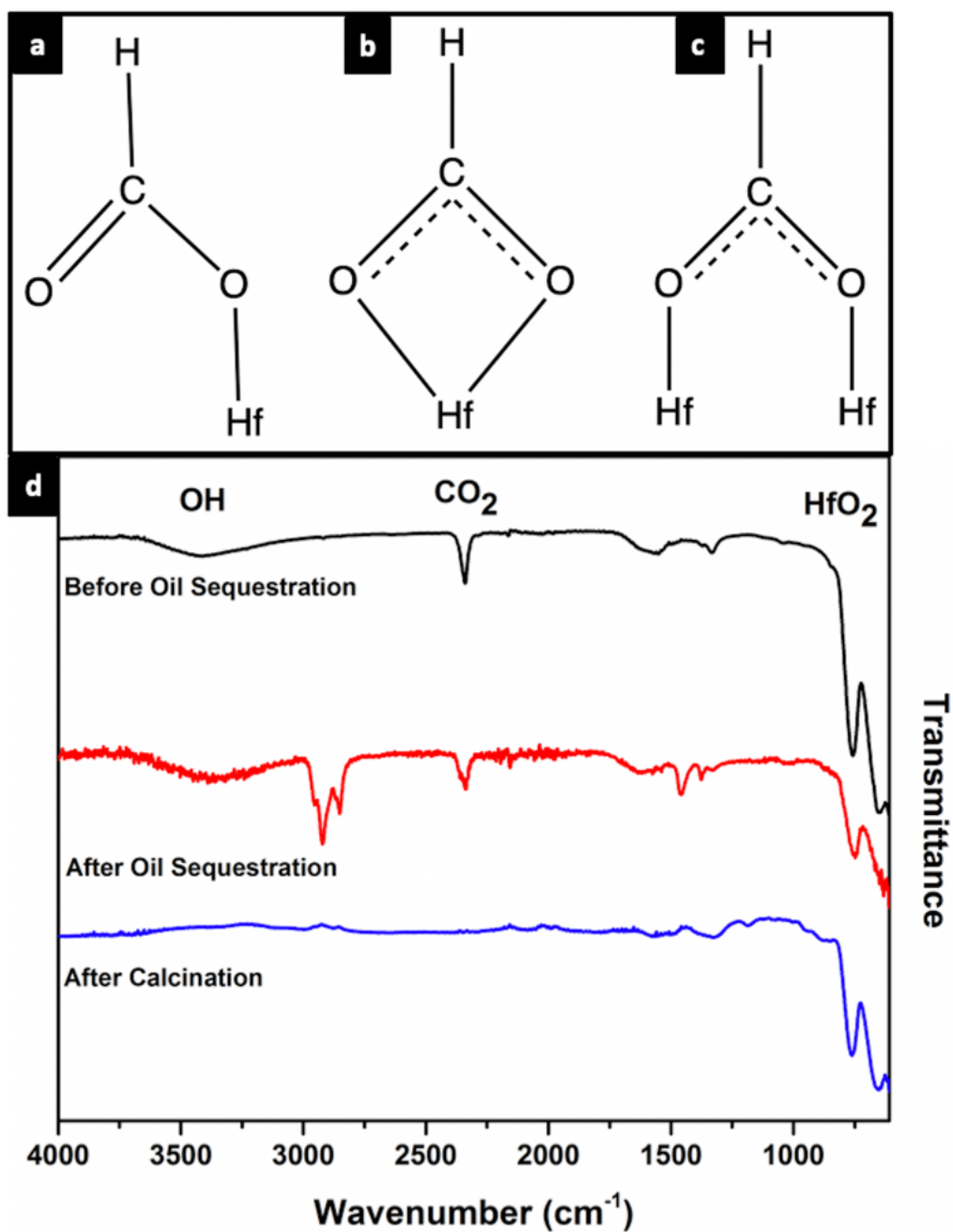


Figure 2.17 a) Monodentate coordination of one oxygen atom to one hafnium ion, b) Bidentate chelating of two oxygen atoms to one hafnium ion, c) Bidentate bridging of two oxygen atoms to two hafnium ions, and d) ATR-FTIR spectrum of MHO ceramic before sequestration, after sequestration in neutral pH, and after calcination.

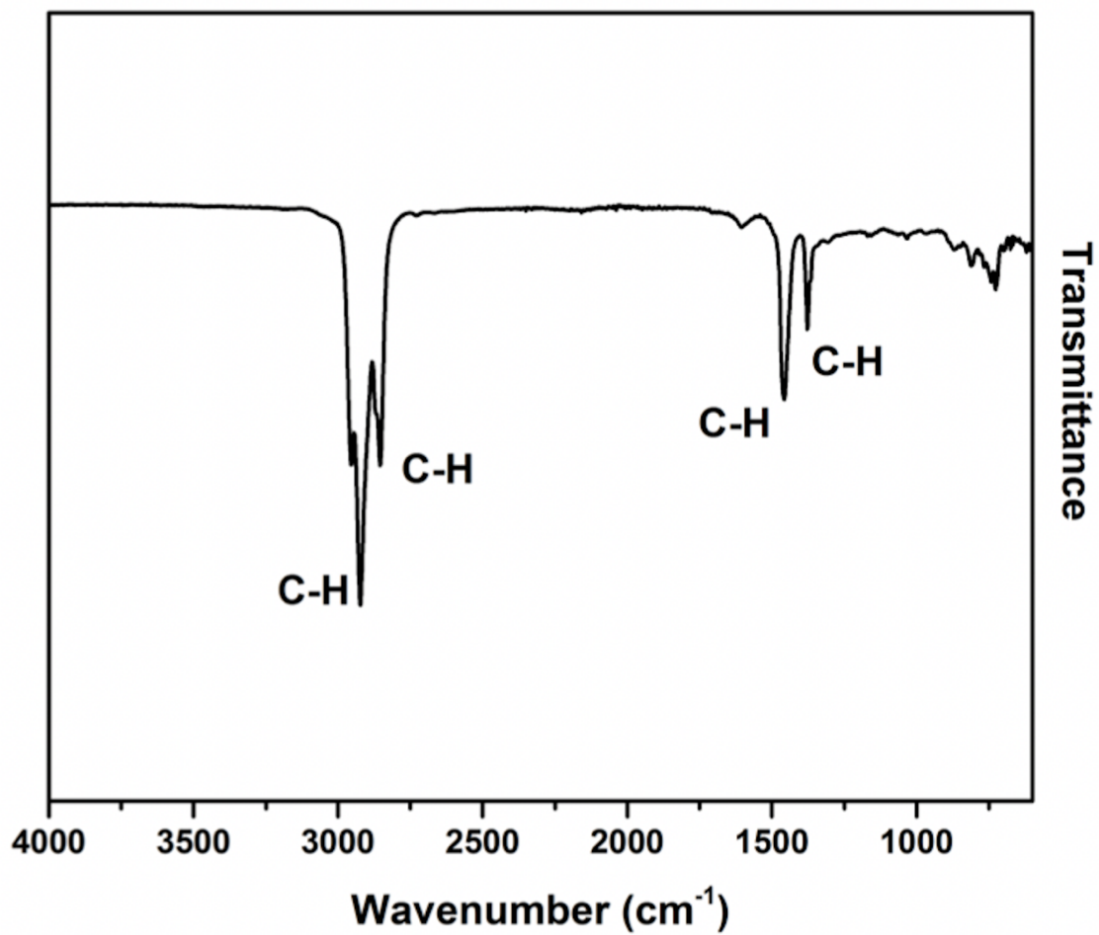


Figure 2.18 ATR-FTIR spectrum of crude oil with major peaks labelled.

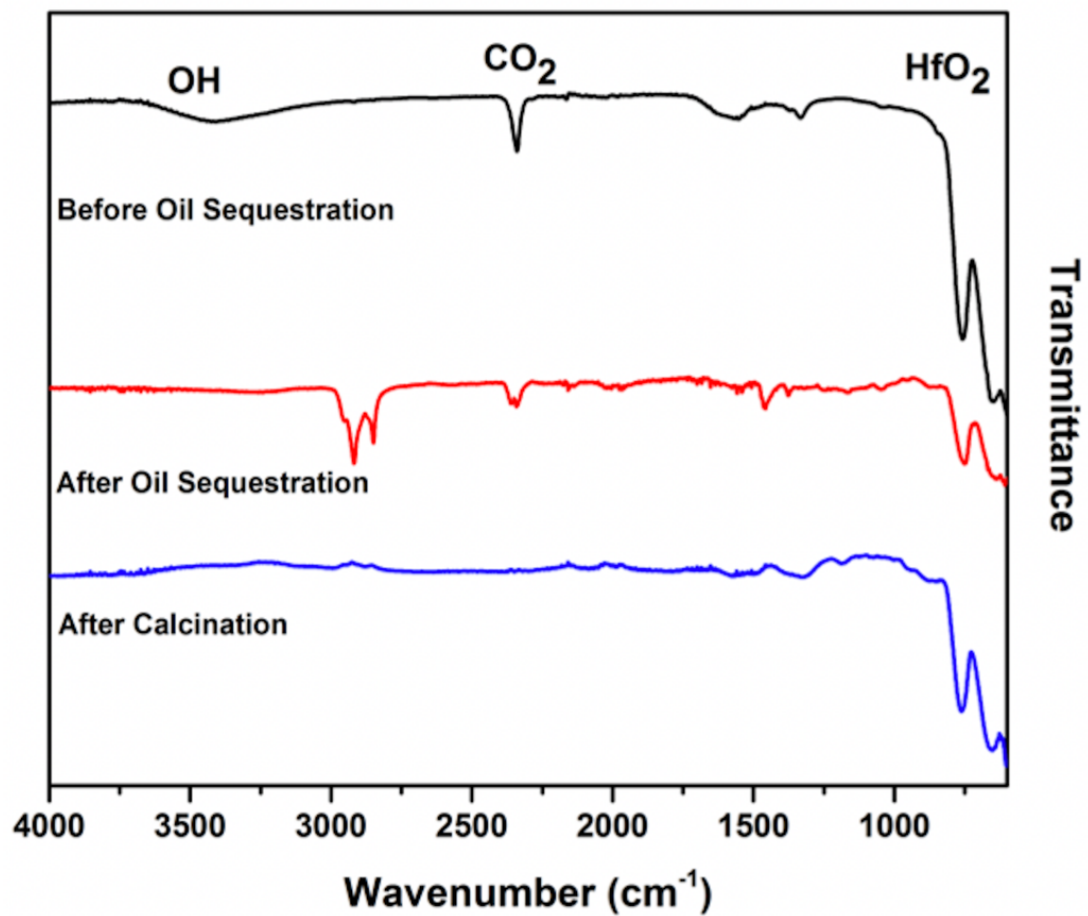


Figure 2.19 ATR-FTIR spectrum of MHO ceramic before sequestration, after sequestration in acidic pH, and after calcination.

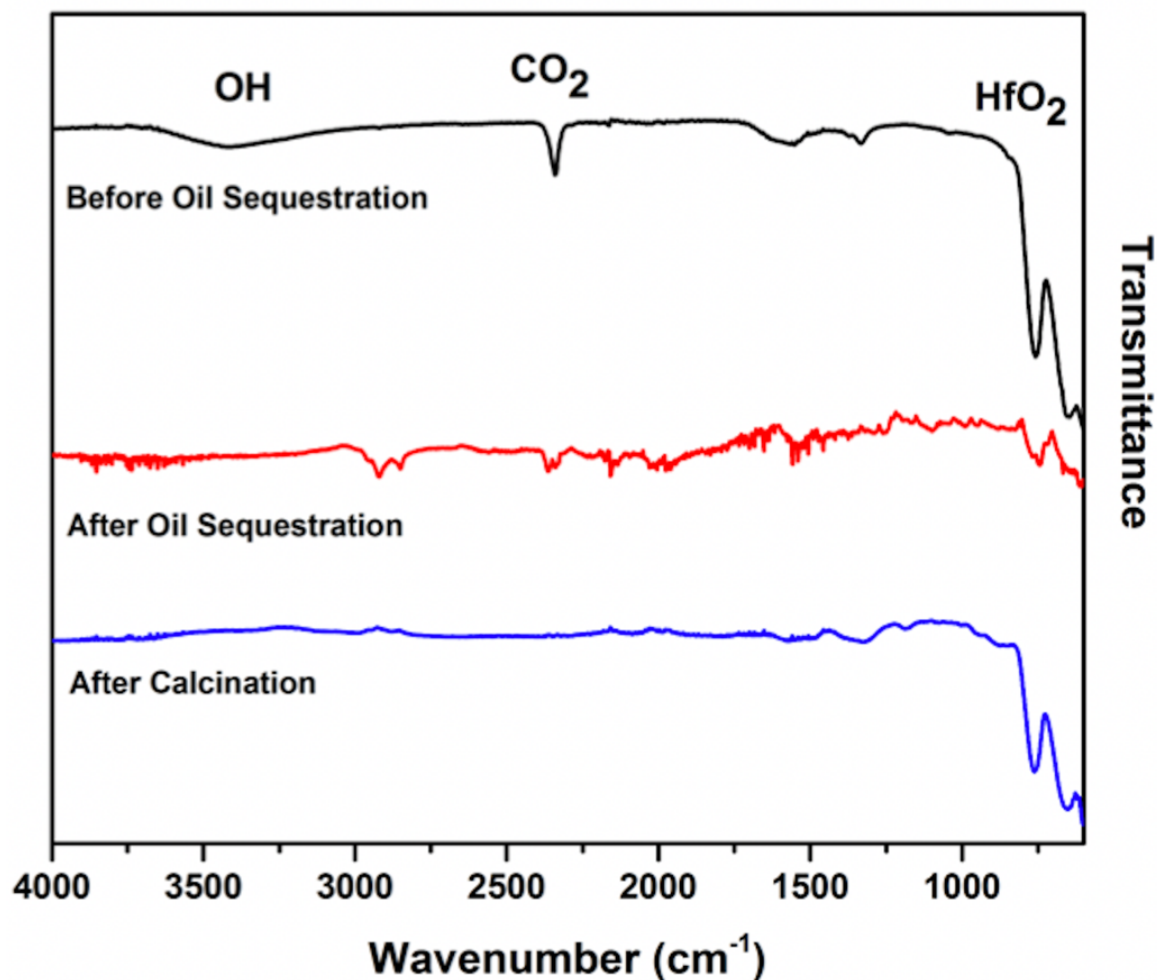


Figure 2.20 ATR-FTIR spectrum of MHO ceramic before sequestration, after sequestration in basic pH, and after calcination.

In this case, we believe that the governing aspect of adsorption during filtration is the adhesion of the hydrophobic crude oil to the hydrophilic MHO ceramic.⁴⁹ Since the solution at hand is an oil-in-water emulsion coalescence is necessary for de-emulsification of the mixture. During the coalescence process the smaller oil droplets attach on to the hydrophilic surface of the MHO ceramic followed by agglomeration of larger droplets. The physical force dominating the adhesion of the hydrophobic crude oil to the hydrophilic MHO ceramic is most likely Van der Waals (VdW) forces. VdW forces are weak intermolecular forces resulting from electrostatic interactions in typically non-attracting molecules due to asymmetric electronic distributions. Small electronic dipoles are created which can induce dipoles in complementary surfaces. Larger molecules have a higher propensity of remaining in the adsorbed state and that is due to VdW forces.

The longer the chain the more electron clouds that can be distorted and can interact with the surface of MHO. VdW forces are weak physical forces which means that the process is reversible. Since no chemical bonds are formed, regeneration of the MHO ceramic can be achieved by calcination of the material after crude oil sequestration as demonstrated herein.⁵⁰

Conclusions

An environmentally benign, mechanically stable, and renewable MHO ceramic monolith was synthesized through a sol-gel process leading to a crystalline bimodal material with macropores and mesopores. The monolith showed excellent adsorption of crude oil from oil-in-water emulsions in acidic, neutral, and basic pH. The material was regenerated by calcination to remove crude oil from the surface. Regeneration of MHO ceramic surface after calcination demonstrates an underexplored family class of materials that are robust under extreme conditions.

Future work for this project will involve development of Langmuir and Freundlich isotherms. The Langmuir adsorption isotherm is used to describe adsorption of a monolayer of oil on a homogeneous surface of an adsorbent. Meanwhile, the Freundlich isotherm model is used to describe multilayer adsorption of oil on a heterogeneous adsorbent surface. When it comes to a complex mixture such as that of crude oil, using either the Langmuir or Freundlich isotherms is challenging.⁵¹ This is due to the fact that not all components of crude oil obey these isotherms as single solutes, hence in order to calculate the constants for each isotherm one would need to be able to calculate the adsorption coefficient of each solute prior to the isotherm application.

Acknowledgements

We would like to acknowledge the University of California, Davis for start-up funding for this project, as well as support from the Cottrell Scholar program supported by the Research Corporation for Science Advancement (RCSA Grant ID#26780). We also acknowledge funding support from the NSF through UC

Davis ChemEnergy REU program, grant #1560479. We also acknowledge support from the McNair Scholars program. We would also like to acknowledge Kasey Devlin from the Kauzlarich Lab at UC Davis for assistance with TGA experiments, and Julio Zamora for assistance with experiments & method development.

References

- 1 L. Pendleton, A. Comte, C. Langdon, J. A. Ekstrom, S. R. Cooley, L. Suatoni, M. W. Beck, L. M. Brander, L. Burke, J. E. Cinner, C. Doherty, P. E. T. Edwards, D. Gledhill, L.-Q. Jiang, R. J. van Hooidek, L. Teh, G. G. Waldbusser and J. Ritter, Coral Reefs And People In A High-CO₂ World: Where Can Science Make A Difference To People?, *PLoS One*, 2016, **11**, e0164699.
- 2 G. Troisi, S. Barton and S. Bexton, Impacts Of Oil Spills On Seabirds: Unsustainable Impacts Of Non-Renewable Energy, *Int. J. Hydrogen Energy*, 2016, **41**, 16549–16555.
- 3 M. I. Ramirez, A. P. Arevalo, S. Sotomayor and N. Bailon-Moscoso, Contamination By Oil Crude Extraction – Refinement And Their Effects On Human Health, *Environ. Pollut.*, 2017, **231**, 415–425.
- 4 U. S. C. Guard, *On scene coordinator report : Deepwater Horizon oil spill.*, Library of Congress, 2011.
- 5 S. Sun, Y. Lu, Y. Liu, M. Wang and C. Hu, Tracking An Oil Tanker Collision And Spilled Oils In The East China Sea Using Multisensor Day And Night Satellite Imagery, *Geophys. Res. Lett.*, , DOI:10.1002/2018GL077433.
- 6 P. Venkataraman, J. Tang, E. Frenkel, G. L. McPherson, J. He, S. R. Raghavan, V. Kolesnichenko, A. Bose and V. T. John, Attachment Of A Hydrophobically Modified Biopolymer At The Oil–Water Interface In The Treatment Of Oil Spills, *ACS Appl. Mater. Interfaces*, 2013, **5**, 3572–3580.

- 7 V. John, C. Arnosti, J. Field, E. Kujawinski and A. MacCormick, The Role Of Dispersants In Oil Spill Remediation: Fundamental Concepts, Rationale For Use, Fate, And Transport Issues, *Oceanography*, 2016, **29**, 108–117.
- 8 S. Kleindienst, J. H. Paul and S. B. Joye, Using Dispersants After Oil Spills: Impacts On The Composition And Activity Of Microbial Communities, *Nat. Rev. Microbiol.*, 2015, **13**, 388.
- 9 H. K. White, S. L. Lyons, S. J. Harrison, D. M. Findley, Y. Liu and E. B. Kujawinski, Long-Term Persistence Of Dispersants Following The Deepwater Horizon Oil Spill, *Environ. Sci. Technol. Lett.*, 2014, **1**, 295–299.
- 10 B. S. Echols, C. J. Langdon, W. A. Stubblefield, G. M. Rand and P. R. Gardinali, A Comparative Assessment Of The Aquatic Toxicity Of Corexit 9500 To Marine Organisms, *Arch. Environ. Contam. Toxicol.*, 2019, **77**, 40–50.
- 11 J. Beirão, L. Baillon, M. A. Litt, V. S. Langlois and C. F. Purchase, Impact Of Crude Oil And The Dispersant CorexitTM EC9500A On Capelin (*Mallotus Villosus*) Embryo Development, *Mar. Environ. Res.*, 2019, **147**, 90–100.
- 12 G. Alaa El-Din, A. A. Amer, G. Malsh and M. Hussein, Study On The Use Of Banana Peels For Oil Spill Removal, *Alexandria Eng. J.*, 2018, **57**, 2061–2068.
- 13 O. Abdelwahab, S. M. Nasr and W. M. Thabet, Palm Fibers And Modified Palm Fibers Adsorbents For Different Oils, *Alexandria Eng. J.*, 2017, **56**, 749–755.
- 14 Z. Wang, J. Saleem, J. P. Barford and G. McKay, Preparation And Characterization Of Modified Rice Husks By Biological Delignification And Acetylation For Oil Spill Cleanup, *Environ. Technol.*, 2018, **39**, 1–12.
- 15 M. Khosravi and S. Azizian, Synthesis Of A Novel Highly Oleophilic And Highly Hydrophobic Sponge For Rapid Oil Spill Cleanup, *ACS Appl. Mater. Interfaces*, 2015, **7**, 25326–25333.

- 16 A. Atta, M. Abdullah, H. Al-Lohedan and N. Mohamed, Novel Superhydrophobic Sand And Polyurethane Sponge Coated With Silica/Modified Asphaltene Nanoparticles For Rapid Oil Spill Cleanup, *Nanomaterials*, 2019, **9**, 187.
- 17 Z.-R. Jiang, J. Ge, Y.-X. Zhou, Z. U. Wang, D. Chen, S.-H. Yu and H.-L. Jiang, Coating Sponge With A Hydrophobic Porous Coordination Polymer Containing A Low-Energy CF₃-Decorated Surface For Continuous Pumping Recovery Of An Oil Spill From Water, *NPG Asia Mater.*, 2016, **8**, e253–e253.
- 18 E. Barry, A. U. Mane, J. A. Libera, J. W. Elam and S. B. Darling, Advanced Oil Sorbents Using Sequential Infiltration Synthesis, *J. Mater. Chem. A*, 2017, **5**, 2929–2935.
- 19 S. T. Nguyen, J. Feng, N. T. Le, N. Hoang, V. B. C. Tan and H. M. Dong, Cellulose Aerogel From Paper Waste For Crude Oil Spill Cleaning, *Ind. Eng. Chem. Res.*, , DOI:10.1021/ie4032567.
- 20 H.-P. Cong, X.-C. Ren, P. Wang and S.-H. Yu, Macroscopic Multifunctional Graphene-Based Hydrogels And Aerogels By A Metal Ion Induced Self-Assembly Process, *ACS Nano*, 2012, **6**, 2693–2703.
- 21 P. Gao, Z. Liu, D. D. Sun and W. J. Ng, The Efficient Separation Of Surfactant-Stabilized Oil–Water Emulsions With A Flexible And Superhydrophilic Graphene–TiO₂ Composite Membrane, *J. Mater. Chem. A*, 2014, **2**, 14082–14088.
- 22 L. Zhang, Y. Zhong, D. Cha and P. Wang, A Self-Cleaning Underwater Superoleophobic Mesh For Oil-Water Separation., *Sci. Rep.*, 2013, **3**, 2326.
- 23 J. Song, S. Huang, Y. Lu, X. Bu, J. E. Mates, A. Ghosh, R. Ganguly, C. J. Carmalt, I. P. Parkin, W. Xu and C. M. Megaridis, Self-Driven One-Step Oil Removal From Oil Spill On Water Via Selective-Wettability Steel Mesh, *ACS Appl. Mater. Interfaces*, 2014, **6**, 19858–19865.

- 24 X. Zhou, F. Wang, Y. Ji, W. Chen and J. Wei, Fabrication Of Hydrophilic And Hydrophobic Sites On Polypropylene Nonwoven For Oil Spill Cleanup: Two Dilemmas Affecting Oil Sorption, *Environ. Sci. Technol.*, 2016, **50**, 3860–3865.
- 25 S. Govender and H. B. Friedrich, Monoliths : A Review Of The Basics , Preparation Methods And Their Relevance To Oxidation, *Catalysts*.
- 26 A. Cybulski and J. A. Moulijn, Monoliths In Heterogeneous Catalysis, *Catal. Rev.*, 1994, **36**, 179–270.
- 27 V. Tomašić and F. Jović, State-Of-The-Art In The Monolithic Catalysts/Reactors, *Appl. Catal. A Gen.*, 2006, **311**, 112–121.
- 28 D. Lu, T. Zhang and J. Ma, Ceramic Membrane Fouling During Ultrafiltration Of Oil/Water Emulsions: Roles Played By Stabilization Surfactants Of Oil Droplets, *Environ. Sci. Technol.*, 2015, **49**, 4235–4244.
- 29 J. Nawrocki, M. Rigney, A. McCormick and P. Carr, Chemistry Of Zirconia And Its Use In Chromatography, *J. Chromatogr. A*, 1993, **657**, 229–282.
- 30 I. M. Ferrer-Lassala, SUNY Buffalo, 2013.
- 31 S. Palchoudhury and J. R. Lead, A Facile And Cost-Effective Method For Separation Of Oil – Water Mixtures Using Polymer-Coated Iron Oxide Nanoparticles, *Environ. Sci. Technol.*, 2014, **48**, 14558–14563.
- 32 W. J. Robson, P. A. Sutton, P. McCormack, N. P. Chilcott and S. J. Rowland, Class Type Separation Of The Polar And Apolar Components Of Petroleum, *Anal. Chem.*, 2017, 2919–2927.
- 33 S. Palchoudhury and J. R. Lead, A Facile And Cost-Effective Method For Separation Of Oil– Water Mixtures Using Polymer-Coated Iron Oxide Nanoparticles, *Environ. Sci. Technol.*, 2014, **48**, 14558–14563.

- 34 R. Almeda, Z. Wambaugh, C. Chai, Z. Wang, Z. Liu and E. J. Buskey, Effects Of Crude Oil Exposure On Bioaccumulation Of Polycyclic Aromatic Hydrocarbons And Survival Of Adult And Larval Stages Of Gelatinous Zooplankton, *PLoS One*, 2013, **8**, e74476–e74476.
- 35 R. H. Carmichael, A. L. Jones, H. K. Patterson, W. C. Walton, A. Pérez-Huerta, E. B. Overton, M. Dailey and K. L. Willett, Assimilation Of Oil-Derived Elements By Oysters Due To The Deepwater Horizon Oil Spill, *Environ. Sci. Technol.*, 2012, **46**, 12787–12795.
- 36 J. Vilcáez, L. Li and S. S. Hubbard, A New Model For The Biodegradation Kinetics Of Oil Droplets: Application To The Deepwater Horizon Oil Spill In The Gulf Of Mexico, *Geochem. Trans.*, 2013, **14**, 4.
- 37 L. Díaz-Ballote, N. U. García-Cruz, E. Hernández-Nuñez, A. Castillo-Atoche, G. González-García and G. Rodríguez-Gattorno, *Quim. Nova*, 2018, **41**, 969–973.
- 38 I. Rakhmatullin, S. Efimov, M. Varfolomeev and V. Klochkov, High-Resolution NMR Study Of Light And Heavy Crude Oils: “Structure-Property” Analysis, *IOP Conf. Ser. Earth Environ. Sci.*, 2018, **155**, 012014.
- 39 R. C. Pereira, P. R. Anizelli, E. Di Mauro, D. F. Valezi, A. C. S. da Costa, C. T. B. V. Zaia and D. A. M. Zaia, The Effect Of pH And Ionic Strength On The Adsorption Of Glyphosate Onto Ferrihydrite, *Geochem. Trans.*, 2019, **20**, 3.
- 40 B. Simonovic, D. Arandjelovic, M. Jovanovic, B. Kovacevic, L. Pezo and A. Jovanovic, Removal Of Mineral Oil And Wastewater Pollutants Using Hard Coal, *Chem. Ind. Chem. Eng. Q.*, 2009, **15**, 57–62.
- 41 K. Suresh and G. Pugazhenthii, Cross Flow Microfiltration Of Oil-Water Emulsions Using Clay Based Ceramic Membrane Support And TiO₂ Composite Membrane, *Egypt. J. Pet.*, 2017, **26**, 679–694.

- 42 T. H. Ibrahim, M. A. Sabri and M. I. Khamis, Application Of Multiwalled Carbon Nanotubes And Its Magnetite Derivative For Emulsified Oil Removal From Produced Water, *Environ. Technol.*, 2019, **40**, 3337–3350.
- 43 W. Dong, D. Sun, Y. Li and T. Wu, Rapid Removal And Recovery Of Emulsified Oil From ASP Produced Water Using In Situ Formed Magnesium Hydroxide, *Environ. Sci. Water Res. Technol.*, 2018, **4**, 539–548.
- 44 G. M. K. Tolba, A. M. Bastaweesy, E. A. Ashour, W. Abdelmoez, K. A. Khalil and N. A. M. Barakat, Effective And Highly Recyclable Ceramic Membrane Based On Amorphous Nanosilica For Dye Removal From The Aqueous Solutions, *Arab. J. Chem.*, 2016, **9**, 287–296.
- 45 H. Bi, Z. Yin, X. Cao, X. Xie, C. Tan, X. Huang, B. Chen, F. Chen, Q. Yang, X. Bu, X. Lu, L. Sun and H. Zhang, Carbon Fiber Aerogel Made From Raw Cotton: A Novel, Efficient And Recyclable Sorbent For Oils And Organic Solvents, *Adv. Mater.*, 2013, **25**, 5916–5921.
- 46 T. Nishide, T. Meguro, S. Suzuki and T. Yabe, Ultraviolet Irradiation Hardening Of Hafnia Films Prepared By Sol-Gel Processes, *J. Ceram. Soc. Japan*, 2005, **113**, 77–81.
- 47 C. Morterra, G. Cerrato, V. Bolis and B. Fubini, A Characterization Of The Surface Acidity Of HfO₂ by FTIR Spectroscopy Of Adsorbed Species, Electron Microscopy And Adsorption Microcalorimetry, *Spectrochim. Acta Part A Mol. Spectrosc.*, 1993, **49**, 1269–1288.
- 48 A. Samanta, K. Ojha and A. Mandal, Interactions Between Acidic Crude Oil And Alkali And Their Effects On Enhanced Oil Recovery, *Energy & Fuels*, 2011, **25**, 1642–1649.
- 49 S. Bansal, V. von Arnim, T. Stegmaier and H. Planck, Effect Of Fibrous Filter Properties On The Oil-In-Water-Emulsion Separation And Filtration Performance, *J. Hazard. Mater.*, 2011, **190**, 45–50.
- 50 S. De Gisi, G. Lofrano, M. Grassi and M. Notarnicola, Characteristics And Adsorption Capacities Of Low-Cost Sorbents For Wastewater Treatment: A Review, *Sustain. Mater. Technol.*, 2016, **9**, 10–40.

51 R. Wahid, L. A. Chuah, T. S. Y. Choong, Z. Ngaini and M. M. Nourouzi, Oil Removal From Aqueous State By Natural Fibrous Sorbent: An Overview, *Sep. Purif. Technol.*, 2013, **113**, 51–63.

3 Chapter 3: Understanding Fate of Per- and Polyfluoroalkyl Substances (PFAS) During Composting of Food Service Products

Abstract

Per- and polyfluoroalkyl substances (PFAS) are a large group of synthetic chemicals that are used in compostable food service products (FSP) due to their hydrophobic and lipophobic properties. However, during composting of these FSP the PFAS can leach into the soil or water and contaminate food and drinking water sources. Bench-scale and commercial-scale composting experiments were setup to determine degradation of FSP and evaluate the fate of PFAS on these FSP during the process. FSP containing PFAS did not degrade completely in the bench and commercial-scale composting process due to the persistence of these molecules and the presence of carbon-fluorine bonds. Mesoporous hafnium oxide (MHO) was synthesized and used to filter PFAS from water. The MHO had higher percent removal efficiencies for longer chain, more hydrophobic PFAS due to the increased hydrophobic effect between hydrophobic molecules and the hydrophilic surface of MHO.

Introduction

Per- and polyfluorinated alkyl substances (PFAS) are a large group of over 4000 synthetic industrial chemicals which have been found in the environment from groundwater, to soil, and even the ocean.¹ These molecules are synthesized for a variety of applications from fire-fighting foams, to everyday products like water-proof clothing, non-stick pans, household carpets, and compostable food-service packaging (FSP).² PFAS are used to coat surfaces of FSP as these molecules are lipophobic and hydrophobic.³ These FSP contain high concentrations of PFAS which could enter the human body through transfer to food, increasing dietary exposure.⁴ PFAS can also contaminate the soil as compostable FSP degrade PFAS into the soil which then contaminate the crops, the livestock that consume the crops, and the meat and milk of the

livestock that is consumed by humans.⁵ One of the most common PFAS found in drinking water as well as FSP is perfluorooctanoic acid (PFOA).⁶ Studies show that exposure to PFOA can lead to various health issues such as testicular and kidney cancer, increased cholesterol levels, thyroid problems, and decreased fertility in adults.⁷ PFOA has also been seen to have adverse effects on child development and immune response in infants who were exposed to PFAS by breast milk especially during the first six months.⁸

Composting is an established and currently used method to dispose of food and compostable waste. Since FSP have shown to contain PFAS in the range of thousands of parts per million (ppm),⁹ composting was the initial method evaluated to assess degradation of PFAS. Composting is a biochemical process that converts organic waste in the presence of oxygen into carbon dioxide, heat, water, and a stable organic substance that can be recovered as a soil amendment or organic fertilizer.¹⁰ Composting involves organisms, such as worms and millipedes, breaking down the bulk of organic matter by mechanical means while microorganisms, such as bacteria and fungi, chemically convert the remaining organic matter to end products of carbon dioxide, heat, water, and compost.¹¹ While carbon dioxide is a product of this aerobic process, studies have shown that GHG emissions from food waste decomposition in landfills are significantly higher than GHG emissions from composting due to methane's greater global warming potential.¹² Since food waste can be highly variable depending on its source, it is important to study multiple parameters of the composting process to ensure an optimized system with a stable product.

Composting requires a moisture content that is between 45 to 60 percent by weight.¹³ A moisture content that is too low will inhibit microbial activity and decrease the biodegradation rates.¹⁴ Due to this moisture on average an industrial composting facility produces 4-400 m³ of leachate per day.^{15,16} PFAS containing FSP could leach during composting and dissolve in the leachate that would later contaminate groundwater and drinking water sources.¹⁷ Therefore adsorbents are also used at composting facilities to adsorb PFAS from leachate.^{18,19} Specifically, mesoporous hafnium oxide (MHO) ceramics as they are mechanically robust, non-toxic, and thermally stable.²⁰ These mesoporous ceramics also have a bimodal pore structure

with larger macropores (> 50 nm) that allow flux of clean water, and smaller mesopores (2-50 nm) that entrap PFAS.²¹

The purpose of this work was to evaluate the degradation of FSP that contain toxic PFAS by evaluating the effect of different moisture contents during bench-scale composting, and by using two different inoculums during commercial-scale composting. The solid compost samples and FSP samples were analyzed using LC-MS and PIGE respectively. To address PFAS from solid FSP that leach during composting, the next goal was to determine the ability of adsorbents such as MHO and metal-organic frameworks (MOFs) to filter out toxic PFAS from water.

Materials & Methods

Chemicals: Hafnium(IV) tetrachloride (98%) was used as the Hafnium source. Acetone, hexanes, methanol, and pentane were all HPLC Plus (>99.9%). Hydrochloric acid (35.0–37.0%), Perfluorotridecanoic acid (97%), Magnesium nitrate hexahydrate (99.999%), N,N-Dimethylformamide (DMF, >99.8%), and deuterated water (D₂O) were used as purchased from Sigma-Aldrich. Pure anhydrous ethanol was purchased from Koptec. The 2,5-dihydroxy-terephthalic acid (H4DOBDC, 98%) was purchased from Spectrum chemical. *N*-Methyl formamide (99%), sodium hydroxide pellets (98%), Nickel (II) nitrate hexahydrate (98%), perfluorodecanoic acid (97%), perfluorododecanoic acid (96%), and perfluorotetradecanoic acid (96%) were purchased from Alfa Aesar. Poly(ethylene oxide) (MW 100 000) was purchased from Polysciences Inc. Propylene oxide (99.5%) and Trifluoroacetic acid (99.5%) were purchased from Acros Organics. Perfluoropentanoic acid (>98%) and Perfluorooctanoic acid (>98%) were purchased from TCI America. Perfluorobutanoic acid (99%) was purchased from Frontier Science. Perfluoroheptanoic acid (98%) was purchased from Matrix Scientific. Perfluorohexanoic acid (97%), perfluorononanoic acid (98%), and perfluoroundecanoic acid (96%) were all purchased from Oakwood Chemical. The fresh cow manure was obtained from the UC Davis Dairy Teaching and Research Facility. Ultrapure water (≥ 18.2 M Ω ·cm) used for synthesis and adsorption kinetics experiments was obtained from

a Thermo Scientific Barnstead E-Pure Ultrapure water purification system. Whatman grade 5 cellulose filter paper with a pore size 2.5 μm was purchased from Sigma-Aldrich. The FSP used in these experiments were all advertised as compostable by the vendors. The FSP used were no.6 coffee filters that are unbleached and made from chlorine-free paper (if you care brand) that were used as a positive control, low density polyethylene sheets (Uline brand) used as a negative control, fiber plates made from bamboo and unbleached plant fibers and green bioplastic bags made from starch were purchased from World Centric, clear clamshells made from polylactic acid (PLA) from corn and white clamshells made from sugarcane bagasse and lined with PLA were purchased from Eco Products.

Part I. Evaluating Fate of PFAS from FSP During Bench-Scale and Commercial-Scale Composting

Bench-Scale Composting Setup

The bench-scale experiments were set up in the Wastewater Laboratory of Dr. Maureen Kinyua in the Department of Civil and Environmental Engineering at the University of California, Davis. **Figure 3.1** provides a schematic of the reactors. Each reactor was built with cast acrylic non-reactive tubing with an inner diameter of 7.5 inches and a height of 11 inches. Two ports were added at the bottom of the reactor for the inlet of air and leachate sampling. Similarly, one port was fitted at the top of the reactor for the air outlet for condensation. Aeration was provided through the perforated (opening diameter of 0.25 inches) plate that was placed in the lower bottom part (3.5 inches from bottom) of the reactor. Reactors were operated at 45% moisture content, and at 60% moisture content. The duration of the experiment was 24 days, and sampling of the compost and FSP was performed on day 0, 3, 5, 7, 10, 14, 18, 20, and 24. The percent degradation of FSP was calculated using **eq. 3.1**:

$$\% \text{ Degradation of FSP} = \frac{m_0 - m}{m_0} \times 100 \text{ (eq. 3.1)}$$

Where m_0 is the initial mass of FSP in grams before composting and m is the mass of FSP after 24 days of composting.

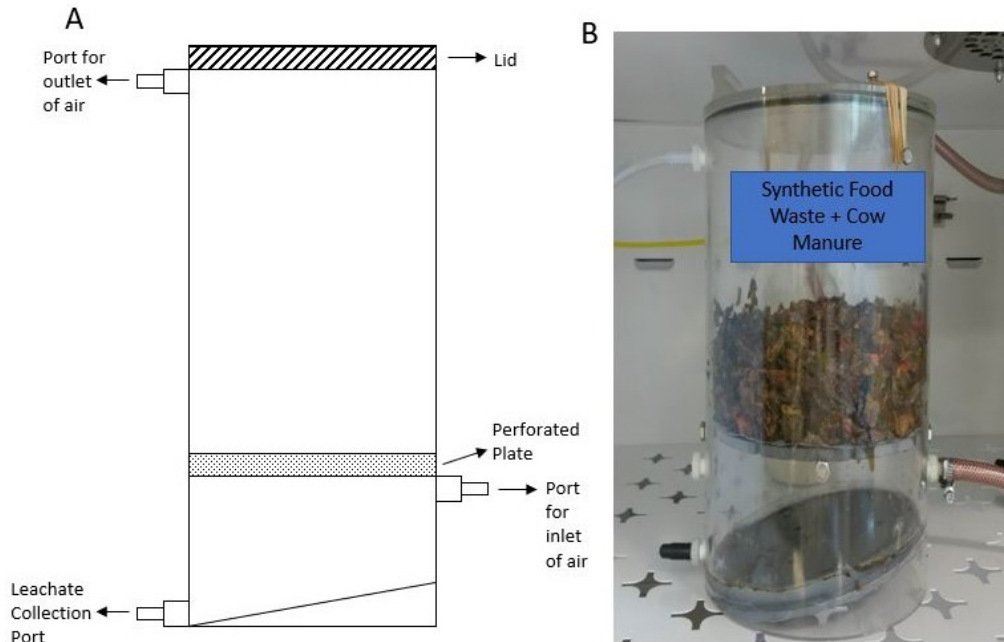


Figure 3.1 Illustration of A) schematic of the reactor, and B) reactor with synthetic food waste and cow manure.

The reactors were placed in an incubator at a constant temperature of 56.0 °C, and constant airflow of 0.3 liters of air per minute, supplied through an air pump. Each reactor contained different types of FSP; see **Table 3.1** for more details. All the FSP were cut in a uniform size of 2 x 2 cm. Cut FSP were sealed in mesh-like plastic bags to avoid the loss in the reactor. Synthetic food waste was created using the mixture of tomatoes, carrots, and lettuce at a ratio of 1:1:1 by weight. Dried leaves and wood chips were added in a ratio of 1:2 by weight to be used as bulking agents. Finally, 175 grams of cow manure (inoculum) was added to 400 mL of Mili Q water, and the slurry of Mili Q water and inoculum was added to reactors. Cow manure was chosen as the inoculum for bench-scale composting experiments as preliminary experiments showed that cow manure had the highest specific oxygen uptake rate when compared to inoculums such as aged compost, mixed liquor, and landfill sludge. Specific oxygen uptake rate is directly related to microbial activity and biodegradation.

Table 3.1 Details of Reactors in Bench-Scale Experimental Setup

Reactor Name	Moisture Content by Weight (%)	Types of Food Service Packaging (FSP) Added
R _{Positive_45}	45	Unbleached Coffee Filters
R _{Positive_60}	60	Unbleached Coffee Filters
R _{Negative_45}	45	LDPE Sheets
R _{Negative_60}	60	LDPE Sheets
R ₄₅ (triplicates)	45	Fiber plates + Bioplastic Bags + PLA Lined Bagasse Clamshells
R ₆₀ (triplicates)	45	Fiber plate + Bioplastic Bags + PLA Lined Bagasse Clamshells

Commercial-Scale Composting Setup

Three aerated static compost piles were set at the Napa Recycling and Waste Services in American Canyon, California. For the aerated static composting process, organic waste was mixed in a large pile, and the piles were placed over the network of pipes that deliver air into the piles as shown in **Figure 3.2**. To aerate the piles, layers of loosely piled bulking agents like garden trimmings and wood waste were added to the piles so that the air could pass from bottom to top. Air blowers were used to blow the air from the bottom to the top through the perforated openings in the floor. All air blowers were active throughout the process. Three trials were conducted at the facility from October 2020 to April 2021. Each trial consisted of two different piles constructed on-site using only food waste and old compost as inoculums. Each pile (94 feet (L) x 30 feet (W) x 10 feet (H)) consisted of inoculum, feedstock (grass, food scraps, and dry leaves), and bulking agents (garden trimmings and wood waste). Piles were constructed from bottom to top, and the top layer was covered with a biofilter layer. The biolayer was a simple top covering layer of soil that protects the piles from heat loss and helps to reduce the escape of foul odors. Each pile had 5 temperature sensors engineered by Engineered Compost Services for continuous monitoring of temperature. Water was sprinkled using sprinklers over the piles 4–6 times a day (from 7 am to 7 pm) depending on the temperature

of the pile. The piles were constantly aerated at a rate of 4.5 cubic feet per minute. Six types of FSP samples were placed in the different mesh-like plastic bags, and the bags were placed in the piles for 24 days. Compost and samples of each type of FSP were collected from the piles on days 3, 5, 7, 10, 14, 18, 20, and 24. The percent degradation of FSP in this case was determined using eq. 3.1.

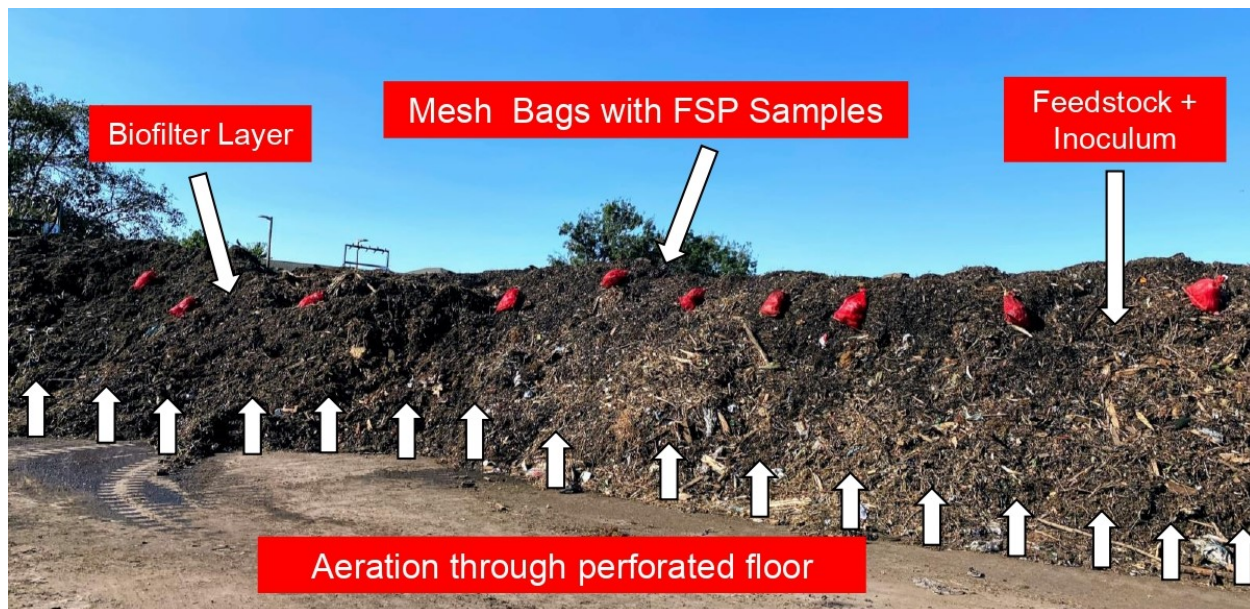


Figure 3.2 Aerated composting pile at Napa Recycling Facility with biofilter layer, mesh bags with FSP samples, and feedstock + inoculum.

Compost Extraction Method

PFAS are extracted from the solid compost samples from the bench-scale composting experiments and commercial-scale composting experiments using previously established extraction procedures.²² Two extractions were done on five grams of solid waste in a 50 mL centrifuge tube to ensure efficiency. In the first extraction, 13 mL of acidified methanol was added to the solid waste and vortexed for 30 seconds and sonicated for one hour in warm water. Then the tube was placed in a shaker for 30 minutes, followed by 5 minutes in a centrifuge at 6000 rpm. The supernatant liquid was extracted and placed in a separate clean tube. The second extraction was done with 10 mL of acidified methanol and the rest of the steps were

repeated the same as detailed above. Both supernatants were combined and dried in a rotary evaporator and reconstituted with 2 mL of methanol. 200 μ L of this matrix was placed in an NMR tube with 400 μ L of D₂O (deuterated water) spiked with an internal standard of trifluoroacetic acid (TFA) for analysis in ¹⁹F NMR.

Analyzing Solids for PFAS Content

For Particle-Induced gamma ray emission (PIGE) spectroscopy the plastic samples were trimmed to fit in 1mm by 1mm plastic bags; for samples where the plastic was broken into pieces, the bags were filled such that the thickness approximated that of the intact samples. Each bag was manually adhered with masking tape to separate stainless steel target frames with a hole of 1 cm in diameter. The portion of the sample exposed through the target's hole was irradiated with ~60 nA of 4 MeV protons for 180 seconds. PIGE spectroscopy exploits the isotope-specific wavelengths of the electromagnetic radiation emitted in the nuclear (p,p' γ) reactions. Fluorine content is calculated by numerically integrating the 110 and 197 keV gamma-ray peaks; because fluorine is mono-isotopic, these signals are indicative of all elemental fluorine present in the samples. PIGE is a comparative measurement; levels of detected fluorine vary daily with the intensity, energy, and tune of the beam. Therefore, each set of samples is preceded with a set of standards treated with stock solutions of sodium fluorine in cellulose. The number of counts detected at these characteristic wavelengths is proportional to fluorine content on the sample's surface. A linear regression applied to the graph of standards' measured fluorine counts vs. known ppm concentration is used to accurately convert measured fluorine counts to ppm fluorine content in the samples.²³ Because bombardment of the samples occurs ex-vacuo, beam intensity and angular resolution can be influenced by discharged ions in the atmosphere. Because of its natural abundance in the atmosphere and lack of interference with fluorine peaks, argon is employed as a normalizing element. Measurements of atmospheric argon's 770 keV gamma-ray peak provide insight into how beam fluctuations and transmission to target bias fluorine counts across samples.²⁴ Solid PFAS samples were analyzed using Attenuated Total Reflectance Fourier transform Infrared (FTIR) Spectroscopy to observe the bonds in the PFAS molecules.

A 5-10 mg aliquot of sample was placed on the sample holder of a Bruker tensor 27 FTIR and scans were performed from 600-4000 cm^{-1} .

Analyzing Liquids for PFAS Content

To detect PFAS in water, standards for each PFAS studied (C4-C14) were created by dissolving standards in water at a concentration of 1000 parts per million (ppm) for analysis using Nuclear Magnetic Resonance (NMR) spectroscopy. 200 μL of this matrix was placed in an NMR tube with 400 μL of D_2O (deuterated water) spiked with an internal standard of trifluoroacetic acid (TFA) for calibration. A 400 MHz NMR instrument was used for these measurements, and each sample was analyzed with 128 scans. Liquid samples were also analyzed using liquid chromatography coupled with mass spectrometry (LC-MS). An Agilent Infinity II 1260 Quad Pump was used with a G6125B single quad mass spectrometer in negative ionization mode. The column used was Zorbax SB-C3 (5 μm pore size) 4.6 mm x 250 mm. The liquid samples were diluted in Acetonitrile with 0.1% formic acid in a 50:50 ratio.

Part II. Synthesis & Characterization of Adsorbents to Filter PFAS from Water

MHO Synthesis

Mesoporous hafnium oxide (MHO) ceramic monoliths were synthesized using the sol-gel method.²⁵ Glass vials were treated with 0.1 M sodium hydroxide for one hour, 0.1 M hydrochloric acid for one hour, and Rain-x overnight. After removing the Rain-x, vials were rinsed with methanol and dried in an oven. Hafnium (IV) chloride was dissolved in ultrapure water (resistivity $>18.2 \text{ M}\Omega$). Then *N*-Methylformamide (NMF) was added, to increase the pH of the solution, and induce phase separation. Polyethylene oxide was added to strengthen the pore network. In addition, propylene oxide was added to induce polymerization, turning the clear liquid to a white gel. The gel was then aged at 50 $^{\circ}\text{C}$ for three days. The monolith was washed with ultrapure water, methanol, acetone, hexanes, and pentane to remove any excess reagents, and

to prevent cracks during heating. Finally, the sample underwent heat treatment in a furnace in air to 700 °C, which yields a crystalline white monolithic ceramic.

M-MOF-74 Synthesis (M= Mg, Ni)

The M-MOF-74 were synthesized using a modified procedure.²⁶ For Ni-MOF-74 nickel nitrate hexahydrate was used as the metal precursor and 2,5-dihydroxyterephthalic acid was used as the ligand (H4DOBDC). In a 250 mL glass bottle, 0.602 g of NiNO₃.6H₂O and 0.12 g of H4DOBDC were dissolved in 45 mL of DMF, 3 mL of ethanol, and 3 mL of ultrapure water. The bottle was placed in an oven at 110°C for 48 hours. After cooling the sample was centrifuged at 3000 rpm for 5 minutes to separate the solid product from the liquid. The mother liquor was decanted and the solid was washed in sequence with DMF once and then methanol twice. Finally the solid was dried in a vacuum oven at 180C for 12 hours. For MG-MOF-74 magnesium nitrate hexahydrate was used as the metal precursor (0.712 g) and H4DOBDC was used as the ligand (0.167 g). A similar synthesis process was used as described for Ni-MOF-74 except Mg-MOF-74 was heated at 125°C for 26 hours.

Characterization

After the synthesis, the crystalline structure of the adsorbents were determined by powder X-ray diffraction (XRD) using a Bruker D8 Advance diffractometer with Cu K α radiation (1.5406 Å). Experimentally obtained diffraction patterns were then compared to literature patterns from the Inorganic Crystal Structure Database to confirm the structure. The pore structure of the materials were determined by a Thermofisher Quattro Environmental scanning electron microscope. The sample was placed on double-sided copper tape and operated at an accelerating voltage of 10 keV under low vacuum. The surface functional groups of the adsorbents were analyzed using Fourier transform infrared (FTIR) spectroscopy. The Bruker Tensor 27 FTIR was equipped with an attenuated total reflectance (ATR) pike accessory. The experiment was performed using 32 scans, a resolution of 2 cm⁻¹, and a spectral range of 400–4000 cm⁻¹. The surface area

was measured by Brunauer-Emmet-Teller (BET) method with nitrogen adsorption using a Micromeritics Gemini VII surface area analyzer.

Filtration Method for PFAS

For this objective, a vacuum filtration experiment was set up as shown in **Figure 3.3b** below. For each filtration a monolith of mesoporous hafnium oxide (MHO) of 0.2 grams was attached to the stem of the funnel using a halogen free shrinking tube (**Figure 3.3a**). The PFAS that were used were perfluorobutanoic acid (PFBA), perfluorohexanoic acid (PFHxA), and perfluorooctanoic acid (PFOA). The PFAS concentration was analysed before and after filtration using ^{19}F NMR spectroscopy. For filtration using MOF powders a dispersion was created by sonicating 60 mg of MOF in 30 mL of methanol for 30 minutes (Branson 8800, 40 kHz, ambient conditions). The emulsion was then dropped on a grade 1 cellulose filter paper in a vacuum filtration setup. The filter paper was allowed to dry for 10 minutes before using for PFAS filtration.

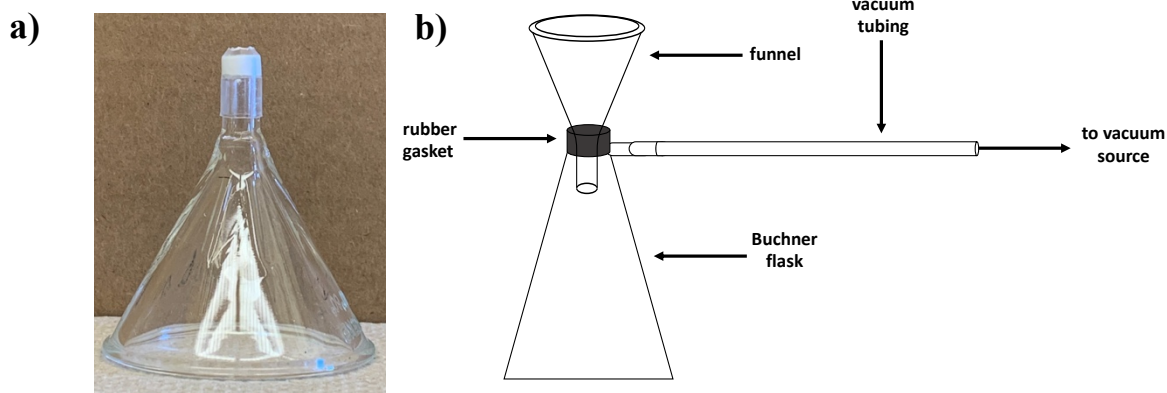


Figure 3.3 a) Funnel with MHO ceramic attached using shrinking tube, b) vacuum filtration setup for PFAS removal.

The PFAS concentration in the liquid before and after filtration was quantitatively determined using ^{19}F NMR spectroscopy. The percentage of PFAS adsorbed after filtration is calculated using **eq. 3.2**:

$$\% \text{ PFAS Adsorbed} = \frac{(C_0 - C)}{C_0} \times 100\% \quad (\text{eq. 3.2})$$

Where C_0 is the initial concentration of PFAS in ppm before filtration, and C is the concentration of PFAS after filtration in ppm.

The quantity of PFAS adsorbed after filtration is calculated using **eq. 3.3**:

$$q_t = \frac{(C_0 - C) \times V}{m} \quad (\text{eq. 3.3})$$

Where q_t is the quantity of PFOA adsorbed in mg per gram of MHO, C_0 is the initial concentration of PFOA in ppm, C is the concentration of PFOA after filtration, V is the total volume of solution used in the experiment in mL, and m is mass of the MHO adsorbent in grams. All experiments were performed in triplicates and the error bars have been included in the figures to report one standard deviation.

Results & Discussion

Part I. Evaluating Fate of PFAS During FSP Composting

PFAS Evaluated

Table 3.2 below summarizes 11 different PFAS molecules that were detected using methods developed by ^{19}F NMR spectroscopy and LC-MS in liquid samples and FTIR in solid samples. All PFAS standards could be detected in the FTIR; however, since the ^{19}F NMR required samples to be dissolved in a liquid solvent for detection, Perfluorotridecanoic acid (C13) and Perfluorotetradecanoic acid (C14) could not be detected in water. This is because as the chain length increases, the molecule becomes more hydrophobic, therefore the solubility in water decreases.²⁷ Since LC-MS has a lower detection limit, it could detect all 11 PFAS in the liquid state. If samples are not soluble in water, they can be dissolved in other solvents, but this study was concerned with detecting PFAS in leachate, which is mostly water.

Table 3.2 Summary of PFAS Detected Through FTIR, ¹⁹F NMR, LC-MS

PFAS Name	Molecular Weight (g/mol)	Solubility in Water (g/L)	Detected in FTIR? (Y/N)	Detected in ¹⁹ F NMR? (Y/N)	Detected in LC-MS? (Y/N)
Perfluorobutanoic acid (C4)	214.04	214	Y	Y	Y
Perfluoropentanoic acid (C5)	254.05	112.6	Y	Y	Y
Perfluorohexanoic acid (C6)	314.05	21.7	Y	Y	Y
Perfluoroheptanoic acid (C7)	364.06	4.2	Y	Y	Y
Perfluorooctanoic acid (C8)	414.07	3.4-9.5	Y	Y	Y
Perfluorononanoic acid (C9)	464.08	9.5	Y	Y	Y
Perfluorodecanoic acid (C10)	514.09	9.5	Y	Y	Y
Perfluoroundecanoic acid (C11)	564.09	0.004	Y	Y	Y
Perfluorododecanoic acid (C12)	614.1	0.0007	Y	Y	Y
Perfluorotridecanoic acid (C13)	664.1	0.0002	Y	N	Y
Perfluorotetradecanoic acid (C14)	714.1	0.00003	Y	N	Y

Results from Bench-Scale Composting

The change in mass of each of the FSP tested during bench-scale composting are shown in **Figure 3.4**. Overall it is clear that at 60% moisture the degradation of FSP was much higher than at 45% moisture content. Moisture content affects the rate of biopolymer degradation by impacting both microbial growth rate and hydrolysis.²⁸ Microbial activity increases with when moisture content increases, thus promoting biodegradation of polymers.²⁹ As mentioned previously, synthetic hetero-chain biopolymers undergo hydrolysis in environments with moisture.³⁰ Hydrolysis reduces the molecular weight of biopolymers, making them susceptible to microbial enzymatic activity.³¹ For example, studies evaluated the impact of moisture on the degradation of polylactic acid (PLA) films found significant molecular weight reduction as

the relative humidity increased from 10 to 100% at 55°C.³² Very high moisture content may result in waterlogs resulting in anaerobic conditions. Similarly, very low moisture content can cause early dehydration, hindering the biological process.³³ The negative control which was LDPE sheets did not degrade as expected since LDPE is not biodegradable. The clear PLA clamshells degraded into microplastics (0.5-5mm) that could not be retrieved from the compost pile so the degradation percentage could not be determined. The green waste bags had a degraded to 57.73% which is comparable to that of the positive control (coffee filter) at 61.89% at 60% moisture content. The fiber plates had a lower degradation rate of 37.46% at 60% moisture content due to their increased thickness in comparison to the coffee filter and green waste bags and the fact that they contained PFAS.

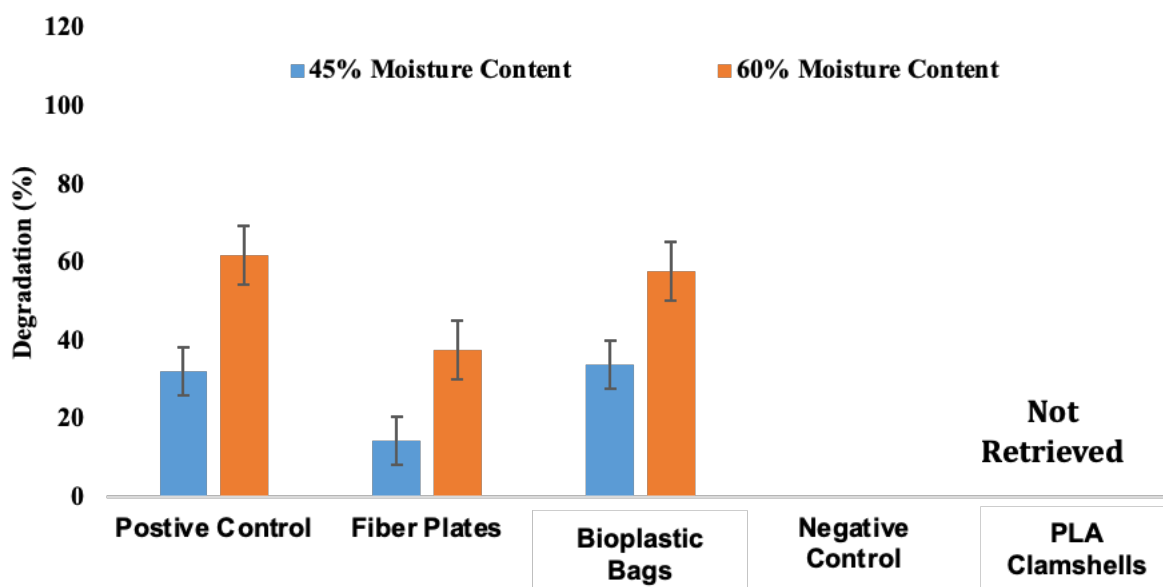


Figure 3.4 Average percent degradation of five different FSP tested during bench-scale composting using cow manure at 45% moisture content (blue) and 60% moisture content (orange).

The change in PFAS concentration on the FSP during the 24 day composting period was determined by PIGE spectroscopy. The errors in PIGE measurements arose from background subtracted peak integrations (2-4%) and the uncertainty in the integrated beam current measurement (6-10%). Propagating these two uncertainties results in an overall 6-11% instrumental uncertainty for fluorine concentrations.²³ Based on **Figure 3.5**, of all the FSP tested using bench-scale composting only the fiber plate contained PFAS. The initial fluorine concentration on the fiber plate was 883 ± 52 ppm. Over the 24 day composting period the

concentration of fluorine on the fiber plate increased to 1094 ± 329 ppm at 45% moisture content and 1098 ± 135 ppm at 60% moisture content. The mass loss observed, 14.47% at 45% moisture content and 37.46% at 60% moisture content, could be due to the degradation of the bamboo and unbleached plant fibers to CO_2 , water, and biomass. However, since the PFAS are not degrading, the total amount of fluorine per cm^2 of the FSP product is increasing. This increase in fluorine concentration could be due to the fact that PFAS are extremely stable due to the strength of the carbon-fluorine bond, however the functional head groups of the molecule may undergo transformation in these composting environments. The transformation of PFAS head groups during composting does not result in PFAS degradation but rather conversion from one PFAS to another.³⁴ For instance, some studies have shown that paper FSP products contain fluorotelomer alcohols (FTOH), during composting FTOH can be converted to perfluoroalkyl acid (PFAAs) which are extremely persistent.³⁵ The solid compost extracts were also analyzed at each time interval, however no fluorine was detected in ^{19}F NMR or in the LC-MS.

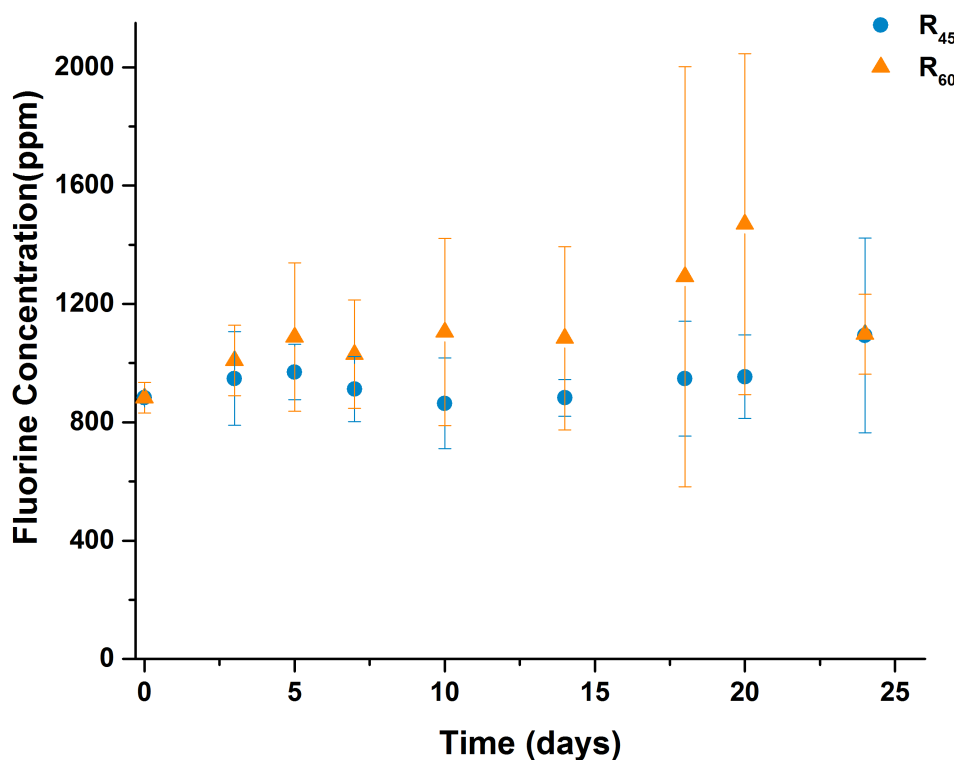



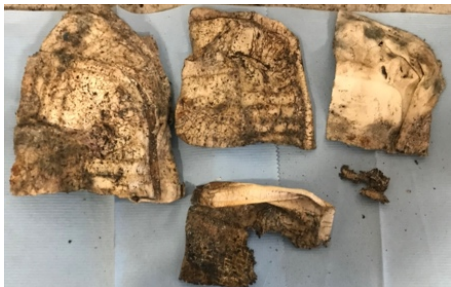
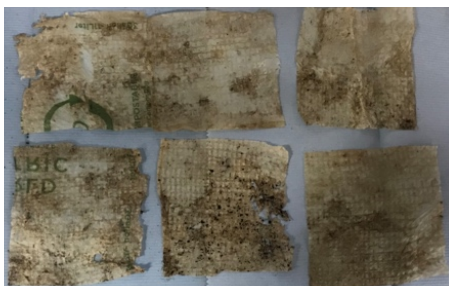





Figure 3.5 Change in fluorine concentration on the fiber plate over 24 days of bench-scale composting using cow manure at 45% moisture content (blue) and 60% moisture content (orange).

Results from Commercial-Scale Composting

The change in mass of each of the FSP tested during commercial-scale composting are shown in **Figure 3.6**. Overall, bioplastic bags had the highest average percent degradation of 94% in food waste and 92% in old compost. However, the PLA lined bagasse clamshell had a degradation of 17% in food waste and 7% in old compost, and the fiber plate had a degradation of 26% in food waste and 11% in old compost. Images illustrating the change in mass of FSP using food waste as an inoculum are shown in **Table 3.3**. Very minimal degradation is observed for the fiber plate and PLA lined bagasse (sugarcane fibers) clamshell after 3 days and after the entire 24 days of composting. In contrast, the thinner bioplastic bags is almost completely degraded after 24 days, and the PLA clamshell is broken into smaller fragments, but not degraded. The fiber plates contained PFAS, and are much thicker than the green waste bags. These differences may be attributed to the chemical structure, polymer chain, crystallinity, and or the complexity of the polymer formula as shown in prior studies.^{36,37} For example, the PLA lined Bagasse Clamshell container had the lowest average percent degradation. A prior study has demonstrated that the degradation process is easier for natural-based polymers than PLA lined.³⁸ The negative control (LDPE) sheets did not degrade as expected and the clear PLA clamshell degraded into microplastics but since the quantities were larger in the commercial-scale experiments the plastics could be retrieved by sieving to determine mass loss. Environmental and FSP based factors impact the degree of degradation. In a composting environment, biodegradation of the bioplastics depends on the biodiversity of microorganisms.³⁹ Hence even though the physical conditions like moisture content and temperature were similar, the difference in microbial ecology of the two composting piles may have affected degradation of the FSP.

Table 3.3 Degradation of FSPs at T-3 and T-24 Days Using Food Waste Inoculum During Commercial-Scale Composting

FSP Type	T – 3 days	T – 24 days
Fiber Plates		
PLA Lined Bagasse Clamshells		
Bioplastic Bags		
PLA Clamshells		

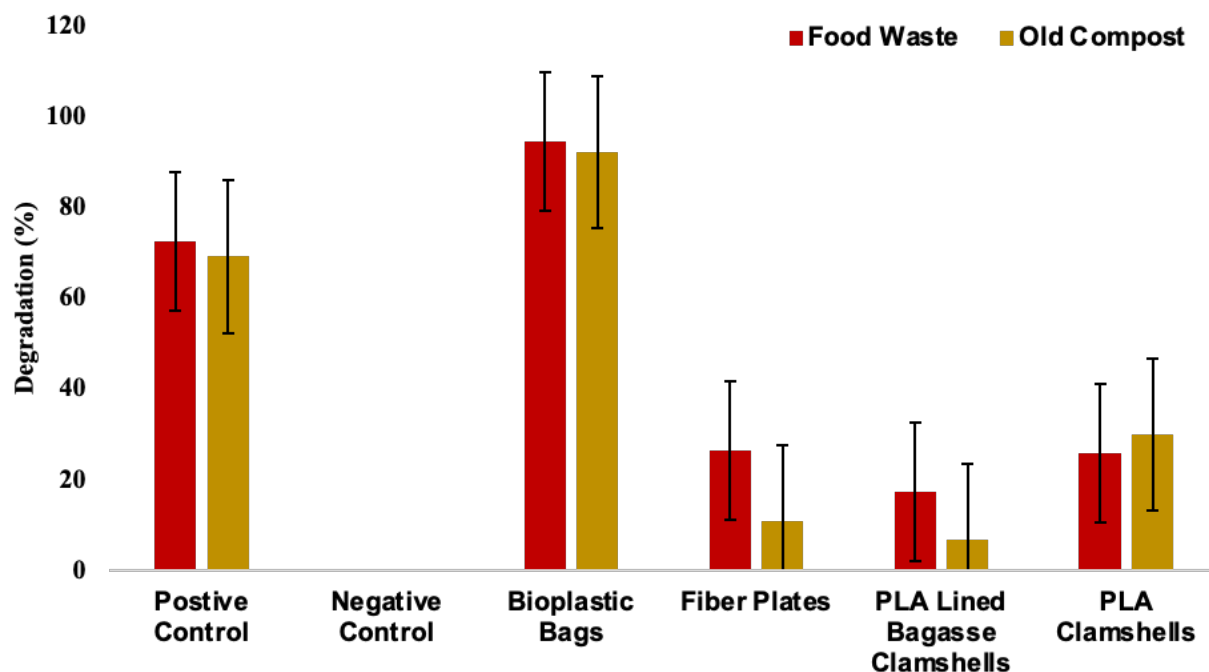


Figure 3.6 Average percent degradation of six different FSP tested during commercial-scale composting at 60% moisture content using food waste (red) and old compost (gold).

The PIGE spectroscopy data for the fiber plate (**Figure 3.7a**) and the PLA lined bagasse clamshells (**Figure 3.7b**) from commercial-scale composting using food waste and old compost as the inoculum. While using food waste as the inoculum, the concentration of fluorine on the fiber plate changed from 883 ± 52 ppm to 831 ± 512 ppm, and for the PLA lined bagasse clamshell the fluorine concentration changed from 854 ± 50 ppm to 687 ± 321 ppm. Similarly, in old compost the fluorine concentration of the fiber plate went from 883 ± 52 ppm to 639 ± 90 ppm, and for the PLA lined bagasse clamshell the fluorine concentration changed from 854 ± 50 ppm to 708 ± 129 ppm. Both these FSP had less than 30% mass loss during commercial-scale composting which once again could just be the unbleached plant fiber, bamboo, and sugarcane bagasse degrading to CO_2 , water, and biomass rather than any PFAS degradation. It is especially challenging to degraded FSP lined with PLA and other polymers.

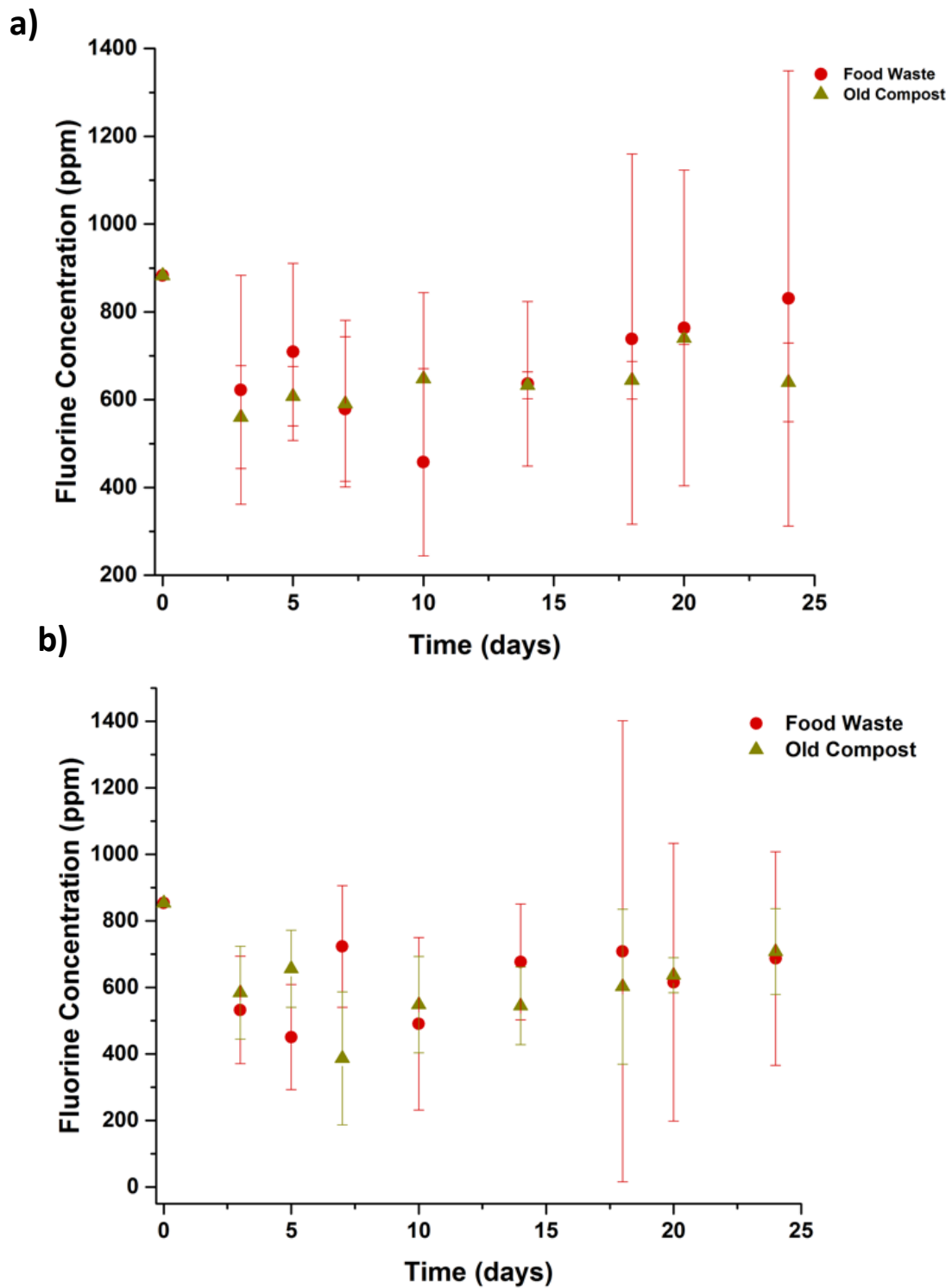


Figure 3.7 Change in fluorine concentration on a) the fiber plate , b) PLA lined bagasse clamshell over 24 days of commercial-scale composting at 60% moisture content using food waste (red) and old compost (gold).

Part II. Synthesis & Characterization of Adsorbents to Filter PFAS from Water

Characterization of MHO

The environmental scanning electron microscope (ESEM) image of the MHO ceramic monolith is shown in **Figure 3.8a**. The image highlights both the macropores (>50nm) and the small black dots that represent the mesopores (2-50nm). The monoclinic crystal structure of the MHO ceramic was determined using X-ray Diffraction (XRD) and compared to literature values from the Inorganic crystal structure database (ICSD)⁴⁰ as shown in **Figure 3.8b**. The FTIR in **Figure 3.8c** illustrates the surface of the MHO. Peaks between 400-800 cm^{-1} describe the Hf-O and Hf-O₂ stretches corresponding to monoclinic hafnium oxide. The peaks between 1250-1600 cm^{-1} correspond to carbonates that originate from NMF during the hydrolysis stage of the sol-gel synthesis. The peaks at 2390 cm^{-1} and 2900 cm^{-1} correspond to carbon dioxide bonded to the Lewis acid site, and water on the hydrophilic surface respectively. The Brunauer-Emmet-Teller (BET) surface area of MHO was calculated to be $10.5 \pm 0.6 \text{ m}^2/\text{g}$ using the linear region of the nitrogen gas adsorption isotherm.

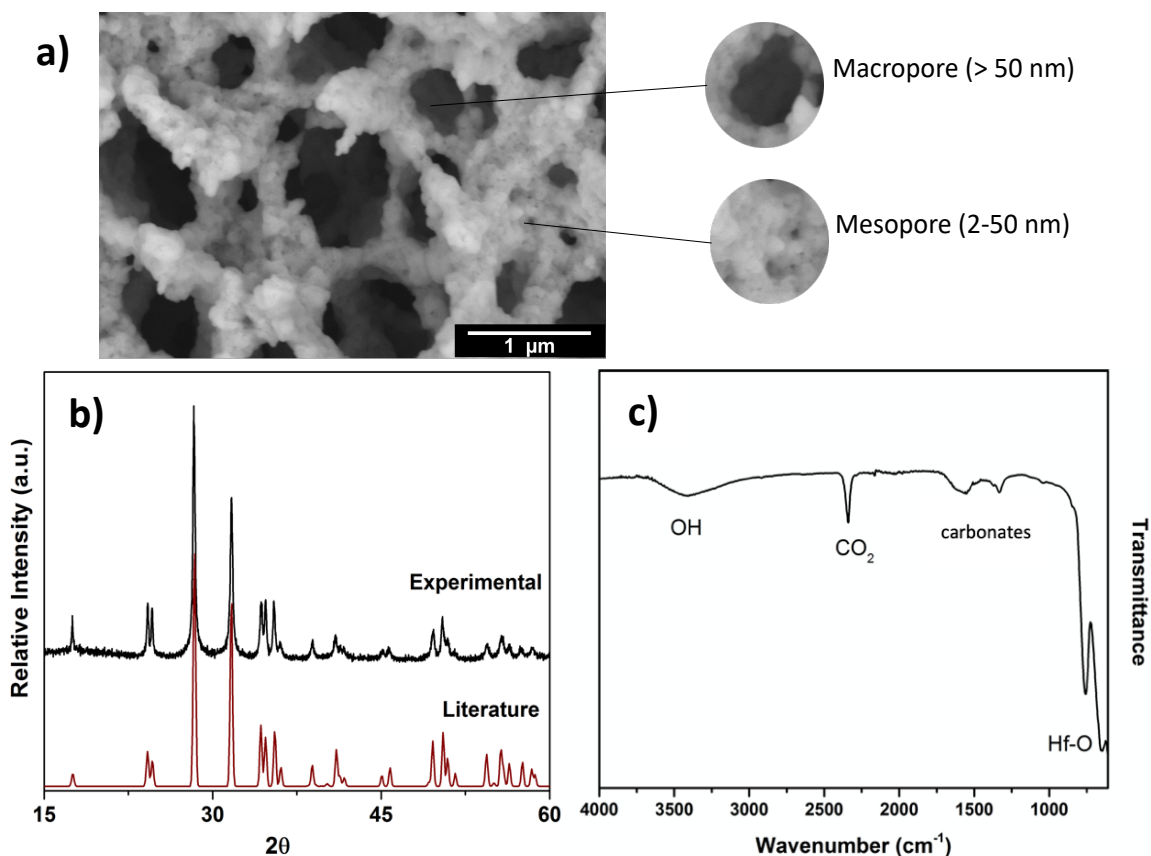


Figure 3.8 a) ESEM image of MHO monolith illustrating both macropores and mesopores, b) XRD pattern of experimentally synthesized MHO (black) overlaid with literature value of MHO (ICSD 57385), c) FTIR spectrum illustrating functional groups on surface of MHO.

Characterization of M-MOF-74 (M=Ni,Mg)

The SEM image for the Ni-MOF-74 and Mg-MOF-74 are shown in **Figure 3.9a** and **Figure 3.9c** respectively. The image shows aggregates of small elongated crystals each of which appear to be 1-2 μm in length that aggregate to form flower-like shapes that have a diameter of about 5 μm. The XRD pattern for experimentally obtained Ni-MOF-74 and Mg-MOF-74 are illustrated in **Figure 3.9b** and **Figure 3.9d**. The experimentally obtained patterns were compared to the published spectra in the Cambridge Crystallographic Data Centre (CCDC) database and the peaks aligned in agreement with the published spectra of the rhombohedral MOF-74.^{41,42} The BET surface area of Ni-MOF-74 and Mg-MOF-74 was calculated to be $917.4 \pm 21.5 \text{ m}^2/\text{g}$ and $1025.2 \pm 23.1 \text{ m}^2/\text{g}$ respectively using the linear region of the nitrogen adsorption isotherm.

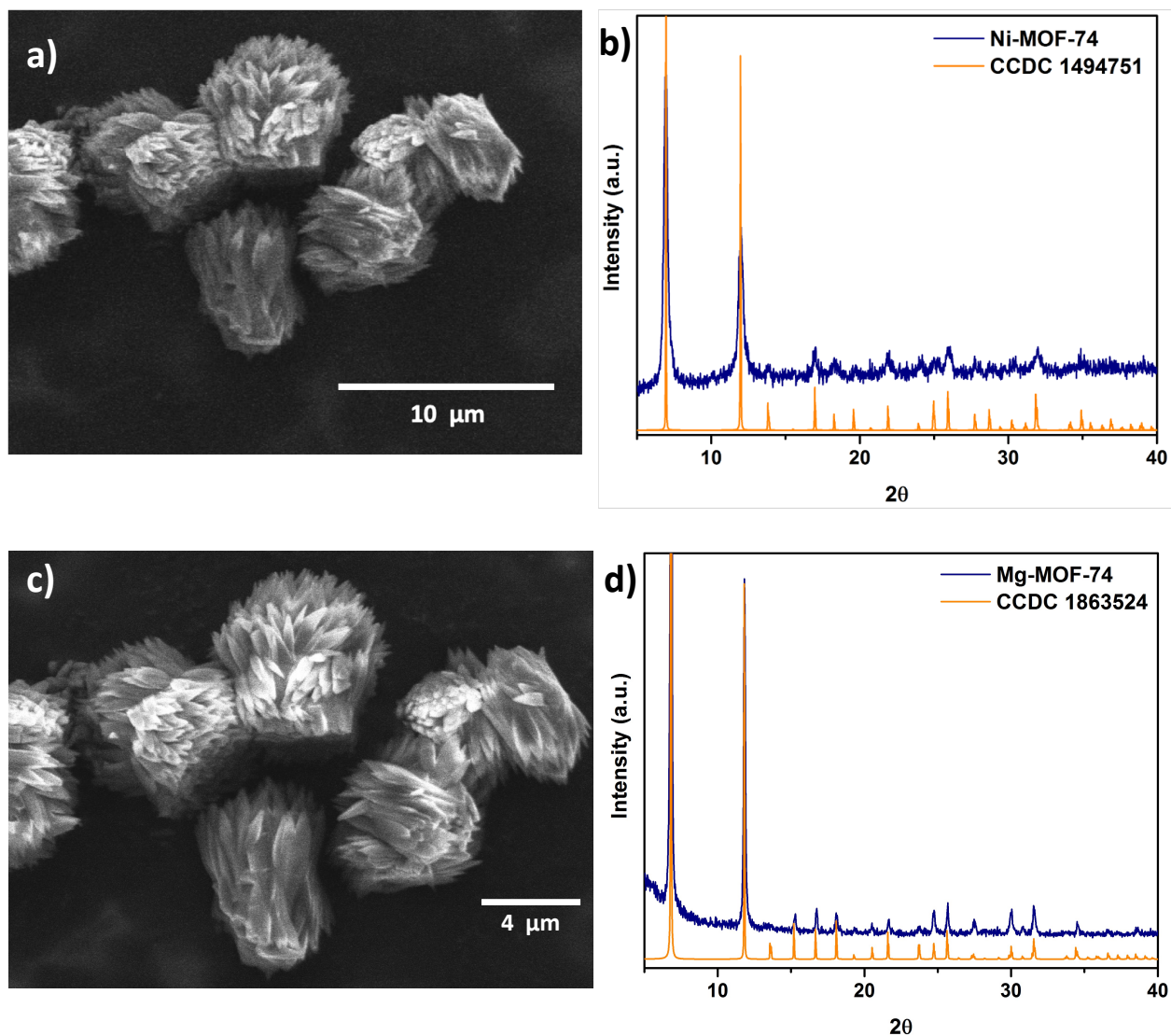


Figure 3.9 a) ESEM image of Ni-MOF-74 illustrating aggregates of elongated crystals, b) XRD pattern of Ni-MOF-74 synthesized and overlaid with published pattern (CCDC 1494751), c) ESEM image of Mg-MOF-74 depicting aggregates of elongated crystals, d) XRD pattern of Mg-MOF-74 synthesized and overlaid with published pattern (CCDC 1863524).

Filtration Results of PFAS Using MHO

To determine the potential of the synthesized adsorbents to filter PFAS from water, 100 ppm solution of PFBA, PFHxA, and PFOA were prepared in ultrapure water. This concentration is higher than what would be typically found in drinking water but is comparable to concentrations found at industrial manufacturing facilities waste streams.^{43,44} The M-MOF-74 that were synthesized were not able to remove any PFAS from

solution. This is due to the fact that M-MOF-74 have an average pore size of 1-2 nm which is too small to remove PFAS molecules from solution. The pores are also extremely hydrophilic and are filled with moisture the moment they are exposed to air. This limits their applicability to remove PFAS from water. However, MHO synthesized has both macropores (1 μm) and mesopores (2-50 nm) which is ideal for PFAS adsorption. ^{19}F NMR was used to quantify percent removal of PFAS by MHO and the resulting spectra are shown in **Figure 3.10**. The peak at -81 ppm corresponds to the terminal CF_3 group in the PFAS molecule. MHO had an average removal efficiency of 31.1%, 45.6 %, and 50.2% for PFBA, PFHxA, and PFOA respectively. The quantity of PFAS adsorbed per gram of MHO (q_t) was 0.78 mg/g, 1.14 mg/g, and 1.31 mg/g for PFBA, PFHxA, and PFOA respectively. As the chain length increases the percent removal of PFAS as well as the quantity of PFAS adsorbed per gram of MHO increases due to the increased hydrophobicity of the molecule. The hydrophobic molecules will have increased Van der Waal's (VdW) interactions with the hydrophilic surface of MHO. VdW interactions are weak intermolecular forces resulting from electrostatic interactions in typically non-attracting molecules due to asymmetric electronic distributions. Small electronic dipoles are created which can induce dipoles in complementary surfaces. Larger molecules have a higher propensity of remaining in the adsorbed state and that is due to VdW interactions. The longer the chain the more electron clouds that can be distorted and can interact with the surface of MHO.

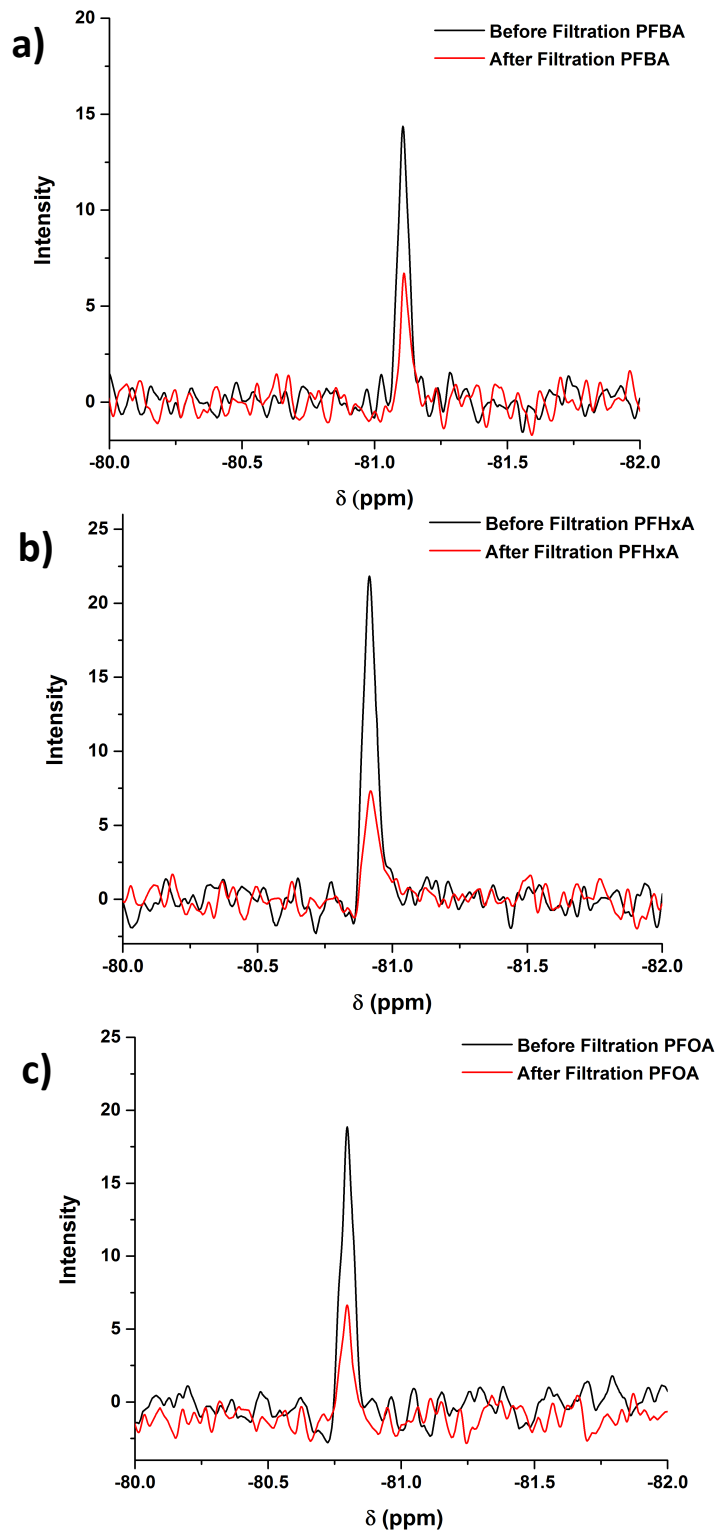


Figure 3.10 ^{19}F NMR spectra showing terminal CF_3 peak of PFAS molecule before and after filtration using MHO monolith with a) PFBA, b) PFHxA, c) PFOA.

Analysis of Solid MHO After Filtration

The solid surface of MHO was analyzed after filtration with PFBA, PFHxA, and PFOA using ATR-FTIR to confirm adsorption of PFAS on the surface. The resulting spectra are shown in **Figure 3.11a-d**. The FTIR peaks between 400-800 cm^{-1} in **Figure 3.11a-c** on the magenta spectra of the MHO before filtration correspond to monoclinic hafnium oxide, the formate ligand binding on the hafnium shown by the peaks between 1200-1600 cm^{-1} , and the carbon dioxide and water peaks at 2390 cm^{-1} and 2900 cm^{-1} respectively. The blue spectra in **Figure 3.11a** corresponds to PFBA, the shortest PFAS tested with only four carbons. PFBA has a carboxylic acid head group which is represented by the carboxylate peak at 1750 cm^{-1} . The peaks corresponding to PFAS appear in the range of 950-1450 cm^{-1} . The peak at 1050 cm^{-1} denotes the C-C bond in the PFBA chain, the peaks at 1149 cm^{-1} , 1200 cm^{-1} , and 1240 cm^{-1} correspond to the symmetric CF_2 the asymmetric stretching of CF_2 and CF_3 , and the asymmetric CF_2 stretch.⁴⁵ Similar peaks are observed for PFHxA and PFOA in **Figure 3.11b** and **Figure 3.11c**. The black spectra in **Figure 3.11a** illustrates the surface of MHO after filtration with PFBA and we observe the peaks corresponding to PFAS in the range of 950-1450 cm^{-1} as well as the carboxylate peak at 1750 cm^{-1} . The spectra for MHO after filtration with PFHxA, the six carbon PFAS, is shown in **Figure 3.11b** and contains similar peaks to previously described spectra for MHO after filtration with PFBA in **Figure 3.11a**. However, after filtration with PFOA the resulting spectra looked different. PFOA is a hydrophobic PFAS with eight carbons in the chain and a solubility of 3.4-9.5 g/L.⁴⁶ In contrast PFBA and PFHxA are hydrophilic and have solubilities of 214 g/L and 21.7 g/L respectively.⁴⁷ Due to the reduced solubility and increased hydrophobicity for PFOA it is difficult to observe the peaks in FTIR so we present the entire spectrum in **Figure 3.11c** and a more focused spectra from 800-1800 cm^{-1} in **Figure 3.11d**. The carboxylate peak of PFOA is shown in **Figure 3.11c** in the blue spectra at 1750 cm^{-1} , however the surface of MHO after filtration denoted by the black spectra shows the peak at 1650 cm^{-1} . This shift is due to the fact that solid PFOA has the undissociated carboxylate group peak (COOH), whereas in solution the carboxylate group deprotonates and the COO^- peak appears at 1650 cm^{-1} . The PFOA peaks on the surface of MHO can be more clearly observed in the black spectra

shown in **Figure 3.11d**. The small peaks at 1149 cm^{-1} , 1200 cm^{-1} , and 1240 cm^{-1} correspond to the symmetric CF_2 the asymmetric stretching of CF_2 and CF_3 , and the asymmetric CF_2 stretch in PFOA.

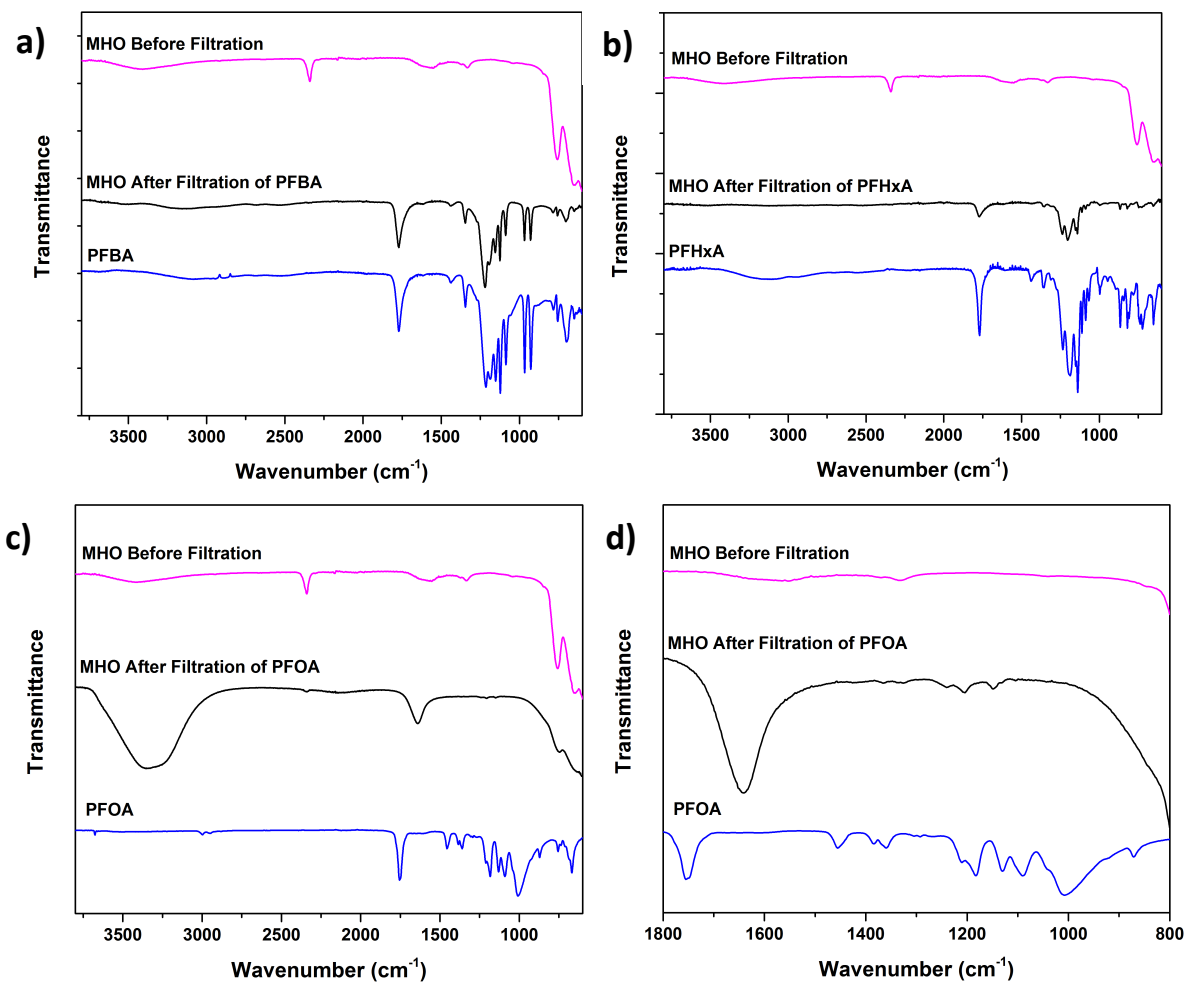


Figure 3.11 FTIR spectra of a) MHO before filtration, MHO after filtration with PFBA, and PFBA standard, b) MHO before filtration, MHO after filtration with PFHxA, and PFHxA standard, c) MHO before filtration, MHO after filtration with PFOA, and PFOA standard, d) Inset of MHO before filtration, MHO after filtration with PFOA, and PFOA standard from $800\text{-}1800\text{ cm}^{-1}$.

Conclusions

Through bench-scale composting experiments with cow manure it was observed that 60% moisture content was 25% better for degrading FSP than 45% moisture content. In both the bench and commercial scale composting experiments the green bioplastic bags had the highest degradation rates when compared to other thicker FSP materials like the fiber plate, PLA clamshell, and white PLA lined clamshell. The fluorine content on the FSP increased during the 24-day-composting period due to mass loss of the unbleached plant fiber, bamboo, and sugarcane bagasse degrading to CO₂, water, and biomass rather than any PFAS degradation. It is especially challenging to degraded FSP lined with PLA and other polymers. During filtration of PFAS using MHO the longer chain PFAS had higher removal efficiency due to the increased hydrophobicity of the molecule.

Future work for this project will involve evaluating the specific microbial communities in the compost and attached on the FSP to be able to correlate a certain microorganism with degradation of FSP and PFAS. Then the microorganism can be concentrated to maximize degradation of FSP and PFAS. This work evaluated the effects of only two types of inoculum in the field, food waste and old compost, however using other microbial inoculants such as cow manure would provide further understanding of degradation ability. Unfortunately cow manure is limited and can only be used in smaller bench-scale experiments for the time being. The kinetics and mechanism behind the interaction between the surface of MHO and the hydrophobic PFOA will be further discussed in Chapter 4 along with the regeneration of the MHO.

Acknowledgements

I would like to acknowledge the California department of Resources, Recycling, and Recovery (CalRecycle) award number DRR18040 for funding this project, University of California Davis for startup funding for this project, NSF-MRI grant DMR-1725618 for the use of the Thermofisher Quattro environmental scanning electron microscope at the Advanced Materials Characterization and Testing

Laboratory (AMCAT) at UC Davis. We would like to acknowledge support from the Cottrell Scholar program supported by the Research Corporation for Science Advancement (RCSA 26780) as well as the National Science Foundation Faculty Early Career Development program (DMR-2044403). I would like to thank Dr. Maureen Kinyua from the Department of Civil and Environmental Engineering at UC Davis and her students Gandhar Pandit, Jessica Hazard, Konane Gurfield, and students Myar Abou-Alfotouh for assistance with bench-scale composting experiments. I want to thank Will Kelly, Grey Kelly, and Chloe Kelly of the Napa Recycling and Composting Facility for helping with our commercial-scale composting experiments. I would like to acknowledge Professor Graham Peaslee and his students; Molly DeLuca and Arthur Alvarez at the University of Notre-Dame, Indiana for their assistance with Particle-Induced Gamma Ray Emission (PIGE) spectroscopy data processing. I want to thank Samuel Janisse from the Heffern lab for assistance with LC-MS.

References

- 1 Z. Abunada, M. Y. D. Alazaiza and M. J. K. Bashir, An Overview Of Per- And Polyfluoroalkyl Substances (PFAS) In The Environment: Source, Fate, Risk And Regulations, *Water*, 2020, **12**, 3590.
- 2 G. Glenn, R. Shogren, X. Jin, W. Orts, W. Hart-Cooper and L. Olson, Per- And Polyfluoroalkyl Substances And Their Alternatives In Paper Food Packaging, *Compr. Rev. Food Sci. Food Saf.*, 2021, 1541-4337.12726.
- 3 A. Ramírez Carnero, A. Lestido-Cardama, P. Vazquez Loureiro, L. Barbosa-Pereira, A. Rodríguez Bernaldo de Quirós and R. Sendón, Presence Of Perfluoroalkyl And Polyfluoroalkyl Substances (PFAS) In Food Contact Materials (FCM) And Its Migration To Food, *Foods*, 2021, **10**, 1443.
- 4 Y. Xu, G. O. Noonan and T. H. Begley, Migration Of Perfluoroalkyl Acids From Food Packaging To Food Simulants, *Food Addit. Contam. Part A*, 2013, **30**, 899–908.

- 5 J. Kowalczyk, S. Ehlers, P. Fürst, H. Schafft and M. Lahrssen-Wiederholt, Transfer Of Perfluorooctanoic Acid (PFOA) And Perfluorooctane Sulfonate (PFOS) From Contaminated Feed Into Milk And Meat Of Sheep: Pilot Study, *Arch. Environ. Contam. Toxicol.*, 2012, **63**, 288–298.
- 6 G. B. Post, Recent US State And Federal Drinking Water Guidelines For Per- And Polyfluoroalkyl Substances, *Environ. Toxicol. Chem.*, 2021, **40**, 550–563.
- 7 E. M. Sunderland, X. C. Hu, C. Dassuncao, A. K. Tokranov, C. C. Wagner and J. G. Allen, A Review Of The Pathways Of Human Exposure To Poly- And Perfluoroalkyl Substances (PFASs) And Present Understanding Of Health Effects, *J. Expo. Sci. Environ. Epidemiol.*, 2019, **29**, 131–147.
- 8 P. Grandjean, C. Heilmann, P. Weihe, F. Nielsen, U. B. Mogensen, A. Timmermann and E. Budtz-Jørgensen, Estimated Exposures To Perfluorinated Compounds In Infancy Predict Attenuated Vaccine Antibody Concentrations At Age 5-Years, *J. Immunotoxicol.*, 2017, **14**, 188–195.
- 9 L. A. Schaidler, S. A. Balan, A. Blum, D. Q. Andrews, M. J. Strynar, M. E. Dickinson, D. M. Lunderberg, J. R. Lang and G. F. Peaslee, Fluorinated Compounds In U.S. Fast Food Packaging, *Environ. Sci. Technol. Lett.*, 2017, **4**, 105–111.
- 10 Z. Li, H. Lu, L. Ren and L. He, Experimental And Modeling Approaches For Food Waste Composting: A Review, *Chemosphere*, 2013, **93**, 1247–1257.
- 11 S. E. Vergara and W. L. Silver, Greenhouse Gas Emissions From Windrow Composting Of Organic Wastes: Patterns And Emissions Factors, *Environ. Res. Lett.*, 2019, **14**, 124027.
- 12 X. F. Lou and J. Nair, The Impact Of Landfilling And Composting On Greenhouse Gas Emissions – A Review, *Bioresour. Technol.*, 2009, **100**, 3792–3798.
- 13 M. Rastogi, M. Nandal and L. Nain, Seasonal Variation Induced Stability Of Municipal Solid Waste Compost: An Enzyme Kinetics Study, *SN Appl. Sci.*, 2019, **1**, 849.

- 14 E. Kim, D.-H. Lee, S. Won and H. Ahn, Evaluation Of Optimum Moisture Content For Composting Of Beef Manure And Bedding Material Mixtures Using Oxygen Uptake Measurement, *Asian-Australasian J. Anim. Sci.*, 2015, **29**, 753–758.
- 15 D. Roy, A. Azaïs, S. Benkaraache, P. Drogui and R. D. Tyagi, Composting Leachate: Characterization, Treatment, And Future Perspectives, *Rev. Environ. Sci. Bio/Technology*, 2018, **17**, 323–349.
- 16 R. Bakhshoodeh, N. Alavi, M. Majlesi and P. Paydary, Compost Leachate Treatment By A Pilot-Scale Subsurface Horizontal Flow Constructed Wetland, *Ecol. Eng.*, 2017, **105**, 7–14.
- 17 Y. J. Choi, R. Kim Lazcano, P. Yousefi, H. Trim and L. S. Lee, Perfluoroalkyl Acid Characterization In U.S. Municipal Organic Solid Waste Composts, *Environ. Sci. Technol. Lett.*, 2019, **6**, 372–377.
- 18 J. Zhang, Z. Huang, L. Gao, S. Gray and Z. Xie, Study Of MOF Incorporated Dual Layer Membrane With Enhanced Removal Of Ammonia And Per-/Poly-Fluoroalkyl Substances (PFAS) In Landfill Leachate Treatment, *Sci. Total Environ.*, 2022, **806**, 151207.
- 19 M. Simonič, Compost Leachate Treatment Using Polyaluminium Chloride And Nanofiltration, *Open Chem.*, 2017, **15**, 123–128.
- 20 F. A. Hussain, J. Zamora, I. M. Ferrer, M. Kinyua and J. M. Velázquez, Adsorption Of Crude Oil From Crude Oil–Water Emulsion By Mesoporous Hafnium Oxide Ceramics, *Environ. Sci. Water Res. Technol.*, , DOI:10.1039/D0EW00451K.
- 21 Y. Zhang, J. R. Vallin, J. K. Sahoo, F. Gao, B. W. Boudouris, M. J. Webber and W. A. Phillip, High-Affinity Detection And Capture Of Heavy Metal Contaminants Using Block Polymer Composite Membranes, *ACS Cent. Sci.*, 2018, **4**, 1697–1707.
- 22 T. J. Westbury, University of Wisconsin, 2014.

- 23 E. E. Ritter, M. E. Dickinson, J. P. Harron, D. M. Lunderberg, P. A. DeYoung, A. E. Robel, J. A. Field and G. F. Peaslee, PIGE As A Screening Tool For Per- And Polyfluorinated Substances In Papers And Textiles, *Nucl. Instruments Methods Phys. Res. Sect. B Beam Interact. with Mater. Atoms*, 2017, **407**, 47–54.
- 24 J. T. Wilkinson, S. R. McGuinness and G. F. Peaslee, External Beam Normalization Measurements Using Atmospheric Argon Gamma Rays, *Nucl. Instruments Methods Phys. Res. Sect. B Beam Interact. with Mater. Atoms*, 2020, **484**, 1–4.
- 25 I. M. Ferrer-Lassala, SUNY Buffalo, 2013.
- 26 T. Grant Glover, G. W. Peterson, B. J. Schindler, D. Britt and O. Yaghi, MOF-74 Building Unit Has A Direct Impact On Toxic Gas Adsorption, *Chem. Eng. Sci.*, 2011, **66**, 163–170.
- 27 P. Zhao, X. Xia, J. Dong, N. Xia, X. Jiang, Y. Li and Y. Zhu, Short- And Long-Chain Perfluoroalkyl Substances In The Water, Suspended Particulate Matter, And Surface Sediment Of A Turbid River, *Sci. Total Environ.*, 2016, **568**, 57–65.
- 28 V. Siracusa, Microbial Degradation Of Synthetic Biopolymers Waste, *Polymers (Basel)*, , DOI:10.3390/polym11061066.
- 29 A. Makan, O. Assobhei and M. Mountadar, Effect Of Initial Moisture Content On The In-Vessel Composting Under Air Pressure Of Organic Fraction Of Municipal Solid Waste In Morocco, *Iranian J. Environ. Health Sci. Eng.*, 2013, **10**, 3.
- 30 J. Rydz, W. Sikorska, M. Kyulavska and D. Christova, Polyester-Based (Bio)Degradable Polymers As Environmentally Friendly Materials For Sustainable Development, *Int. J. Mol. Sci.*, 2014, **16**, 564–596.
- 31 N. Mohanan, Z. Montazer, P. K. Sharma and D. B. Levin, Microbial And Enzymatic Degradation Of Synthetic Plastics, *Front. Microbiol.*, , DOI:10.3389/fmicb.2020.580709.

- 32 K. . Ho, A. L. Pometto and A. Gadea-Rivas, Degradation Of Polylactic Acid (PLA) Plastic In Costa Rican Soil And Iowa State University Compost Rows, *J. Polym. Environ.*, 1999, **7**, 173–177.
- 33 R. Guo, G. Li, T. Jiang, F. Schuchardt, T. Chen, Y. Zhao and Y. Shen, Effect Of Aeration Rate, C/N Ratio And Moisture Content On The Stability And Maturity Of Compost, *Bioresour. Technol.*, 2012, **112**, 171–178.
- 34 A. Nestler, A. Montgomery and L. Heine, *Evaluating Alternatives to Food Packaging Materials Containing Per- or Polyfluorinated Substances (PFAS)*, Oregon, 2019.
- 35 D. X. Trier, C. Taxvig, A. K. Rosenmai and G. A. Pedersen, *PFAS in Paper and Board for Food Contact*, Nordic Council of Ministers, 2018.
- 36 S. M. Emadian, T. T. Onay and B. Demirel, Biodegradation Of Bioplastics In Natural Environments, *Waste Manag.*, 2017, **59**, 526–536.
- 37 M. Cucina, P. De Nisi, L. Trombino, F. Tambone and F. Adani, Degradation Of Bioplastics In Organic Waste By Mesophilic Anaerobic Digestion, Composting And Soil Incubation, *Waste Manag.*, 2021, **134**, 67–77.
- 38 K. J. Jem and B. Tan, The Development And Challenges Of Poly (Lactic Acid) And Poly (Glycolic Acid), *Adv. Ind. Eng. Polym. Res.*, 2020, **3**, 60–70.
- 39 M. Rastogi, M. Nandal and B. Khosla, Microbes As Vital Additives For Solid Waste Composting, *Heliyon*, 2020, **6**, e03343.
- 40 D. M. Adams, S. Leonard, D. R. Russell and R. J. Cernik, X-Ray Diffraction Study Of Hafnia Under High Pressure Using Synchrotron Radiation, *J. Phys. Chem. Solids*, 1991, **52**, 1181–1186.
- 41 W. Wong-Ng, J. A. Kaduk, H. Wu and M. Suchomel, Synchrotron X-Ray Studies Of Metal-Organic Framework M₂ (2,5-Dihydroxyterephthalate), M = (Mn, Co, Ni, Zn) (MOF74), *Powder*

- Diffr.*, 2012, **27**, 256–262.
- 42 S. E. Henkelis, S. M. Vornholt, D. B. Cordes, A. M. Z. Slawin, P. S. Wheatley and R. E. Morris, A Single Crystal Study Of CPO-27 And UTSA-74 For Nitric Oxide Storage And Release, *CrystEngComm*, 2019, **21**, 1857–1861.
- 43 L. C. Green, *Assessing the Risk Presented by PFOA and PFOS in Drinking Water*, New England, 2019.
- 44 C. Y. Tang, Q. S. Fu, A. P. Robertson, C. S. Criddle and J. O. Leckie, Use Of Reverse Osmosis Membranes To Remove Perfluorooctane Sulfonate (PFOS) From Semiconductor Wastewater, *Environ. Sci. Technol.*, 2006, **40**, 7343–7349.
- 45 X. Gao and J. Chorover, Adsorption Of Perfluorooctanoic Acid And Perfluorooctanesulfonic Acid To Iron Oxide Surfaces As Studied By Flow-Through ATR-FTIR Spectroscopy, *Environ. Chem.*, 2012, **9**, 148.
- 46 L. Benbrahim-Tallaa, B. Lauby-Secretan, D. Loomis, K. Z. Guyton, Y. Grosse, F. El Ghissassi, V. Bouvard, N. Guha, H. Mattock and K. Straif, Carcinogenicity Of Perfluorooctanoic Acid, Tetrafluoroethylene, Dichloromethane, 1,2-Dichloropropane, And 1,3-Propane Sultone, *Lancet Oncol.*, 2014, **15**, 924–925.
- 47 T. Pancras, G. Schrauwen, T. Held, K. Baker, I. Ross and H. Slenders, *Environmental fate and effects of poly- and perfluoroalkyl substances (PFAS)*, Brussels, 2016.

4 Chapter 4: Adsorption of Perfluorooctanoic Acid from Water by pH-modulated Brönsted Acid and Base Sites in Mesoporous Hafnium Oxide Ceramics

Abstract

Per- and polyfluoroalkyl substances (PFAS) are increasingly appearing in drinking water sources globally. Our work focuses specifically on the adsorption of the legacy perfluorooctanoic acid (PFOA) using mesoporous hafnium oxide (MHO) ceramic synthesized via a sol-gel process. Experiments were performed at varying pH to determine the effect of surface charge on adsorption capacity of PFOA by MHO and to postulate adsorption behavior. At pH 2.3 the adsorption capacity of PFOA on MHO was 20.9 mg/g, whereas in a more alkaline pH of 6.3 it was much lower at 9.2 mg/g. This was due to increased coulombic attractions at lower pH between the positively charged conjugate acid active sites on MHO surface and negatively charged deprotonated PFOA anion in solution. After adsorption the solid MHO was regenerated via calcination, reducing the amount of toxic solid waste to be disposed since the adsorbent is regenerated, and the PFOA is completely removed.

Introduction

Per- and polyfluoroalkyl substances (PFASs) are a group of over 4000 industrial chemicals that have been widely synthesized for applications in water-proof clothing, carpets, cookware, and food packaging.¹⁻⁵ They are used in food packaging and waterproof gear as they are thermally resistant, hydrophobic, and oleophobic.^{6,7} The widespread industrial applicability of PFAS has led to large concentrations in already vulnerable aquatic environments.⁸ Perfluorooctanoic acid (PFOA) in particular, has become a serious cause for concern because it is environmentally persistent due to its high water solubility (9.5 g/L), and low volatility.⁹⁻¹² PFOA does not bind well to soil or sediments, so it tends to persist in aquatic environments.

In some cases, PFOA can present itself in drinking water leading to serious health effects.¹³ PFAS in human bodies can target organs like the liver and kidney,¹⁴ and human bodily fluids like blood^{15,16} which can lead to thyroid disease,¹⁷ ulcerative colitis,¹⁸ reduced fertility,¹⁹ and several types of cancer depending on length of exposure.^{20,21}

Developing techniques to remove PFOA from natural and drinking waters is of the essence. Various technologies exist to remove PFOA from water such as reverse osmosis,²² electrochemical degradation using Yb-doped Ti/SnO₂-Sb/PbO₂ anodes,²³ and photochemical decomposition by coexisting ferric ions and oxalic acids.²⁴ While reverse osmosis membranes are ideal due to their high removal capacity, modularity, and flexibility,²⁵ the process is non-destructive to PFAS creating secondary waste, very energy intensive,²⁶ and most reverse osmosis membranes are very susceptible to fouling resulting in increased cost of treatment.²⁷ Electrochemical degradation and photochemical decomposition of PFOA is a destructive removal technique that destroys other contaminants in water however, it leads to the generation of shorter chain PFAS, carbon dioxide, and fluoride ions which are still toxic and harmful to the environment.^{28,29} Consequently, economically feasible technologies that are functional in extreme chemical environments are lacking that lower PFOA concentrations to safe levels.

Alternatively, adsorption-based technologies are preferred due to their efficiency and economic benefits.³⁰ Granular activated carbon (GAC) has been extensively studied due to its low cost and broad usability. However, the particle size of GAC (>100 μm) leads to relatively slow PFOA adsorption kinetics, which could also explain why the breakthrough point of PFOA in GAC is very fast.³¹ Regenerating GAC is also more complex as it requires heating at high temperatures (700-900°C)³² as well as chemical reactivation.³³ The high regeneration temperature may alter the physical and chemical properties of GAC, which in turn could affect the adsorption behavior.³⁴ Other adsorbents such as ion-exchange resins,³⁵ alumina,³⁶ and quaternized cotton³⁷ are not thermally and chemically stable, which inhibits their regeneration efficacy.³⁸ Mesoporous materials are beneficial for adsorption due to the ordered network of pores that can be tuned in size to trap contaminants, and chemically functionalized for selective adsorption.³⁹ There is a need for

mesoporous adsorbents that have faster adsorption kinetics, are stable in harsh chemical conditions, and are thermally stable during regeneration.

Mesoporous hafnium oxide, a group IV transition metal oxide, is an attractive PFOA adsorption candidate. The high thermal and chemical stability of MHO ceramic results from its highly coordinated hafnium. Hafnium can coordinate to seven oxygen atoms, whereas silicon, also in group IV, can only coordinate to four. Additionally, the chemical stability stems from the three tunable active sites on MHO: Lewis acid sites originating from unoccupied hafnium d orbitals, Brønsted acid sites which donate a proton in basic media resulting in a negatively charged conjugate base active site, and Brønsted base sites which accept a proton in acidic media resulting in a positively charged conjugate acid active site (**Figure 4.1**).⁴⁰ These active sites are stimulated at different pH conditions and may facilitate favorable interactions between the contaminant and the MHO ceramic surface.

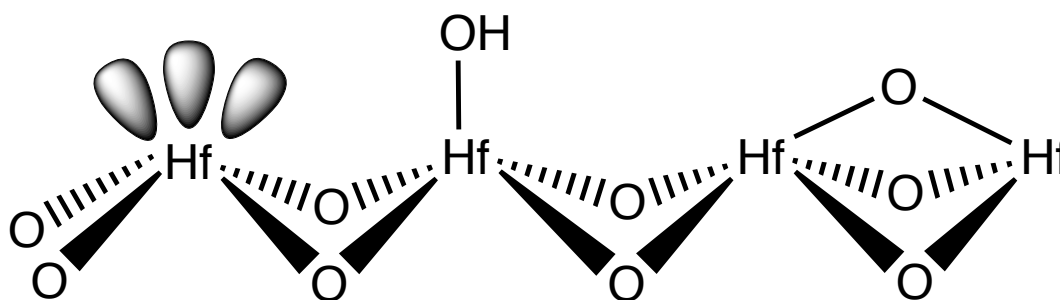


Figure 4.1 Three main active sites on the surface of hafnium oxide: Lewis acid site (left), Brønsted acid site (middle), and Brønsted base site (right).

The objective of this study is to investigate the kinetics and removal rate of PFOA from water using MHO ceramic under a range of pH conditions. MHO from sol-gel synthesis was used as the PFOA adsorbent. Adsorption experiments were performed over a period of twelve hours, which were then used to determine the maximum adsorption capacity of PFOA by MHO ceramic, the time needed to reach equilibrium, and construct adsorption isotherms. The concentrations of PFOA in liquid aliquots and solid MHO were measured using ¹⁹F nuclear magnetic resonance spectroscopy and Fourier transform infrared spectroscopy, respectively.

Materials & Methods

Chemicals and Materials

Hafnium(IV) tetrachloride (98%) was used as the Hafnium source. Acetone, hexanes, methanol, and pentane were all HPLC Plus (>99.9%). Hydrochloric acid (35.0–37.0%), sulfuric acid (95.0–98.0%), Sodium chloride (>99%) and deuterated water (D₂O) were used as purchased from Sigma-Aldrich. *N*-Methyl formamide (99%) and sodium hydroxide pellets (98%) were purchased from Alfa Aesar. Poly(ethylene oxide) (MW 100 000) was purchased from Polysciences Inc. Propylene oxide (99.5%) and Trifluoroacetic acid (99.5%) were purchased from Acros Organics. Perfluorooctanoic acid (>98%) was purchased from TCI America. Ultrapure water ($\geq 18.2 \text{ M}\Omega\cdot\text{cm}$) used for synthesis and adsorption kinetics experiments was obtained from a Thermo Scientific Barnstead E-Pure Ultrapure water purification system.

MHO Synthesis

MHO ceramic was synthesized using the sol–gel method detailed in our previous work.⁴¹ Briefly, 20 mL scintillation glass vials were treated in sequence with 0.1 M NaOH for 1 hour, 0.1 M HCl for 1 hour, and Rain-X overnight prior to the start of the synthesis. After removing the Rain-X, vials were rinsed with methanol three times and dried in an oven at 150°C for 1 hour. Hafnium (IV) chloride was first hydrolyzed in ultrapure water. *N*-methylformamide was added as a porogen, to increase the solution pH and induce phase separation. Polyethylene oxide was added to create a strong pore network. Additionally, propylene oxide was added to polymerize the clear liquid to a white gel. The gel was then aged at 50°C for three days. The monolith was successively washed with ultrapure water, methanol, acetone, hexanes, then pentane to remove any excess reagents. Lastly, the sample underwent heat treatment in air to 700°C to yield a crystalline white monolithic ceramic.

MHO Characterization

The distinctive mesostructured morphology of the as-synthesized MHO ceramic was confirmed by a Thermofisher Quattro ESEM. To avoid charge mitigation from insulating surfaces such as MHO, samples were placed on double-sided copper tape and operated at an accelerating voltage of 10 keV under low

vacuum. The phase purity and crystalline structure of the adsorbent was determined by powder XRD using a Bruker D8 Advance diffractometer with Cu K α radiation (1.5406 Å). Experimentally obtained diffraction patterns were then compared to literature patterns from the Inorganic Crystal Structure Database (ICSD) to confirm the structure. The surface of the MHO ceramic was analyzed before adsorption, after adsorption, and after heating to remove PFOA (500°C) using Fourier transform infrared (FTIR) spectroscopy. The Bruker Tensor 27 FTIR was equipped with an attenuated total reflectance (ATR) pike accessory. The experiment was performed using 32 scans, a resolution of 2 cm⁻¹, and a spectral range of 400–4000 cm⁻¹. Thermogravimetric analysis (TGA) was done using a NETSCH STA 449F3 instrument under high purity argon. It was heated from 20 °C to 750 °C at a rate of 10.0 °C min⁻¹. The surface area was measured by Brunauer-Emmet-Teller (BET) method with nitrogen adsorption using a Micromeritics Gemini VII surface area analyzer. The point of zero charge (pH_{PZC}) of MHO was analyzed using the pH drift method.⁴² The pH_{PZC} is the pH when the charge on the surface of the adsorbent is neutral. The first step is to prepare a 0.01M NaCl solution using ultra pure water. Six Falcon tubes were filled with 50 mL of 0.01M NaCl. Then, the pH values were adjusted using 0.1M NaOH and 0.1M H₂SO₄ to be pH 2,4,6,8,10, and 12. Once the pH of solutions had stabilized the pH were recorded as pH_{initial}. Then 150 mg of crushed MHO was added to each Falcon tube and placed on the benchtop shaker for 24 hours to reach equilibrium. pH after shaking was recorded as pH_{final}. The pH_{PZC} of MHO is the point when pH_{initial} = pH_{final}.

PFOA Adsorption Kinetics & Isotherm Models

PFOA adsorption experiments were performed using a Benchmark tabletop shaker. The white ceramic MHO was crushed and sieved to be between 0.6 mm and 2 mm. Each 50 mL Falcon tube contained 1.25 g of MHO ceramic and 50 mL of PFOA solution in the range of 200-1000 ppm. The concentration of PFOA used in the experiments was higher than the concentrations found typically in wastewater streams for ease of sample handling and analysis. The pH was adjusted in these experiments using 0.1M NaOH and 0.1M H₂SO₄. The tubes were shaken for twelve hours, and a 1 mL aliquot was extracted every two hours for analysis. At the end of the twelve hours, the solid MHO floated on top and was separated from the liquid

by filtration. The quantity of PFOA adsorbed per gram of MHO at a time t (q_t) was calculated using eq. 4.1:

$$q_t = \frac{(C_0 - C_t) \times V}{m} \quad (\text{eq. 4.1})$$

Where C_t is the concentration at a time t , C_0 is the initial PFOA concentration, m is the mass of MHO, and V is the total volume of solution used in the adsorption experiment. To determine the order of the adsorption of PFOA on MHO, the data was fit to the pseudo-first order (eq. 4.2) and pseudo-second order (eq. 4.3) kinetic equations as depicted below:

$$\ln(q_e - q_t) = \ln q_e - k_1 t \quad (\text{eq. 4.2})$$

$$\frac{t}{q_t} = \frac{1}{k_2 q_e^2} + \frac{t}{q_e} \quad (\text{eq. 4.3})$$

Where q_e is the adsorption capacity at equilibrium and q_t is the adsorption capacity at a time t and k_1 and k_2 are the rate constants for the pseudo-first order and pseudo-second order kinetic equations respectively. Langmuir (eq. 4.4) and Freundlich (eq. 4.5) adsorption isotherms were applied to further comprehend the adsorption of PFOA on MHO.

$$q_e = q_m K_L \frac{C_e}{1 + K_L C_e} \quad (\text{eq. 4.4})$$

$$q_e = K_F C_e^{1/n} \quad (\text{eq. 4.5})$$

Where q_e is the adsorption capacity of PFOA on MHO at equilibrium, q_m is the saturation adsorption capacity, C_e is the concentration of PFOA at equilibrium, n is a constant relating to surface heterogeneity, and K_L and K_F are the Langmuir and Freundlich constants respectively. All experiments were performed in triplicates and the average values are reported.

PFOA Liquid Analysis

The PFOA concentration in the liquid was quantitatively determined using ^{19}F nuclear magnetic resonance (NMR) spectroscopy on a Bruker 400 MHz spectrometer. The concentration was determined by integrating the area of the characteristic peak of the terminal CF_3 (-80.8 ppm) and comparing it to the area of the peak of the internal standard, trifluoroacetic acid (-76 ppm). Calibrations were performed with six standard solutions in the range of (9-2000 ppm). 200 μL of liquid was added to 400 μL of D_2O spiked with TFA in a 300 MHz Wilmad NMR tube.

Results & Discussion

Morphology and Crystal Structure of MHO Ceramic

The environmental scanning electron microscope (ESEM) image of the MHO ceramic powder is shown in **Figure 4.2a**. The particles in the image show very small black dots that represent the mesopores (2-50 nm) in the structure. The monoclinic crystal structure of the MHO ceramic was determined using X-ray Diffraction (XRD) and compared to literature values as shown in **Figure 4.2b**. The results of the determination of the pH at the point of zero charge (pH_{PZC}) of MHO via pH drift method are shown in **Figure 4.2c**. The pH_{PZC} was determined to be 4.7. The Brunauer-Emmet-Teller (BET) surface area of MHO was calculated using nitrogen gas adsorption isotherms to determine the porous surface area as shown in **Figure 4.2d**. The linear portion of the isotherm is used to determine BET surface area of MHO which was $10.5 \pm 0.6 \text{ m}^2/\text{g}$.

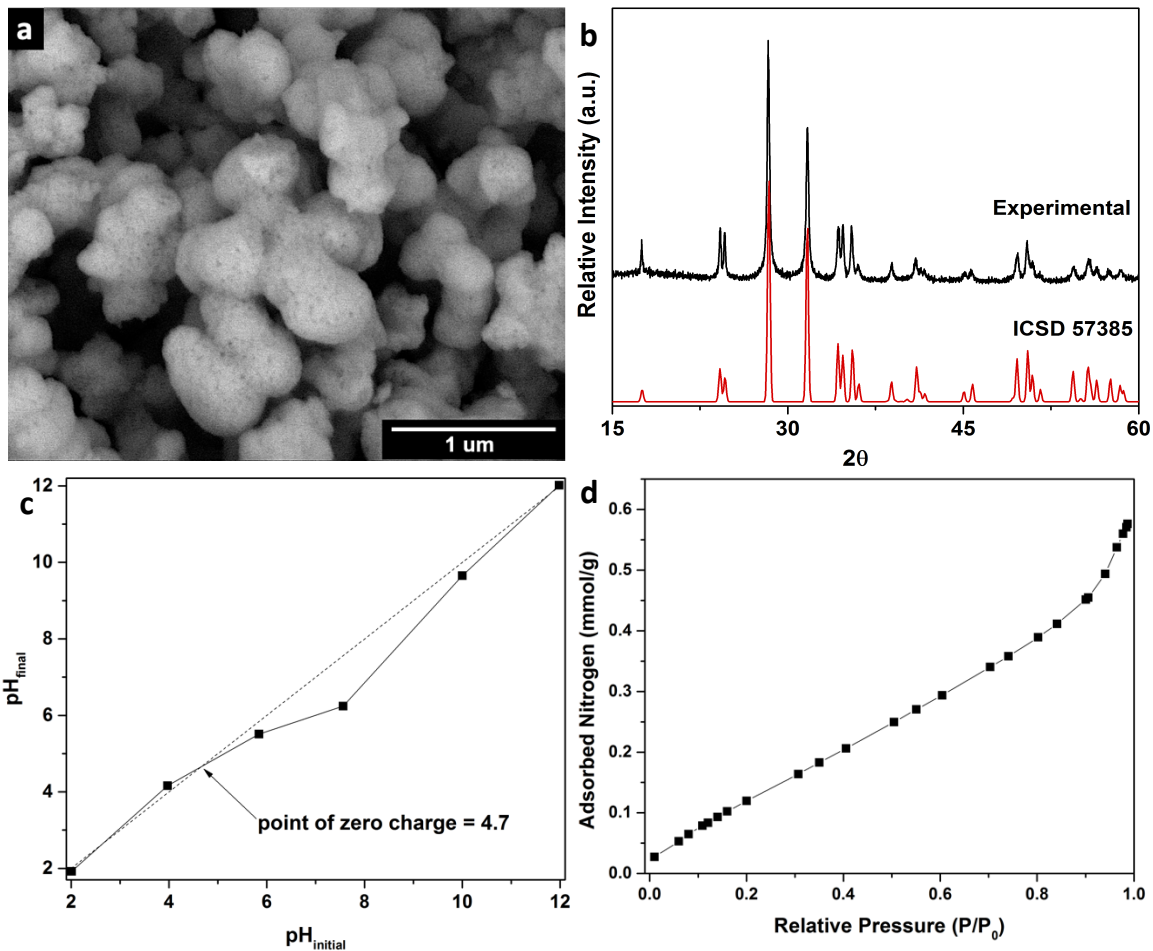


Figure 4.2 a) ESEM image depicting particles of MHO with mesopores. b) XRD pattern with diffraction peaks for monoclinic MHO ceramic synthesized (top) overlaid with the published spectrum for monoclinic MHO ceramic (bottom, ICSD Collection Code 57385), c) pH_{PZC} determination of MHO using pH drift method, d) Nitrogen gas adsorption isotherm used to determine BET surface area.

PFOA Adsorption Kinetics

Previous studies have indicated that PFOA adsorption on metal oxide surfaces is enhanced in acidic pH.⁴³ Therefore, the adsorption of PFOA on MHO was initially studied in an acidic pH of 2.3 to observe the rate of the reaction and kinetics of adsorption. Adsorption experiments over a 12 hour period (**Figure 4.3a**) shows that the adsorption was very rapid in the first two hours, corresponding to the initial transfer of the PFOA onto the surface of MHO ceramic, followed by a relatively slower diffusion of the PFOA into the mesopores of MHO.⁴⁴ **Figure 4.3b** illustrates this two-step adsorption behavior of PFOA onto the different MHO surface sites. **Figure 4.3c** shows the reduction of the integrated area of the terminal CF_3 peak ¹⁹F

nuclear magnetic resonance (NMR) signal, as expected the largest change in area is observed in the first two hours of adsorption, followed by a visibly smaller decrease in the terminal CF_3 peak area. This is consistent with the two-step adsorption model for porous solid surfaces.⁴⁵

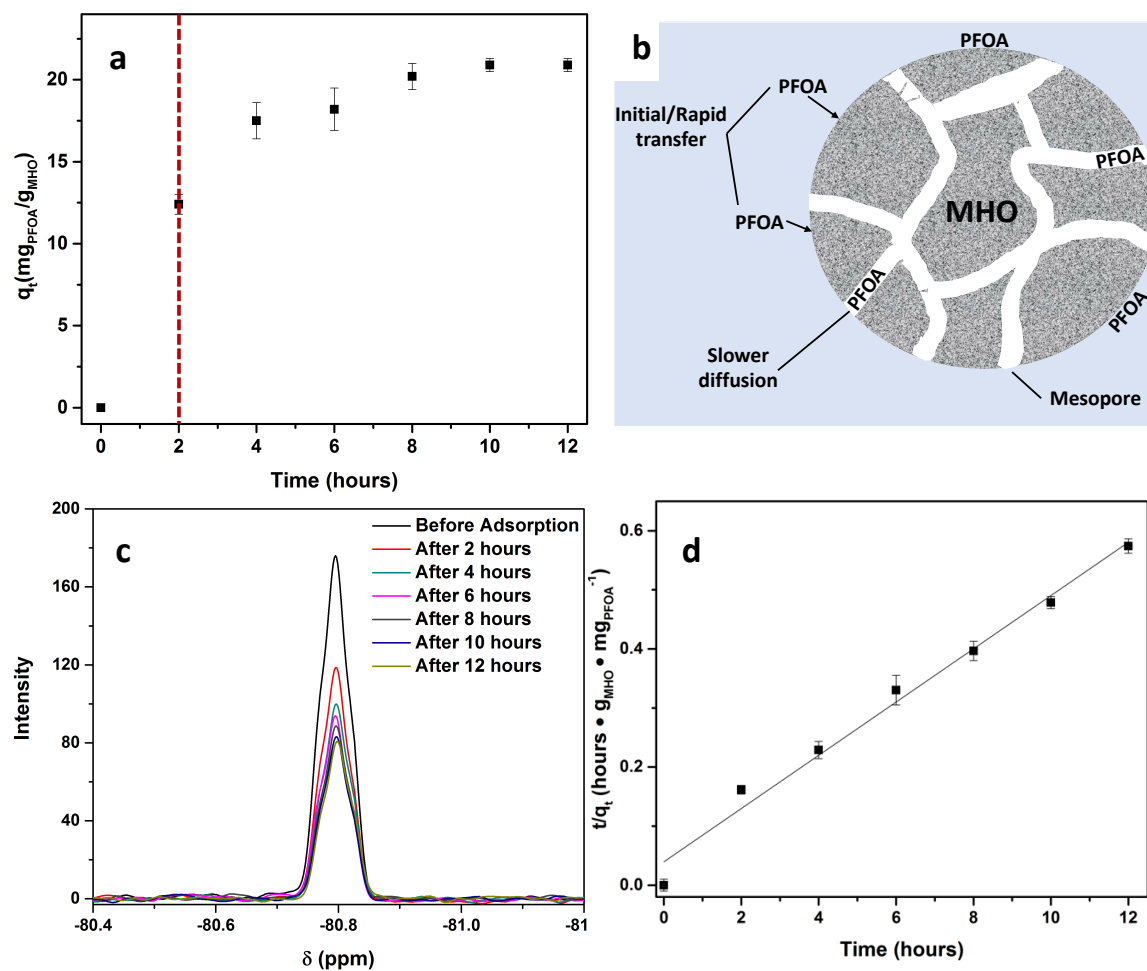


Figure 4.3 a) Rate of PFOA adsorption on MHO at pH 2.3 using 1.25 g MHO ceramic, 50 mL of 1000 ppm PFOA, over a period of 12 hours. Two-step adsorption process delineated using a red dotted line. b) Adsorption behavior of PFOA on MHO ceramic illustrating the rapid transfer of PFOA from solution to surface of MHO as well as slower diffusion of PFOA into the mesopores of MHO. c) Decrease in area of the terminal CF_3 peak in ^{19}F NMR of PFOA during adsorption on MHO. d) Pseudo-second-order model fit of the adsorption of PFOA on MHO.

A detailed ^{19}F NMR Spectrum illustrating all the peaks corresponding to PFOA can be found in **Figure 4.4**. The MHO ceramic interface in water was easily accessible by PFOA, thus equilibrium was reached in ten hours and the MHO showed an adsorption capacity of 20.9 mg of PFOA/g of MHO. The rate of adsorption of PFOA on MHO ceramic from **Figure 4.3a** was fit with the pseudo-first-order model (**Figure 4.5**) and pseudo-second-order model (**Figure 4.3d**). The adsorption capacity at equilibrium (q_e), rate constants (k), and R^2 values are reported for both models in **Table 4.1**. The reaction more closely follows the pseudo-second order model.

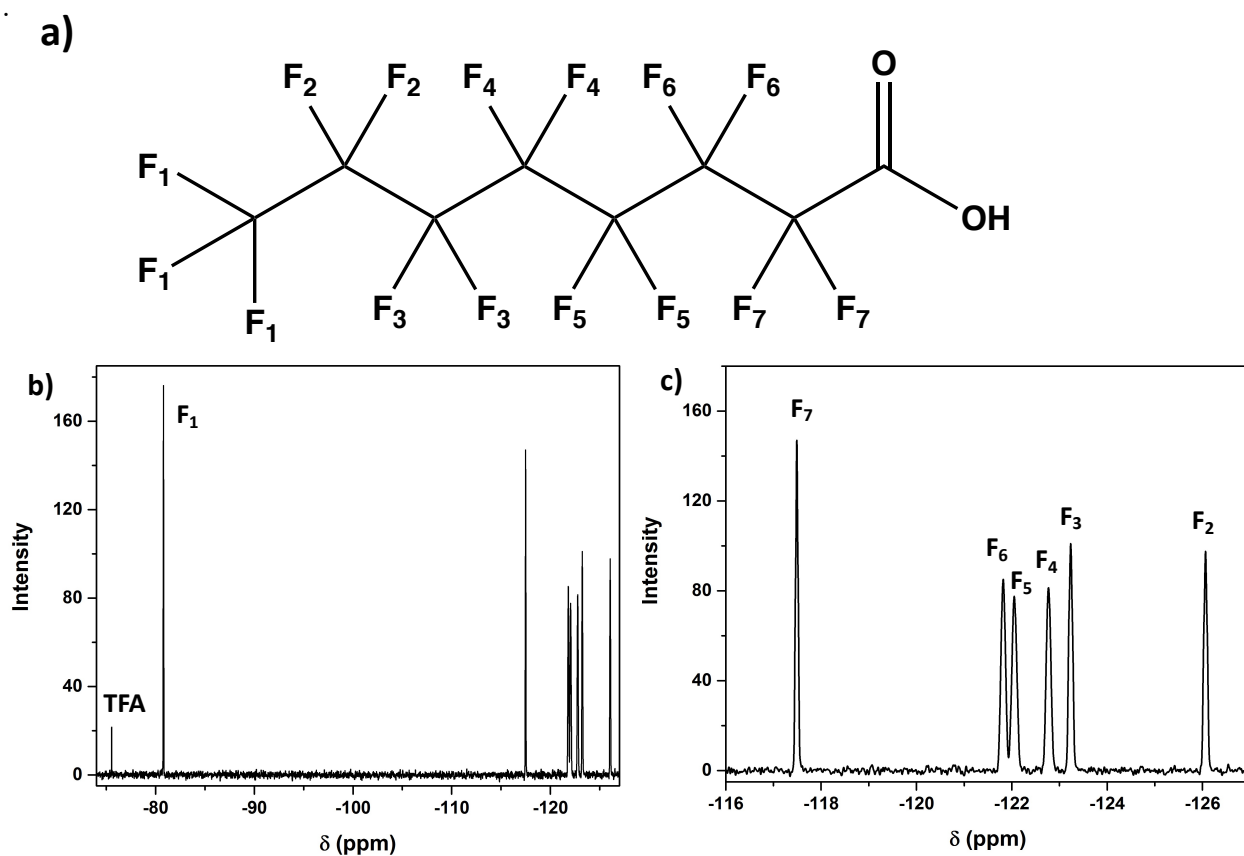


Figure 4.4 a) Structure of PFOA with different types of Fluorine numbered, b) ^{19}F NMR spectrum of PFOA with TFA (internal standard) with F_1 labelled, c) ^{19}F NMR spectrum with F_2 - F_7 labelled.

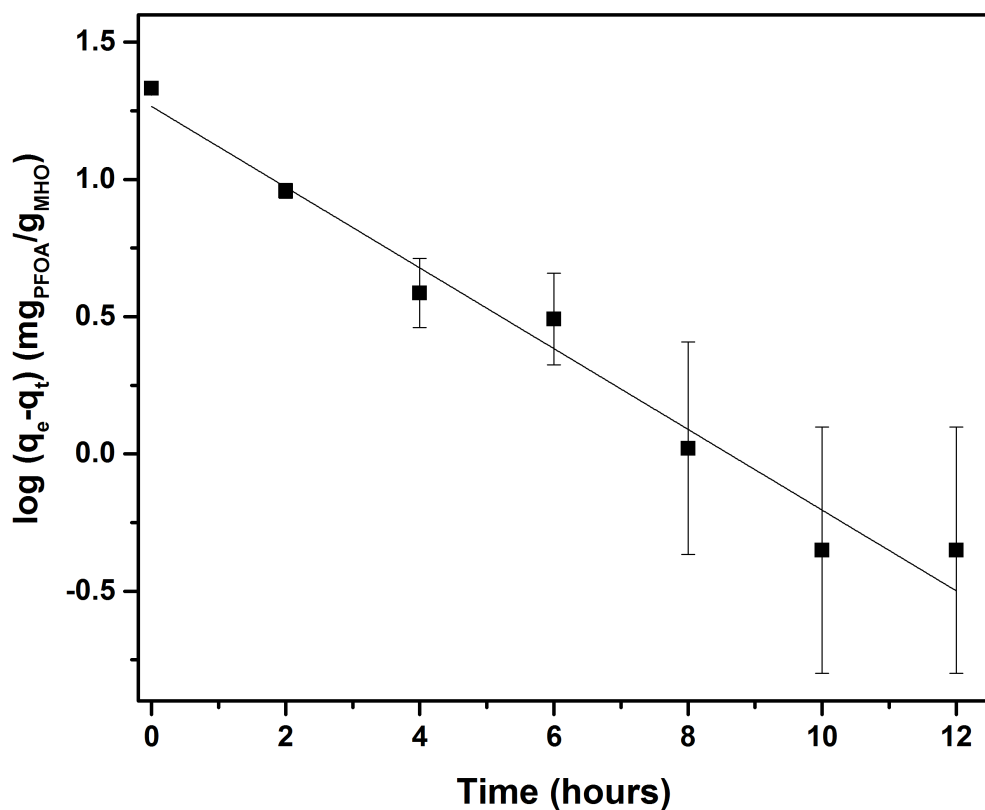


Figure 4.5 Pseudo-first-order model of adsorption of 1000 ppm PFOA on 1.25 g of MHO.

Table 4.1 Kinetic Parameters of PFOA Adsorption on MHO

Model	q_e (mg _{PFOA} /g _{MHO})	Rate Constant (k)	R^2
Pseudo-First Order	3.55 ± 0.08	$0.147 \pm 0.011 \text{ hours}^{-1}$	0.965
Pseudo-Second order	22.2 ± 1.2	0.0513 ± 0.023 g _{MHO} /mg _{PFOA} · hours	0.983

The rate of adsorption of PFOA on MHO ceramic was compared to other state-of-the-art porous materials used for PFOA adsorption and summarized in **Table 4.2**. PFOA adsorption on MHO is very efficient in comparison to GAC⁴⁶ and boehmite⁴⁷ which required 24 and 48 hours to reach equilibrium respectively. Boehmite (299.2 m²/g) specifically had a much lower adsorption capacity at 1.89 mg/g, however GAC (1100 m²/g) was more comparable at 22.7 mg/g. Commercially available multi-walled carbon nanotubes (350 m²/g) had a shorter equilibrium time (4 hours) when compared to MHO, however the adsorption capacity was also significantly lower at 12.4 mg/g.⁴⁶ Silica (650 m²/g), another group IV metal oxide, had an equilibrium time of 14 hours, and the adsorption capacity was 21.9 mg/g. However, the silica could not be regenerated after adsorption so it does limit its practicality.⁴⁸ IRA67 is an anion-exchange resin which adsorbs PFOA by ion exchange between the positively charged resin and the negatively charged head of PFOA and adsorption of the hydrophobic tail. In this case the IRA67 resin had a higher adsorption capacity than MHO at 22.2 mg/g as well as lower equilibrium time of 2 hours.⁴⁶ However, methods to regenerate spent resins have not been fully developed to date. Despite MHO having a significantly lower BET surface area than all the adsorbents mentioned earlier, the adsorption capacity of PFOA is still comparable. That is due to the fact that mesoporous particles have larger external surface area and therefore more functional groups, such as Brønsted Acid-Base sites, that are available for PFOA adsorption.⁴⁹

Table 4.2 Comparison of Our Work on PFOA Adsorption by MHO with Other State-of-the-Art Adsorbents

Material	BET Surface Area (m ² /g)	qt (mg of PFOA/g of adsorbent)	Equilibrium Time (Hours)	Reference
Swellable modified silica	650	21.2 ± 0.1	14	Stebel et al.
Boehmite	299.2 ± 1.8	1.89	48	Weng et al.
Anion-Exchange Resin (IRA67)	N/A	22.2	2	Yao et al.
Granular activated carbon	1100	22.7	24	Yao et al.
Multi-walled carbon nanotube	350	12.4	4	Yao et al.
Mesoporous hafnium oxide	10.5 ± 0.6	20.9 ± 0.4	10	This Work

PFOA Adsorption Isotherms

Experimental adsorption isotherms of PFOA on MHO ceramic were calculated with initial concentrations (200 ppm - 1000 ppm) as shown in **Figure 4.6**. The adsorption isotherms were fitted by the Langmuir model and the Freundlich model using simple linear regression. **Table 4.3** lists the isotherm constants obtained through the fitting. Based on the R² value, the Freundlich isotherm fit the data slightly better than the Langmuir isotherm. However, the Freundlich isotherm is not restricted to monolayer adsorption. The Freundlich model suggests that there are certain sites on the MHO that have an affinity for PFOA so the molecule will adsorb there first.⁵⁰

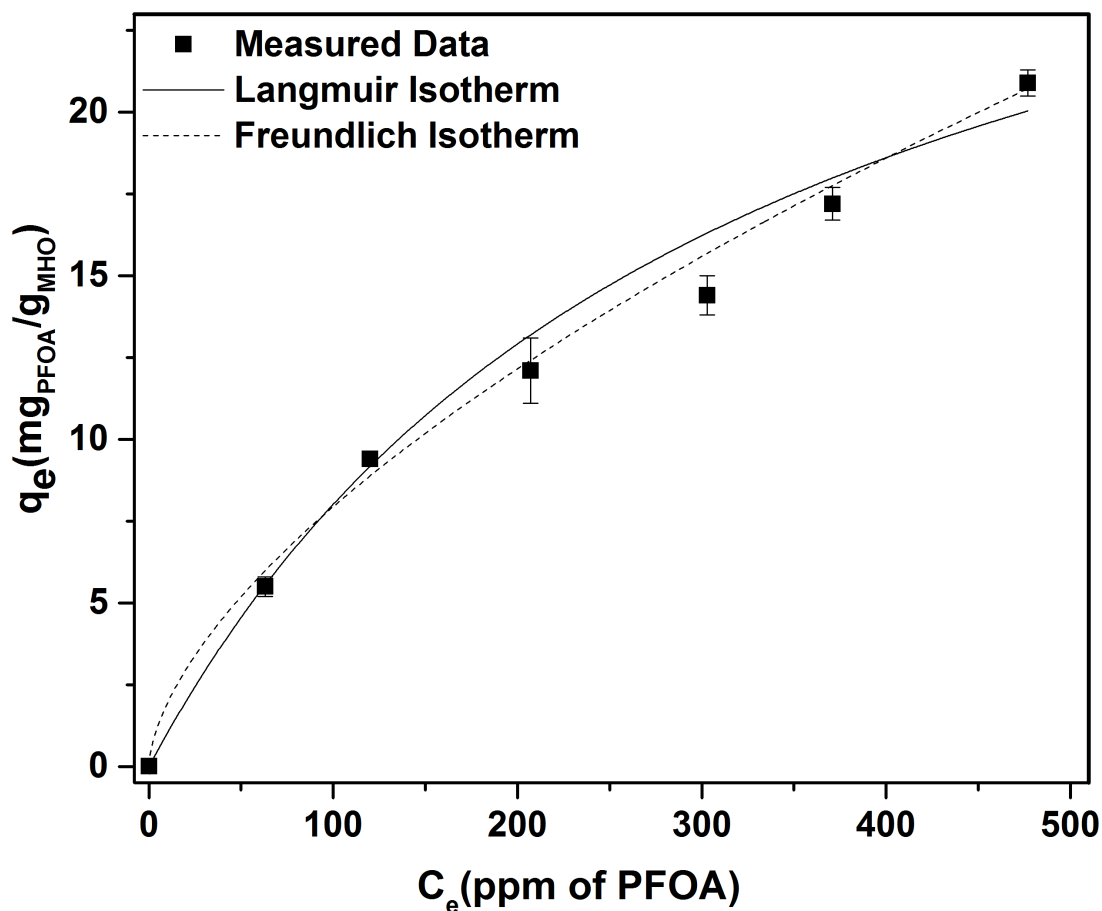


Figure 4.6 Adsorption of PFOA on MHO ceramic fitted using the Langmuir isotherm, and the Freundlich isotherm at 25°C.

Table 4.3 Constants of Langmuir and Freundlich models of PFOA Adsorption on MHO

Langmuir Constants			Freundlich Constants		
K_L (L mg ⁻¹)	q_m (mg _{PFOA} /g _{MHO})	R^2	K_F (mg g ⁻¹) (L mg ⁻¹) ^{1/n}	n	R^2
$0.00317 \pm 5.06 \times 10^{-4}$	33.3 ± 2.99	0.996	0.470 ± 0.081	1.63 ± 0.083	0.997

pH-Dependent Adsorption of PFOA

pH is an important factor in adsorption experiments due to the strong reactivity of H^+ and OH^- in solution.³⁶ Previous work using silica has shown how various metal oxide active sites affect adsorption behavior of PFOA as a function of pH.⁵¹ The effects of three different pH (2.3, 4.3, and 6.3) on the adsorption of PFOA on MHO ceramic were tested and the results are illustrated in **Figure 4.7a**. These pH values were selected in order to study the effects of adsorption on MHO when the surface is positively charged (pH 2.3), neutral (pH 4.3), and negatively charged (pH 6.3) as depicted in **Figure 4.8b**. At pH 2.3 the adsorption capacity of PFOA on MHO was 20.9 ± 0.4 mg/g. The kinetics of adsorption of PFOA on MHO at pH 2.3 followed a clear two-step adsorption model as illustrated by the curve shape of the kinetic adsorption data in **Figure 4.7a**. The first 2 hours were rapid adsorption on the surface followed by slow diffusion into the mesopores. As the pH increased the adsorption capacity decreased to 13.0 ± 0.3 mg/g and 9.12 ± 0.5 mg/g at pH 4.3 and pH 6.3, respectively. The adsorption at pH 4.3 and 6.3 did not appear to follow a curved two-step adsorption model but rather a linear adsorption onto the surface. This is due to increased repulsion between PFOA anion and negatively charged conjugate base active site on MHO. The decrease in adsorption capacity of PFOA on MHO at various pH is illustrated by the reduction of the ^{19}F NMR signal that corresponds to the terminal CF_3 peak as shown in **Figure 4.7b**.

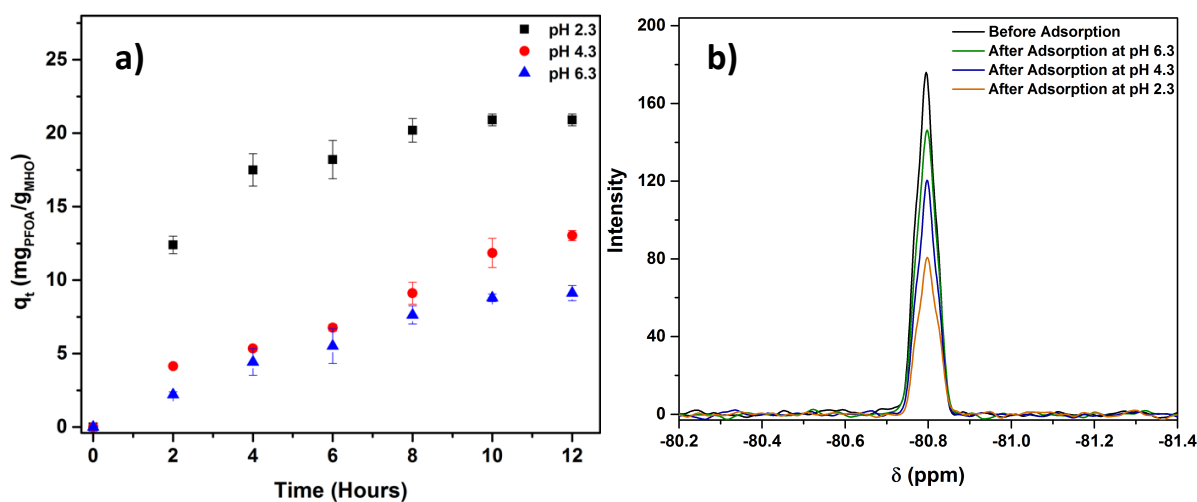


Figure 4.7 a) Rate of adsorption of PFOA on MHO at pH 2.3, 4.3, and 6, b) Decrease in area of CF_3 peak in ^{19}F NMR of PFOA during adsorption on MHO at pH 2.3, pH 4.3, and pH 6.3.

The driving forces behind the drastic change in adsorption capacity of PFOA on MHO as pH changes are illustrated in **Figure 4.8**. The pKa of PFOA is reported to be in the range of 0.5-3.8,⁵² as shown in **Figure 4.8b**. At pH 2.3, the pH < point of zero charge (PZC) of MHO (4.7), therefore the surface of the MHO is mostly positively charged with conjugate acid active sites. PFOA would be in equilibrium with the deprotonated PFOA anion at a pH of 2.3 since the pH is in the range of the pKa. This leads to coulombic attraction between the positively charged conjugate acid active site of MHO and the PFOA anion, as depicted by the green arrow in **Figure 4.8a**. There will also be some hydrophobic interaction between the hydrophobic tail of the PFOA molecule and the hydrophilic surface of MHO as depicted by the orange arrow in **Figure 4.8a**. At pH 4.3 the pH = PZC so the surface will be neutral, and the PFOA will exist mostly as the deprotonated anion since pH > pKa. Since there will be fewer positive conjugate acid active sites on the surface of MHO, there will be decreased coulombic attraction and some coulombic repulsion (**Figure 4.8a**, black arrow). Once the pH is at 6.3, the surface of the MHO is mostly negatively charged with conjugate base active sites since pH > PZC, and the PFOA will mostly exist as the deprotonated anion in solution. Both negatively charged species will lead to increased coulombic repulsion and consequently decreased PFOA adsorption.

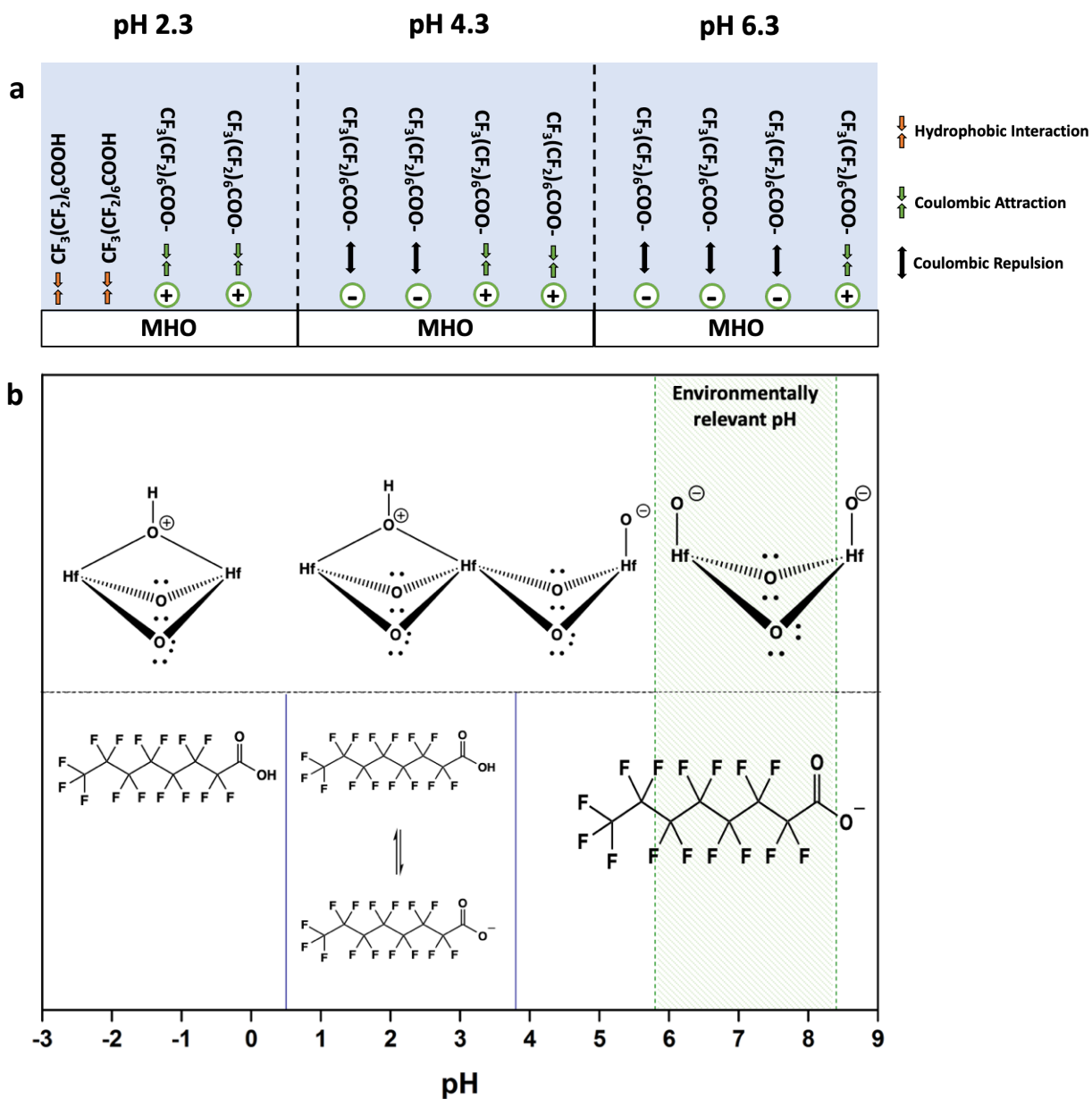


Figure 4.8 a) Illustration of PFOA adsorption on MHO at pH 2.3, 4.3, and 6.3, b) Description of MHO surface charge and PFOA charge as a function of pH. At $\text{pH} < 4.7$ MHO is positively charged with conjugate acid active sites, at $\text{pH} = 4.7$ MHO has a neutrally charged surface, and at $\text{pH} > 4.7$ MHO is negatively charged with conjugate base active sites. pK_a of PFOA is 0.5-3.8. At $\text{pH} < \text{pK}_a$ the molecule does not dissociate in solution, at $\text{pH} = \text{pK}_a$ the molecule is in equilibrium with the deprotonated anion, and $\text{pH} > \text{pK}_a$ the PFOA exists mostly as the deprotonated anion in solution.

Analysis of MHO Solid After Adsorption of PFOA

Adsorption of PFOA on the solid MHO under different pH conditions was characterized using Fourier transform infrared (FTIR) spectroscopy. The resulting FTIR in **Figure 4.9** reveals spectroscopic bands corresponding to PFOA, and shows that PFOA is adsorbed by the MHO ceramic. **Figure 4.9a** shows the spectrum between 1450-1800 cm^{-1} . The purple line represents pure solid PFOA, which is a perfluoro carboxylic acid that contains a carboxylate group (COOH) shown by the peak at 1750 cm^{-1} . All the solid MHO samples after adsorption have a peak at 1640 cm^{-1} which represents the deprotonated carboxylate group (COO⁻).⁵³ As the pH of adsorption increases, the intensity of the peak at 1640 cm^{-1} increases. This corresponds to the fact that PFOA has a low pKa (3.8) therefore as the pH increases the amount of COO⁻ in solution also increases. This suggests that coulombic attractions between the PFOA anion and the positively charged conjugate acid active site on the MHO are the driving force of the adsorption. **Figure 4.9b** shows the spectrum from 950-1450 cm^{-1} which is the range in which C-F bonds are typically observed. Peak 1 at 1050 cm^{-1} denotes the C-C bond in the PFOA chain, peak 2 at 1149 cm^{-1} represents the symmetric CF₂ stretch, peak 3 at 1200 cm^{-1} represents the asymmetric stretching of CF₂ and CF₃, and peak 4 at 1240 cm^{-1} is an asymmetric CF₂ stretch.⁵⁴ As the pH of adsorption increases, the intensity of the C-F peaks on MHO ceramic decreases. As the pH increases there are fewer positively charged conjugate acid active sites on the surface of MHO, hence more repulsion between negatively charged conjugate base active site on MHO and PFOA anion. Because of the increased coulombic repulsion, it is harder for the PFOA to travel into the mesopores of MHO ceramic.

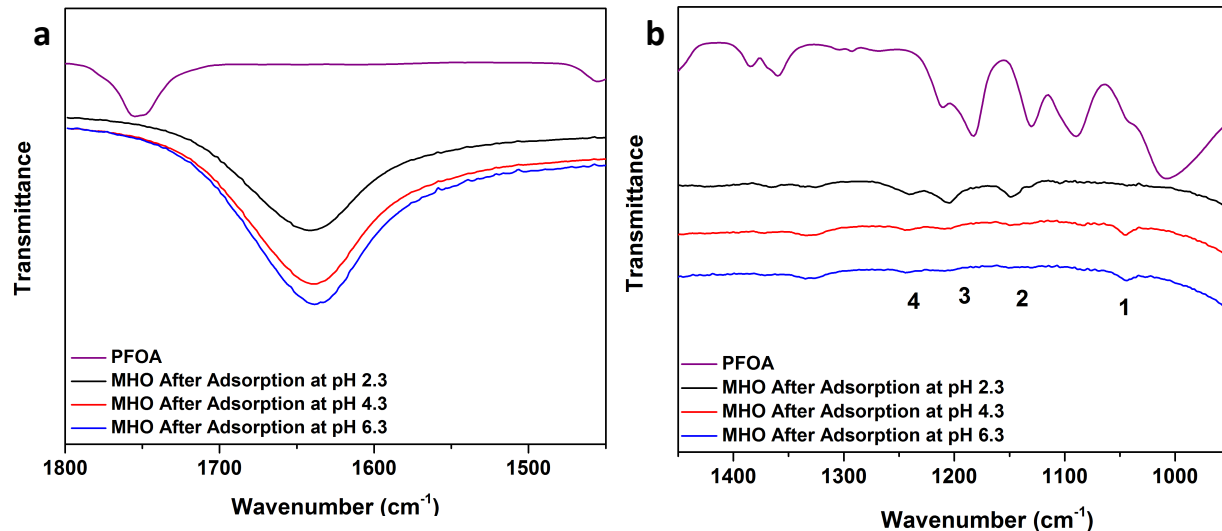


Figure 4.9 FTIR of MHO ceramic after PFOA adsorption at pH 2.3, pH 4.3, and pH 6.3 in the range of a) 1450-1800 cm^{-1} , b) 950-1450 cm^{-1} .

Regeneration of MHO Ceramic After Adsorption

The reusability of adsorbents used to remove PFOA is imperative for mitigating waste production and cleanup costs. Inadequate disposal techniques may lead to PFOA leaching back into the aquatic cycle. Thermal regeneration of PFOA contaminated adsorbents may provide an opportunity to utilize existing regeneration framework to mineralize the adsorbed PFOA, and recover the spent adsorbent.⁵⁵ Materials such as GAC⁵⁶ and multi-walled carbon nanotubes⁵⁷ have been regenerated by calcination. After adsorption, the MHO was calcined at 500°C for twenty minutes. This is relatively safer than using harsh and toxic chemicals to clean the material, as it does not produce excess toxic liquid waste. To compare the thermal stability and regeneration of MHO ceramic we performed TGA experiments after PFOA adsorption. The MHO ceramic was heated to 750 °C under high purity argon flow. The results of the TGA are shown in **Figure 4.10**. The mass loss observed from heating the bare MHO ceramic before adsorption was very minimal at 0.16% which is due to the evaporation of water from the hydrophilic surface. After PFOA adsorption we see a mass loss of 1.01% which corresponds to the PFOA and some water evaporating from the MHO ceramic.

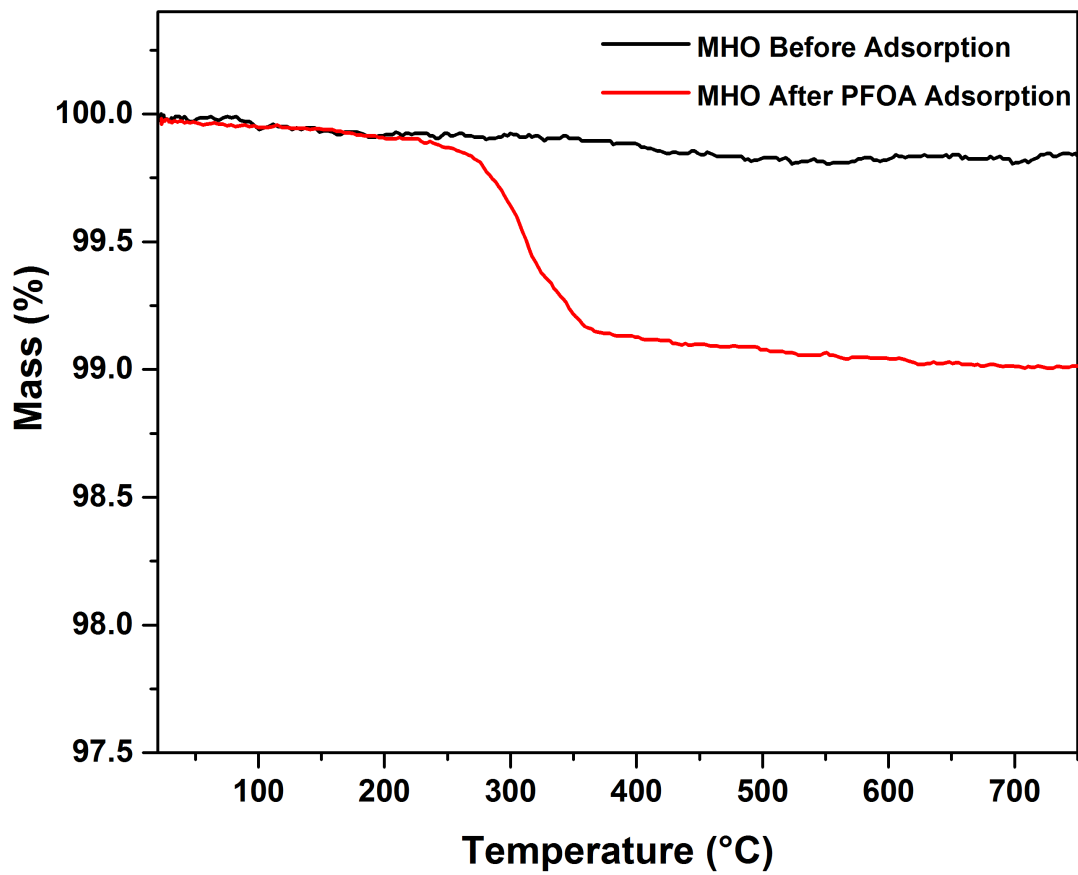


Figure 4.10 TGA of MHO ceramic before adsorption (black) and after PFOA adsorption at pH 2.3 (red) under argon.

To confirm the removal of PFOA from the MHO, the surface was analyzed using FTIR spectroscopy. The resulting spectrum is shown in **Figure 4.11**. The entire spectrum from 650 cm^{-1} to 4000 cm^{-1} is shown in **Figure 4.11a**. It overlays the spectra of the PFOA standard, MHO before adsorption, MHO after adsorption in pH 2.3, and MHO after calcination. For MHO before adsorption, the peaks between $650\text{--}800\text{ cm}^{-1}$ correspond to monoclinic Hf-O and Hf-O₂. The low intensity peaks in the range of $1200\text{--}1600\text{ cm}^{-1}$ correspond to the carboxylate (COO⁻) ligand vibrations originating from the hydrolysis of N-methyl formamide during the sol-gel synthesis. The peak at 2390 cm^{-1} represents the CO₂ that is alpha-coordinated to the Lewis acid sites on the surface.⁴¹ The intensity of the COO⁻ peak on the MHO after adsorption was clearly visible, however the C-F peaks were very low in intensity, therefore **Figure 4.11b** shows the FTIR spectrum in the range of $950\text{--}1800\text{ cm}^{-1}$ for clarity. From **Figure 4.11b**, the peaks from $1000\text{--}1400\text{ cm}^{-1}$ confirm the presence of PFOA on MHO after adsorption. After calcination, the surface of the MHO has no peaks corresponding to PFOA in the range of $950\text{--}1800\text{ cm}^{-1}$. The MHO powders were also analyzed using XRD and ESEM after calcination to ensure that the crystal structure and morphology of the MHO also remained the same as before adsorption. The XRD shown in **Figure 4.12a** illustrates that the crystal structure remains monoclinic after heating. The ESEM in **Figure 4.12b** shows similar particles with mesopores as it did prior to calcination. The FTIR spectra of MHO after calcination confirms that PFOA was completely removed and that the MHO was regenerated.

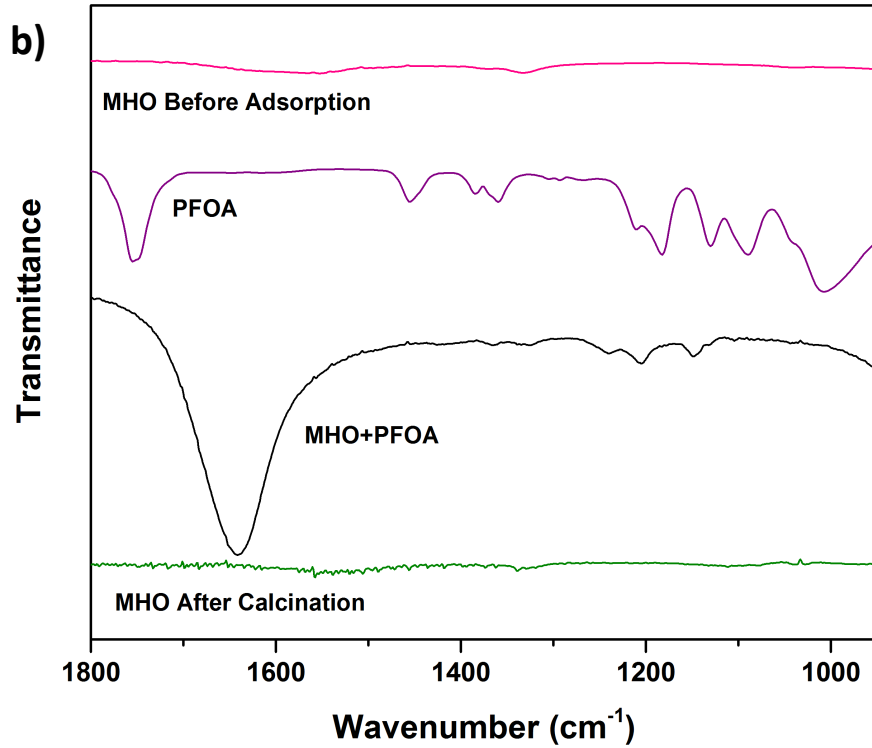
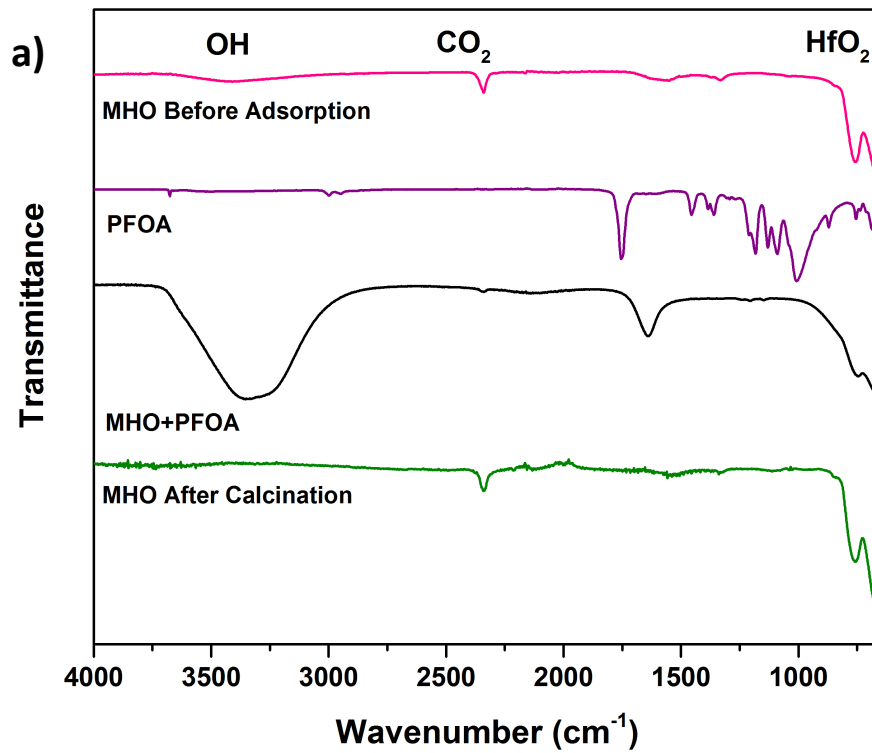


Figure 4.11 FTIR spectra of MHO before adsorption, PFOA standard, MHO after adsorption of PFOA, and MHO after calcination at 500°C from a) 650-4000 cm⁻¹, b) 950-1800 cm⁻¹.

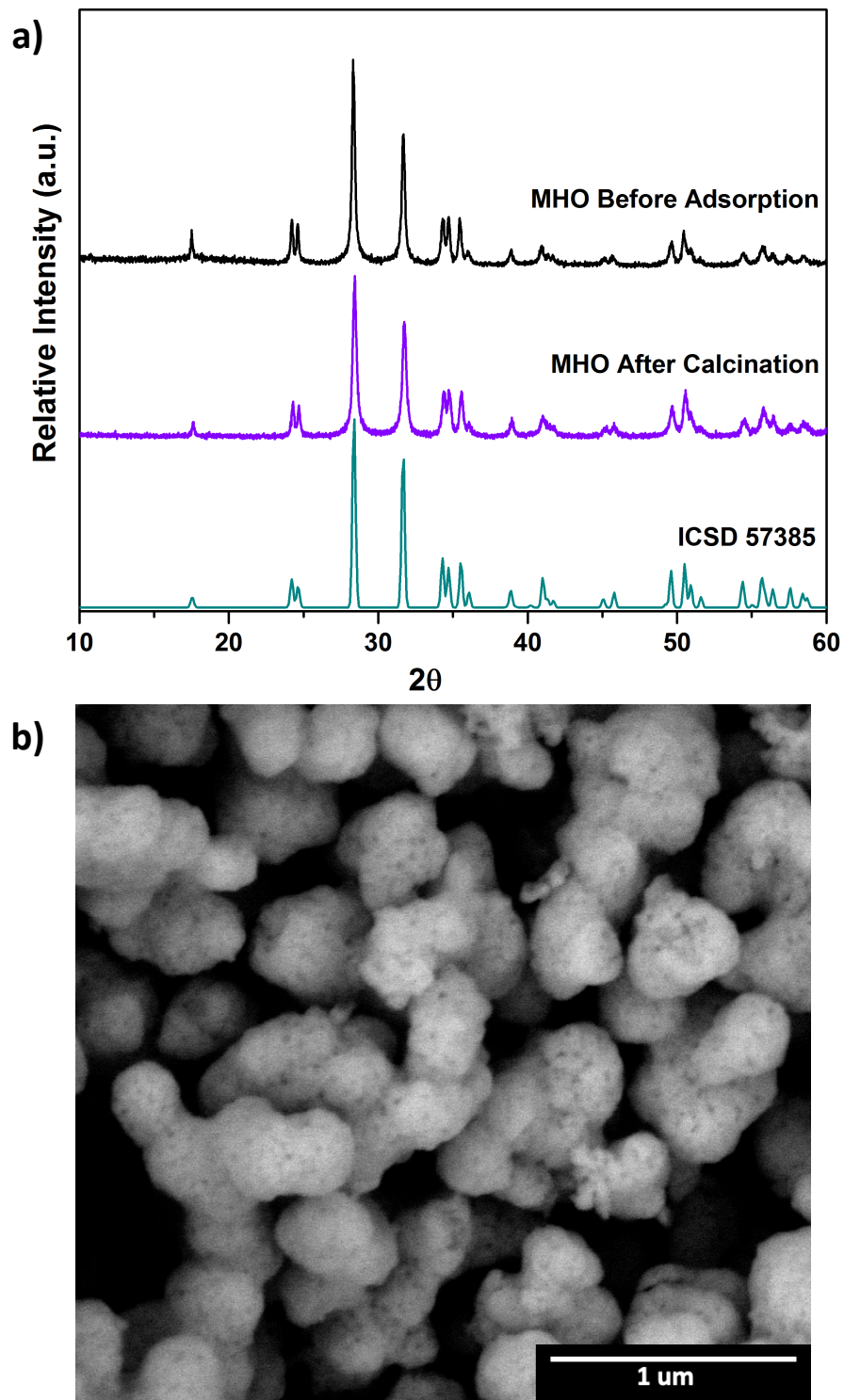


Figure 4.12 a) XRD of MHO before adsorption (black), after calcination (purple), and from Inorganic Crystal Structure Database, b) SEM image of MHO after calcination showing similar mesoporous morphology as MHO before adsorption.

Conclusions

This work demonstrated the ability of MHO to adsorb PFOA from water despite its relatively low BET surface area. The adsorption capacity of PFOA on MHO was 20.9 ± 0.4 mg/g at pH 2.3 with an equilibrium time of 10 hours. As the pH increased the adsorption capacity of MHO decreased. This is because increasing pH produces more negatively charged conjugate base active sites on the surface of MHO and more PFOA anion in solution. There will be coulombic repulsion between the adsorbent and the PFOA anion. However, at pH 2.3, the surface of MHO is positively charged with conjugate acid active sites so there will be coulombic attraction between the surface and the PFOA anion. The solid MHO could be easily regenerated after adsorption via calcination which reduces the amount of toxic solid waste that requires disposal after usage. The morphology, crystal structure, and surface functional groups remained the same before and after calcination.

The adsorption capacity of PFOA on MHO was low at environmentally relevant pH, therefore future studies would include developing methods to improve PFOA adsorption at environmentally relevant pH (5.8-8.4). This could be achieved by chemically functionalizing the surface with fluorophilic molecules that increase the adsorption capacity even at environmentally relevant pH. Given that the MHO can be regenerated after adsorption, it is important to study the endurance of MHO as an adsorbent by analyzing the adsorption capacity after each adsorption and calcination cycle. While thermal regeneration of adsorbents does not produce any excess toxic liquid waste, the PFOA does degrade to volatile PFAS molecules such as perfluoroheptene, C_2F_5 , and C_2F_4 which are released in gaseous form and contaminate the air.³² Thermal regeneration is also a very energy-intensive process which is not economically feasible so future studies will investigate less energy intensive regeneration methods that do not produce any toxic waste such as treating the spent adsorbents with ultra-violet (UV) radiation to degrade PFOA to Fluoride ions.⁵⁸

Acknowledgements

We would like to acknowledge the California Department of Resources, Recycling, and Recovery (CalRecycle) award number DRR18040 for funding this project, University of California Davis for startup funding for this project, NSF-MRI grant DMR-1725618 for the use of the Thermofisher Quattro environmental scanning electron microscope at the Advanced Materials Characterization and Testing Laboratory (AMCAT) at UC Davis. We would like to thank Ashlee Hauble from the Kauzlarich Lab at UC Davis for assistance with TGA measurements. We would like to acknowledge support from the Cottrell Scholar program supported by the Research Corporation for Science Advancement (RCSA 26780) as well as the National Science Foundation Faculty Early Career Development program (DMR-2044403).

References

- 1 K. Sini, D. Bourgeois, M. Idouhar, M. Carboni and D. Meyer, Metal–Organic Framework Sorbents For The Removal Of Perfluorinated Compounds In An Aqueous Environment, *New J. Chem.*, 2018, **42**, 17889–17894.
- 2 E. M. Sunderland, X. C. Hu, C. Dassuncao, A. K. Tokranov, C. C. Wagner and J. G. Allen, A Review Of The Pathways Of Human Exposure To Poly- And Perfluoroalkyl Substances (PFASs) And Present Understanding Of Health Effects, *J. Expo. Sci. Environ. Epidemiol.*, 2019, **29**, 131–147.
- 3 G. Zheng and A. Salamova, Are Melamine And Its Derivatives The Alternatives For Per- And Polyfluoroalkyl Substance (PFAS) Fabric Treatments In Infant Clothes?, *Environ. Sci. Technol.*, 2020, **54**, 10207–10216.
- 4 N. Seltenrich, PFAS In Food Packaging: A Hot, Greasy Exposure, *Environ. Health Perspect.*, 2020, **128**, 054002.
- 5 I. Zabaleta, N. Negreira, E. Bizkarguenaga, A. Prieto, A. Covaci and O. Zuloaga, Screening And Identification Of Per- And Polyfluoroalkyl Substances In Microwave Popcorn Bags, *Food Chem.*,

- 2017, **230**, 497–506.
- 6 G. Glenn, R. Shogren, X. Jin, W. Orts, W. Hart-Cooper and L. Olson, Per- And Polyfluoroalkyl Substances And Their Alternatives In Paper Food Packaging, *Compr. Rev. Food Sci. Food Saf.*, 2021, 1541-4337.12726.
- 7 P. J. Hill, M. Taylor, P. Goswami and R. S. Blackburn, Substitution Of PFAS Chemistry In Outdoor Apparel And The Impact On Repellency Performance, *Chemosphere*, 2017, **181**, 500–507.
- 8 N. H. Lam, C.-R. Cho, K. Kannan and H.-S. Cho, A Nationwide Survey Of Perfluorinated Alkyl Substances In Waters, Sediment And Biota Collected From Aquatic Environment In Vietnam: Distributions And Bioconcentration Profiles, *J. Hazard. Mater.*, 2017, **323**, 116–127.
- 9 A. Cordner, V. Y. De La Rosa, L. A. Schaider, R. A. Rudel, L. Richter and P. Brown, Guideline Levels For PFOA And PFOS In Drinking Water: The Role Of Scientific Uncertainty, Risk Assessment Decisions, And Social Factors, *J. Expo. Sci. Environ. Epidemiol.*, 2019, **29**, 157–171.
- 10 X.-M. Zheng, H.-L. Liu, W. Shi, S. Wei, J. P. Giesy and H.-X. Yu, Effects Of Perfluorinated Compounds On Development Of Zebrafish Embryos, *Environ. Sci. Pollut. Res.*, 2012, **19**, 2498–2505.
- 11 M. W. Sima and P. R. Jaffé, A Critical Review Of Modeling Poly- And Perfluoroalkyl Substances (PFAS) In The Soil-Water Environment, *Sci. Total Environ.*, 2021, **757**, 143793.
- 12 S.-H. Seo, M.-H. Son, E.-S. Shin, S.-D. Choi and Y.-S. Chang, Matrix-Specific Distribution And Compositional Profiles Of Perfluoroalkyl Substances (PFASs) In Multimedia Environments, *J. Hazard. Mater.*, 2019, **364**, 19–27.
- 13 G. B. Post, P. D. Cohn and K. R. Cooper, Perfluorooctanoic Acid (PFOA), An Emerging Drinking Water Contaminant: A Critical Review Of Recent Literature, *Environ. Res.*, 2012, **116**, 93–117.

- 14 H. K. Knutsen, J. Alexander, L. Barregård, M. Bignami, B. Brüschweiler, S. Ceccatelli, B. Cottrill, M. Dinovi, L. Edler, B. Grasl-Kraupp, C. Hogstrand, L. (Ron) Hoogenboom, C. S. Nebbia, I. P. Oswald, A. Petersen, M. Rose, A. Roudot, C. Vleminckx, G. Vollmer, H. Wallace, L. Bodin, J. Cravedi, T. I. Halldorsson, L. S. Haug, N. Johansson, H. van Loveren, P. Gergelova, K. Mackay, S. Levorato, M. van Manen and T. Schwerdtle, Risk To Human Health Related To The Presence Of Perfluorooctane Sulfonic Acid And Perfluorooctanoic Acid In Food, *EFSA J.*, , DOI:10.2903/j.efsa.2018.5194.
- 15 F. Guo, Y. Zhong, Y. Wang, J. Li, J. Zhang, J. Liu, Y. Zhao and Y. Wu, Perfluorinated Compounds In Human Blood Around Bohai Sea, China, *Chemosphere*, 2011, **85**, 156–162.
- 16 B. Göckener, T. Weber, H. Rüdell, M. Bücking and M. Kolossa-Gehring, Human Biomonitoring Of Per- And Polyfluoroalkyl Substances In German Blood Plasma Samples From 1982 To 2019, *Environ. Int.*, 2020, **145**, 106123.
- 17 F. Coperchini, L. Croce, G. Ricci, F. Magri, M. Rotondi, M. Imbriani and L. Chiovato, Thyroid Disrupting Effects Of Old And New Generation PFAS, *Front. Endocrinol. (Lausanne)*, , DOI:10.3389/fendo.2020.612320.
- 18 B. Panikkar, B. Lemmond, L. Allen, C. DiPirro and S. Kasper, Making The Invisible Visible: Results Of A Community-Led Health Survey Following PFAS Contamination Of Drinking Water In Merrimack, New Hampshire, *Environ. Heal.*, 2019, **18**, 79.
- 19 M. P. Velez, T. E. Arbuckle and W. D. Fraser, Maternal Exposure To Perfluorinated Chemicals And Reduced Fecundity: The MIREC Study, *Hum. Reprod.*, 2015, **30**, 701–709.
- 20 J. J. Shearer, C. L. Callahan, A. M. Calafat, W.-Y. Huang, R. R. Jones, V. S. Sabbisetti, N. D. Freedman, J. N. Sampson, D. T. Silverman, M. P. Purdue and J. N. Hofmann, Serum Concentrations Of Per- And Polyfluoroalkyl Substances And Risk Of Renal Cell Carcinoma, *JNCI J. Natl. Cancer Inst.*, 2021, **113**, 580–587.

- 21 S. M. Bartell and V. M. Vieira, Critical Review On PFOA, Kidney Cancer, And Testicular Cancer, *J. Air Waste Manage. Assoc.*, 2021, 10962247.2021.1909668.
- 22 C. Patterson, J. Burkhardt, D. Schupp, E. R. Krishnan, S. Dymont, S. Merritt, L. Zintek and D. Kleinmaier, Effectiveness Of Point-of-use/Point-of-entry Systems To Remove Per- And Polyfluoroalkyl Substances From Drinking Water, *AWWA Water Sci.*, 2019, **1**, e1131.
- 23 Q. Ma, L. Liu, W. Cui, R. Li, T. Song and Z. Cui, Electrochemical Degradation Of Perfluorooctanoic Acid (PFOA) By Yb-Doped Ti/SnO₂-Sb/PbO₂ Anodes And Determination Of The Optimal Conditions, *RSC Adv.*, 2015, **5**, 84856–84864.
- 24 Y. Wang and P. Zhang, Enhanced Photochemical Decomposition Of Environmentally Persistent Perfluorooctanoate By Coexisting Ferric Ion And Oxalate, *Environ. Sci. Pollut. Res.*, 2016, **23**, 9660–9668.
- 25 T. F. Mastropietro, R. Bruno, E. Pardo and D. Armentano, Reverse Osmosis And Nanofiltration Membranes For Highly Efficient PFASs Removal: Overview, Challenges And Future Perspectives, *Dalt. Trans.*, 2021, **50**, 5398–5410.
- 26 C. Coyle, R. Ghosh, A. Leeson and T. Thompson, US Department Of Defense–Funded Research On Treatment Of Per- And Polyfluoroalkyl Substance–Laden Materials, *Environ. Toxicol. Chem.*, 2021, **40**, 44–56.
- 27 C. Y. Tang, Q. S. Fu, C. S. Criddle and J. O. Leckie, Effect Of Flux (Transmembrane Pressure) And Membrane Properties On Fouling And Rejection Of Reverse Osmosis And Nanofiltration Membranes Treating Perfluorooctane Sulfonate Containing Wastewater, *Environ. Sci. Technol.*, 2007, **41**, 2008–2014.
- 28 M. Trojanowicz, A. Bojanowska-Czajka, I. Bartosiewicz and K. Kulisa, Advanced Oxidation/Reduction Processes Treatment For Aqueous Perfluorooctanoate (PFOA) And

- Perfluorooctanesulfonate (PFOS) – A Review Of Recent Advances, *Chem. Eng. J.*, 2018, **336**, 170–199.
- 29 L. Liu, Y. Liu, B. Gao, R. Ji, C. Li and S. Wang, Removal Of Perfluorooctanoic Acid (PFOA) And Perfluorooctane Sulfonate (PFOS) From Water By Carbonaceous Nanomaterials: A Review, *Crit. Rev. Environ. Sci. Technol.*, 2020, **50**, 2379–2414.
- 30 J. Xu, Z. Liu, D. Zhao, N. Gao and X. Fu, Enhanced Adsorption Of Perfluorooctanoic Acid (PFOA) From Water By Granular Activated Carbon Supported Magnetite Nanoparticles, *Sci. Total Environ.*, 2020, **723**, 137757.
- 31 Q. Yu, R. Zhang, S. Deng, J. Huang and G. Yu, Sorption Of Perfluorooctane Sulfonate And Perfluorooctanoate On Activated Carbons And Resin: Kinetic And Isotherm Study, *Water Res.*, 2009, **43**, 1150–1158.
- 32 F. Xiao, P. C. Sasi, B. Yao, A. Kubátová, S. A. Golovko, M. Y. Golovko and D. Soli, Thermal Stability And Decomposition Of Perfluoroalkyl Substances On Spent Granular Activated Carbon, *Environ. Sci. Technol. Lett.*, 2020, **7**, 343–350.
- 33 J. E. Park, G. B. Lee, B. U. Hong and S. Y. Hwang, Regeneration Of Activated Carbons Spent By Waste Water Treatment Using KOH Chemical Activation, *Appl. Sci.*, 2019, **9**, 5132.
- 34 D. P. Siriwardena, R. James, K. Dasu, J. Thorn, R. D. Iery, F. Pala, D. Schumitz, S. Eastwood and N. Burkitt, Regeneration Of Per- And Polyfluoroalkyl Substance-Laden Granular Activated Carbon Using A Solvent Based Technology, *J. Environ. Manage.*, 2021, **289**, 112439.
- 35 F. Dixit, B. Barbeau, S. G. Mostafavi and M. Mohseni, PFOA And PFOS Removal By Ion Exchange For Water Reuse And Drinking Applications: Role Of Organic Matter Characteristics, *Environ. Sci. Water Res. Technol.*, 2019, **5**, 1782–1795.
- 36 F. Wang and K. Shih, Adsorption Of Perfluorooctanesulfonate (PFOS) And Perfluorooctanoate

- (PFOA) On Alumina: Influence Of Solution PH And Cations, *Water Res.*, 2011, **45**, 2925–2930.
- 37 S. Deng, Y. Q. Zheng, F. J. Xu, B. Wang, J. Huang and G. Yu, Highly Efficient Sorption Of Perfluorooctane Sulfonate And Perfluorooctanoate On A Quaternized Cotton Prepared By Atom Transfer Radical Polymerization, *Chem. Eng. J.*, 2012, **193–194**, 154–160.
- 38 A. V. Alves, M. Tsianou and P. Alexandridis, Fluorinated Surfactant Adsorption On Mineral Surfaces: Implications For PFAS Fate And Transport In The Environment, *Surfaces*, 2020, **3**, 516–566.
- 39 L. Zhao, H. Qin, R. Wu and H. Zou, Recent Advances Of Mesoporous Materials In Sample Preparation, *J. Chromatogr. A*, 2012, **1228**, 193–204.
- 40 J. Nawrocki, M. Rigney, A. McCormick and P. Carr, Chemistry Of Zirconia And Its Use In Chromatography, *J. Chromatogr. A*, 1993, **657**, 229–282.
- 41 F. A. Hussain, J. Zamora, I. M. Ferrer, M. Kinyua and J. M. Velázquez, Adsorption Of Crude Oil From Crude Oil–Water Emulsion By Mesoporous Hafnium Oxide Ceramics, *Environ. Sci. Water Res. Technol.*, , DOI:10.1039/D0EW00451K.
- 42 A. Xie, J. Dai, X. Chen, J. He, Z. Chang, Y. Yan and C. Li, Hierarchical Porous Carbon Materials Derived From A Waste Paper Towel With Ultrafast And Ultrahigh Performance For Adsorption Of Tetracycline, *RSC Adv.*, 2016, **6**, 72985–72998.
- 43 H. Campos-Pereira, D. B. Kleja, C. Sjöstedt, L. Ahrens, W. Klysubun and J. P. Gustafsson, The Adsorption Of Per- And Polyfluoroalkyl Substances (PFASs) Onto Ferrihydrite Is Governed By Surface Charge, *Environ. Sci. Technol.*, 2020, **54**, 15722–15730.
- 44 M. L. Brusseau, Simulating PFAS Transport Influenced By Rate-Limited Multi-Process Retention, *Water Res.*, 2020, **168**, 115179.
- 45 L. J. Kennedy, J. J. Vijaya, K. Kayalvizhi and G. Sekaran, Adsorption Of Phenol From Aqueous

- Solutions Using Mesoporous Carbon Prepared By Two-Stage Process, *Chem. Eng. J.*, 2007, **132**, 279–287.
- 46 Y. Yao, K. Volchek, C. E. Brown, A. Robinson and T. Obal, Comparative Study On Adsorption Of Perfluorooctane Sulfonate (PFOS) And Perfluorooctanoate (PFOA) By Different Adsorbents In Water, *Water Sci. Technol.*, 2014, **70**, 1983–1991.
- 47 F. Wang, C. Liu and K. Shih, Adsorption Behavior Of Perfluorooctanesulfonate (PFOS) And Perfluorooctanoate (PFOA) On Boehmite, *Chemosphere*, 2012, **89**, 1009–1014.
- 48 E. K. Stebel, K. A. Pike, H. Nguyen, H. A. Hartmann, M. J. Klonowski, M. G. Lawrence, R. M. Collins, C. E. Hefner and P. L. Edmiston, Absorption Of Short-Chain To Long-Chain Perfluoroalkyl Substances Using Swellable Organically Modified Silica, *Environ. Sci. Water Res. Technol.*, 2019, **5**, 1854–1866.
- 49 A. Kuvayskaya, B. Lotsi, R. Mohseni and A. Vasiliev, Mesoporous Adsorbents For Perfluorinated Compounds, *Microporous Mesoporous Mater.*, 2020, **305**, 110374.
- 50 M. A. Al-Ghouti and D. A. Da'ana, Guidelines For The Use And Interpretation Of Adsorption Isotherm Models: A Review, *J. Hazard. Mater.*, 2020, **393**, 122383.
- 51 U. Shafique, V. Dorn, A. Paschke and G. Schüürmann, Adsorption Of Perfluorocarboxylic Acids At The Silica Surface, *Chem. Commun.*, 2017, **53**, 589–592.
- 52 D. C. Burns, D. A. Ellis, H. Li, C. J. McMurdo and E. Webster, Experimental P K A Determination For Perfluorooctanoic Acid (PFOA) And The Potential Impact Of P K A Concentration Dependence On Laboratory-Measured Partitioning Phenomena And Environmental Modeling, *Environ. Sci. Technol.*, 2008, **42**, 9283–9288.
- 53 W. Chen, X. Zhang, M. Mamadiev and Z. Wang, Sorption Of Perfluorooctane Sulfonate And Perfluorooctanoate On Polyacrylonitrile Fiber-Derived Activated Carbon Fibers: In Comparison

- With Activated Carbon, *RSC Adv.*, 2017, **7**, 927–938.
- 54 X. Gao and J. Chorover, Adsorption Of Perfluorooctanoic Acid And Perfluorooctanesulfonic Acid To Iron Oxide Surfaces As Studied By Flow-Through ATR-FTIR Spectroscopy, *Environ. Chem.*, 2012, **9**, 148.
- 55 B. Sonmez Baghirzade, Y. Zhang, J. F. Reuther, N. B. Saleh, A. K. Venkatesan and O. G. Apul, Thermal Regeneration Of Spent Granular Activated Carbon Presents An Opportunity To Break The Forever PFAS Cycle, *Environ. Sci. Technol.*, 2021, **55**, 5608–5619.
- 56 N. Watanabe, M. Takata, S. Takemine and K. Yamamoto, Thermal Mineralization Behavior Of PFOA, PFHxA, And PFOS During Reactivation Of Granular Activated Carbon (GAC) In Nitrogen Atmosphere, *Environ. Sci. Pollut. Res.*, 2018, **25**, 7200–7205.
- 57 F. Cao, L. Wang, Y. Yao, F. Wu, H. Sun and S. Lu, Synthesis And Application Of A Highly Selective Molecularly Imprinted Adsorbent Based On Multi-Walled Carbon Nanotubes For Selective Removal Of Perfluorooctanoic Acid, *Environ. Sci. Water Res. Technol.*, 2018, **4**, 689–700.
- 58 F. Li, Z. Wei, K. He, L. Blaney, X. Cheng, T. Xu, W. Liu and D. Zhao, A Concentrate-And-Destroy Technique For Degradation Of Perfluorooctanoic Acid In Water Using A New Adsorptive Photocatalyst, *Water Res.*, 2020, **185**, 116219.

5 Chapter 5: Electrochemical Oxidation of Perfluorooctanoic Acid

Abstract

The electrochemical oxidation of the legacy perfluorooctanoic acid (PFOA) was studied using platinum mesh, nickel foil, and glassy carbon electrodes. These electrodes were selected to determine a relationship between oxygen evolution potential and PFOA degradation. Based on preliminary reactions nickel which is a better oxygen evolution reaction (OER) catalyst showed the highest degradation of PFOA at 58.7% in comparison to platinum (51.8%) and glassy carbon (33.1%). Since alkaline pH increases the rate of oxygen evolution reactions, when tested at a higher pH, complete degradation of PFOA was observed using nickel and platinum anodes. The gaseous degradation product observed was carbon dioxide, however the fluorinated degradation products are yet to be determined.

Introduction

Per- and polyfluoroalkyl substances (PFAS) are a large group of synthetic toxic chemicals found in firefighting foams, non-stick cookware, and water proof clothing.¹ These chemicals have emerged as one of the leading contaminants of concern worldwide due to their environmental persistence, and human toxicity.² As a consequence of their low volatility and solubility in water they tend to bioaccumulate in organs such as the liver and bodily fluids such as blood.³ This can lead to health issues like liver damage, immunotoxicity, and in extreme cases cancer.⁴ In particular, perfluorooctanoic acid (PFOA) the PFAS molecule with eight carbons is of the highest concern due to the fact that it is the most prevalent PFAS molecule in wastewater.⁵ PFOA was found to have a half life of 2.7 years in aquatic ecosystems.⁶ Therefore, developing remediation technologies to degrade these compounds is of the utmost importance.

While the scale down of PFAS from industrial waste would be the ideal way to eliminate PFAS from wastewater, remediation techniques are still required to treat PFAS in wastewater. Numerous remediation

techniques are used for treating PFAS contaminated wastewater such as reverse osmosis using a thin-film composite polyamide membrane,⁷ adsorption using granular activated carbon (GAC)⁸ and anion-exchange resins (AIX)⁹, as well as microbial degradation using *Acidimicrobium* bacteria from the wetlands of New Jersey.¹⁰ While reverse osmosis membranes are ideal due to their high removal capacity, modularity, and flexibility, they require extremely high pressures to operate, which results in considerable energy-costs.¹¹ In comparison, adsorption using GAC and AIX resins is facile and economically feasible due to the ease of production. However, both reverse osmosis using a thin-film composite polyamide membrane, and adsorption with GAC and IX resins results in the transfer of PFAS from water to a solid that requires further disposal. These non-destructive techniques do not degrade or destroy PFAS, rather the contaminant is just transferred from one form to another. However, microbial degradation using *Acidimicrobium* bacteria has shown the ability to destroy PFOA to fluoride ions however, the process did take 100 days. Hence, there is a need to evaluate techniques that destroy PFAS molecules in a reasonable amount of time.

Electrochemical oxidation (EO) has been widely used as a destructive technique for a range of persistent organic pollutants (POP) such as humic acid,¹² clofibrilic acid,¹³ and Rhodamine B dye.¹⁴ EO has low energy consumption, can be performed at room temperature and pressure, rapid reaction time, and high oxidation efficiency.¹⁵ Using EO the degradation of PFOA can be directly performed at the anode surface via electron transfer, or indirectly with the assistance of in situ generated hydroxyl radicals.¹⁶ The degradation proceeds via a series of defluorination reactions of the parent PFOA molecule to products such as shorter chain PFAS, hydrofluoric acid (HF), fluoride ions, and carbon dioxide (CO₂) gas.¹⁷ The rate of the reaction will depend on pH, initial PFOA concentration, and the presence of co-contaminants. Since EO is not selective and already used for destruction of POP, it provides a unique opportunity for the destruction of PFOA as well as other contaminants in wastewater within existing infrastructure. In addition, EO is less energy-intensive than thermal incineration of PFAS, and can produce commodity chemicals such as fluoride as by products.

During EO, the selection of an appropriate anode material is important as it determines the cost and efficiency of the degradation. The most commonly evaluated anode for the degradation of PFOA is boron-

doped diamond (BDD) which efficiently degrades 94% of PFOA in 5 hours,¹⁸ but is difficult to produce and costs \$7125/m².¹⁹ Therefore, using pure metal electrodes is advantageous as they are easier to fabricate and have excellent electrical properties.²⁰ The three pure metal anodes that will be evaluated herein are nickel foil, platinum mesh, and glassy carbon electrode. Nickel is a better oxygen-evolution reaction (OER) catalyst when compared to platinum and glassy carbon.²¹ The hydroxyl radicals (OH•) generated by electrolysis of water are extremely electrochemically active due to their high oxidation potential.²⁰ The OH• radicals are also essential for the stepwise degradation of PFOA molecules. These electrodes will allow us to evaluate correlation between oxygen evolution reaction and PFOA electrochemical oxidation.

The goal of this work is to compare PFOA degradation by electrochemical oxidation using platinum mesh, nickel foil, and glassy carbon as working electrodes. Platinum (Pt), nickel (Ni), and glassy carbon were selected due to their differences in oxygen-evolution potential which are 1.90V for Pt, 1.40V for Ni, and 2.30V for glassy carbon all versus Ag/AgCl reference. EO was performed using these electrodes in a three electrode setup where a constant potential is applied under argon flow and continuous stirring. The liquid aliquots are evaluated using ¹⁹F nuclear magnetic resonance (NMR) spectroscopy and fluoride ion selective electrode. The gas products are determined using gas chromatography (GC).

Materials & Methods

Chemicals & Materials

Perfluorooctanoic acid (PFOA, >98%) was purchased from TCI America. Deuterated water (D₂O), Sulfuric acid (95.0–98.0%), Sodium fluoride (>99%), Sodium sulfate (>99.0%), Graphite rod (99.995%), Nickel foil (99.98%) were used as purchased from Sigma-Aldrich. The fluoride ionic strength adjustor solution (TISAB 1) was purchased from Col-Parmer. Trifluoroacetic acid (TFA, 99.5%) was purchased from Acros Organics. Sodium hydroxide pellets (98%) and Platinum mesh (99.99%) were purchased from Alfa Aesar, Ag/AgCl reference electrode and the glassy carbon working electrode were purchased through ALS Japan.

Selemion® anion exchange membrane was purchased from AGC Engineering and stored in ultra-pure deionized water prior to use in electrochemical experiments. Ultrahigh purity grade argon gas (99.999%) was used as purchased from Praxair. Ultrapure water ($\geq 18.2 \text{ M}\Omega\cdot\text{cm}$) used for electrochemical oxidation experiments was obtained from a Thermo Scientific Barnstead E-Pure Ultrapure water purification system.

Electrochemical Analysis

All electrochemical oxidation experiments were performed using a custom sealable three electrode cell as shown in **Figure 5.1**. The counter electrode is separated from the working and reference electrode using a selemion anion-exchange membrane. The working electrodes used were as purchased nickel foil, platinum mesh, and a glassy carbon electrode, the reference electrode was Ag/AgCl, and the counter electrode was a graphite rod. The working, counter (graphite rod), and reference electrode (Ag/AgCl) were all submerged in 0.1 M sodium sulfate with 100 ppm of PFOA. pH was adjusted for the electrolyte using 0.1 M Sulfuric acid and 0.1 M sodium hydroxide. All electrochemical experiments were carried out using a Bio-Logic VSP-300 multichannel potentiostat equipped with standard EC-Lab software. The cell was purged with argon for 30 minutes to clear the headspace of air to be able to determine presence of gaseous degradation products. EO of PFOA was evaluated by performing chronoamperometry experiments under continuous stirring to ensure homogenization of the electrolyte throughout the course of the reaction, and continuous argon flow. Liquid aliquots were extracted from both the working (anode), and counter (cathode) compartments for analysis in NMR, and the headspace gases of the anode compartment were analyzed using GC.

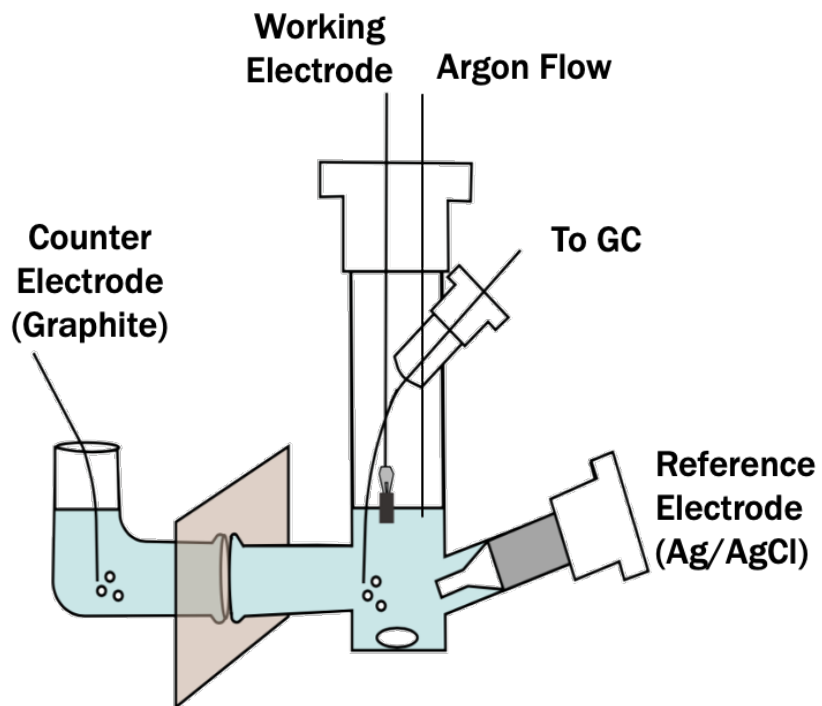


Figure 5.1 Illustration of schematic of three electrode cell setup with the counter electrode (graphite) on the left side separated by a selenion anion exchange membrane, the right side is the working compartment side with the stir bar, reference electrode of Ag/AgCl, argon gas purge needle, and needle that is connected directly to the GC.

Product Analysis

Liquid aliquots from the cell before and after electrochemical oxidation experiments were extracted and quantified using ^{19}F NMR spectroscopy in a 400 MHz Bruker NMR spectrometer. A calibration curve was created using Trifluoroacetic acid (TFA) as the internal standard and D_2O as the solvent. The concentration of PFAS was determined by integrating the area of the terminal CF_3 peak (-81 ppm) and comparing it to the area of the peak of the internal standard, trifluoroacetic acid (-76 ppm). Calibrations were performed with six standard solutions in the range of (9-2000 ppm). 200 μL of liquid was added to 400 μL of D_2O spiked with TFA in a 300 MHz Wilmad NMR tube and analysed using 128 scans. The percent removal of PFOA was calculated using the following **eq 5.1**:

$$\% \text{ PFOA Removed} = \frac{(C_0 - C)}{C_0} \times 100\% \text{ (eq. 5.1)}$$

Where C_0 is the initial concentration of PFOA in ppm, and C is the concentration of PFOA at a certain point during the EO experiment in ppm.

For the detection of gas-phase products such as CO_2 , gas chromatography with thermal conductivity detection (GC–TCD) was implemented using methods from literature²² with a Thermo-Fisher GC equipped with a Carboxen® 1010 Porous Layer Open Tubular (PLOT) fused silica column (30m x 0.53mm x 10 μm), with helium as a reference and carrier gas. Fluoride ion content was determined using a fluoride ion selective electrode (ISE) from Oakton by Cole-Parmer. The fluoride ISE was calibrated using sodium fluoride (1-1000 ppm) in acidic, neutral, and alkaline pH.

Results & Discussion

Preliminary PFOA Degradation Results

The results shown in **Figures 5.3-5.5** depict changes in concentration of PFOA during EO using platinum,

nickel, and glassy carbon anodes respectively. Platinum is the most electrochemically active electrode tested and showed 51.8% removal of PFOA on the anode side, and 69.4% on the cathode side. In this case the indirect oxidation of PFOA via hydroxyl radicals was better than direct oxidation at the anode. Whereas using nickel, a better OER catalyst than platinum we observed higher degradation of PFOA via direct oxidation at the anode (58.7%) when compared to the indirect oxidation via $\text{OH}\cdot$ (49%). Finally glassy carbon, which is not as conductive as platinum or nickel, had higher degradation of PFOA via direct oxidation at the anode (33.3%) when compared to the indirect oxidation using $\text{OH}\cdot$ (28.5%). The direct oxidation of PFOA at the anode, and indirect oxidation of PFOA using $\text{OH}\cdot$ at the cathode is shown in **Figure 5.2** below.

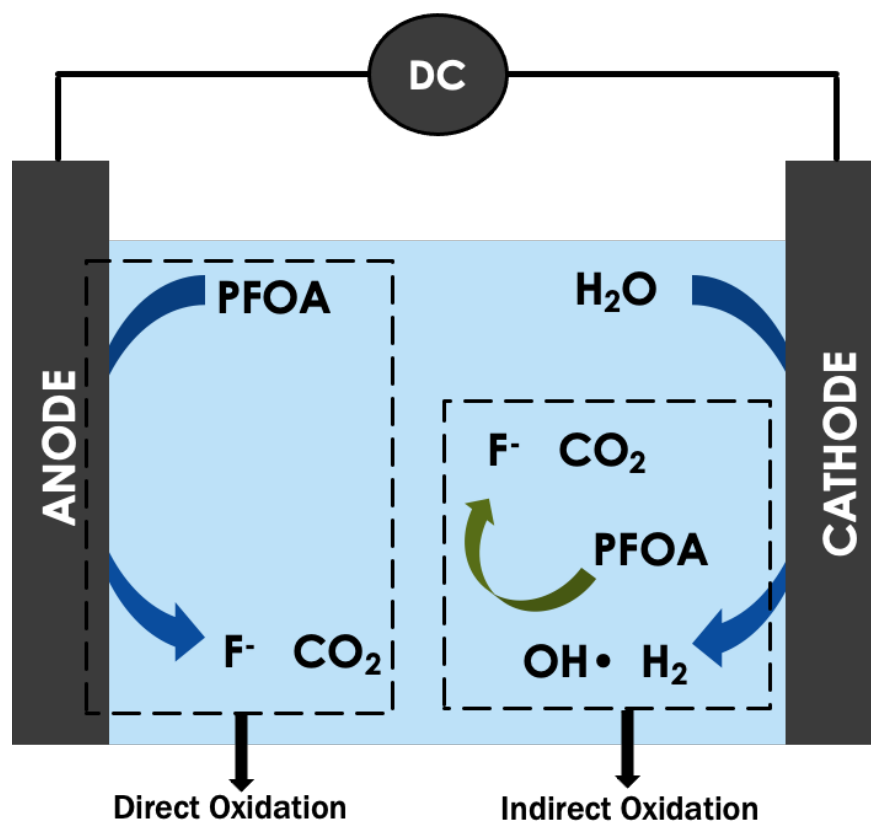


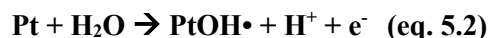
Figure 5.2 Depiction of direct oxidation of PFOA at the anode, and indirect oxidation of PFOA via $\text{OH}\cdot$ in bulk solution.

Therefore, after 21 hours, an initial concentration of 100 ppm PFOA at a pH of 4.1, the anodic oxidation was highest using nickel and lowest using glassy carbon, whereas in terms of indirect oxidation it was highest using platinum and lowest using glassy carbon as summarized in **Table 5.1**.

Table 5.1 Summary of PFOA Degraded during EO using 100 ppm of PFOA at pH 4.1 with Nickel, Platinum, and Glassy Carbon Anodes.

Catalyst	% PFOA Degraded After 21 hours at pH 4.1	
	Anode	Cathode
Nickel	58.7%	49.0%
Platinum	51.8%	69.4%
Glassy Carbon	33.3%	28.5%

The nickel foil degraded more PFOA directly at the anode in comparison with platinum because nickel is a better anode material with a lower oxidation potential. Nickel can readily oxidize to Ni²⁺ ion in solution. Such metal ions have been known to remove pollutants such as acetaminophen via hydrogen bonding.²³ Platinum is a very stable electrode which does not ionize readily in solution and is slower to degrade PFOA. Therefore, the indirect degradation via hydroxyl radicals produced is more efficient. The electrochemical activity of the anode is important as it determines whether the OH• will chemisorb or physisorb on the surface which in turn affects the degradation of PFOA. An electrochemically active anode will have OH• chemisorbed on the surface, whereas electrochemically inactive anodes will have physisorbed OH• on the surface. Physisorbed OH• will completely mineralize PFOA to CO₂ as physisorbed species are more oxidant than chemisorbed ones.²⁴ Since platinum is an electrochemically active electrode the hydroxyl radical (OH•) generated by the electrolysis of water will chemically adsorb on the surface.²⁵ This chemically adsorbed OH• radical will limit the ability of the anode for direct PFOA oxidation to CO₂ (eq. 5.2):



The largest decrease in concentration of PFOA in liquid with all three electrodes was observed in the first two hours and the largest amount of carbon dioxide produced was also in the first two hours. Considering bond energies involved the degradation of PFOA is likely to begin with the cleavage of the C-C bond (372 kJ/mol) rather than the C-F bond (531 kJ/mol), specifically the C-C bond between the CF₂ and the

carboxylic acid group (CF₂-COOH).²⁶ In the work developed by Sukeesan et al.,¹⁸ the PFOA molecule begins to degrade by donating an electron to the anode surface from the carboxylic acid group resulting in a C₇F₁₅COO• radical (eq. 5.3). The radical then decarboxylates to produce CO₂ and C₇F₁₅• radical (eq. 5.4). The C₇F₁₅• radical reacts with OH• radical to produce C₇F₁₅OH (eq. 5.5), a thermally unstable alcohol, which further defluorinates to C₆F₁₃COF and HF (eq. 5.6). Finally, hydrolysis of C₆F₁₃COF occurs resulting in C₆F₁₃COOH, a shorter PFAS molecule also known as perfluoroheptanoic acid (eq. 5.7). The reactions continue in this cycle of sequentially removing CF₂ to form shorter chain PFAS until COF₂ is formed. COF₂ degrades to CO₂ and HF in solution. This possible degradation mechanism for PFOA was observed by researchers through theoretical density functional theory (DFT) modeling²⁷ as well as experimental procedures.^{28,29} The balanced reactions are shown below:



Through analysis in the GC, the only gaseous product observed with all three anodes was carbon dioxide originating from the unzipping of the PFOA molecule. The fluoride ion selective electrode did not detect any fluoride ions in the anode or cathode compartment nor any HF. No other fluorinated species were detected in the ¹⁹F NMR, so the fluorinated degradation products are yet to be determined. The limitation with ¹⁹F NMR is the detection limit is low in the 10 ppm regime so lower concentrations of degradation products may not be observed.

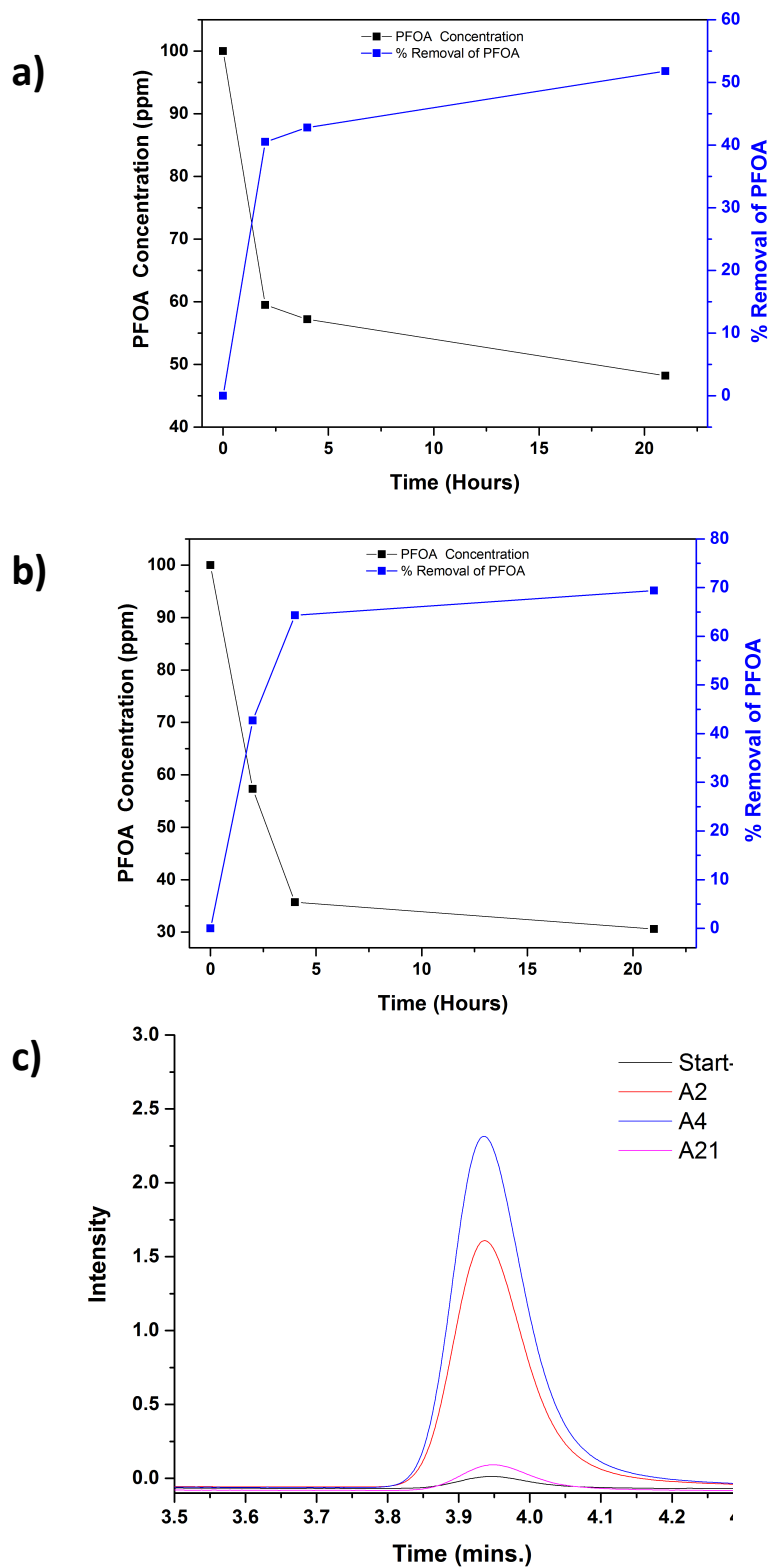


Figure 5.3 Results from electrochemical oxidation of 100 ppm PFOA in 0.1M Na₂SO₄ at a potential of 1.92V vs. Ag/AgCl using platinum for 21 hours by ¹⁹F NMR using liquid aliquot from a) working electrode compartment, b) counter electrode compartment, and c) gas chromatography of the headspace on the working electrode compartment.

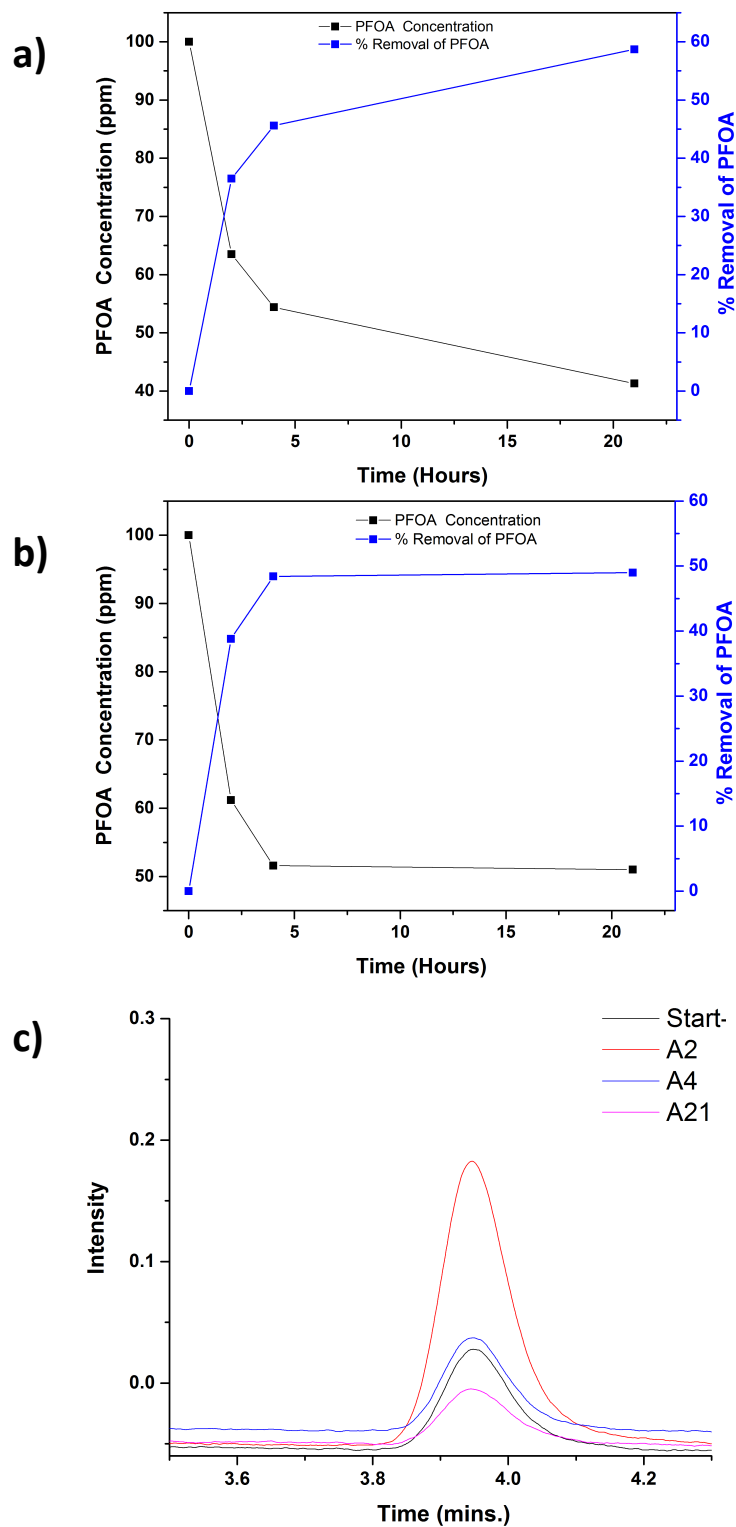


Figure 5.4 Results from electrochemical oxidation of 100 ppm PFOA in 0.1M Na₂SO₄ at a potential of 1.60V vs. Ag/AgCl using nickel for 21 hours by ¹⁹F NMR using liquid aliquot from a) working electrode compartment, b) counter electrode compartment, and c) gas chromatography of the headspace on the working electrode compartment.

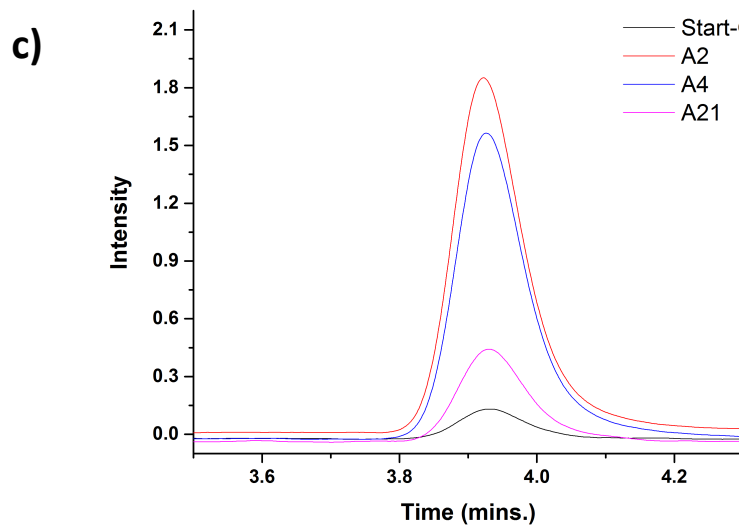
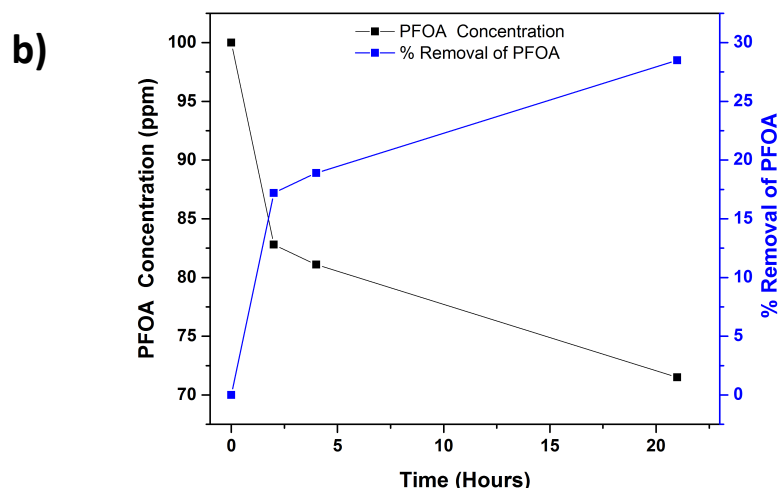
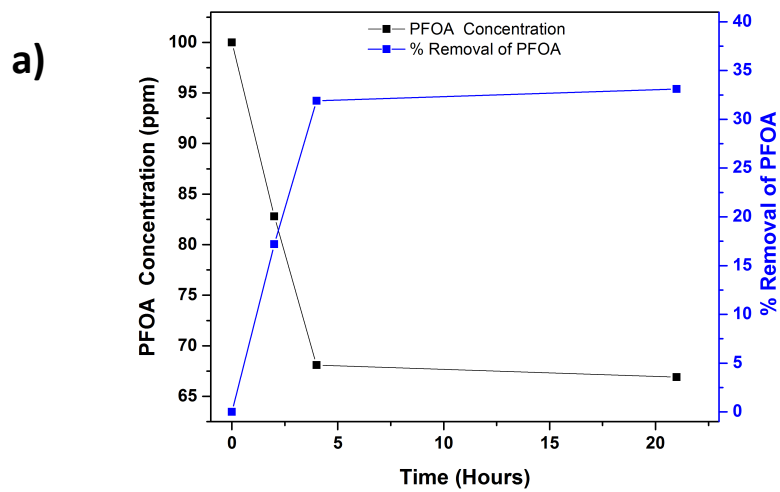


Figure 5.5 Results from electrochemical oxidation of 100 ppm PFOA in 0.1M Na₂SO₄ at a potential of 2.30V vs. Ag/AgCl using glassy carbon for 21 hours by ¹⁹F NMR using liquid aliquot from a) working electrode compartment, b) counter electrode compartment, and c) gas chromatography of the headspace on the working electrode compartment.

pH Effect on Preliminary PFOA Degradation

Since PFOA degradation was high using platinum and nickel as anodes, these two metals were tested at an increased pH of 5.1. Increasing pH is known to favor the oxygen evolution reactions of these metals as well as increase the amount of PFOA anion in solution.²¹ From **Figure 5.6** we observe that at pH 5.1 the PFOA was no longer detected in the anode or cathode compartment using platinum meaning 100% degradation of PFOA was observed. Meanwhile from **Figure 5.7** we observe that with nickel 100% degradation was observed at the cathode compartment and only 46.2% in the anode compartment. At higher pH the oxidation of nickel to generate Ni^{2+} ions is reduced.³⁰ Therefore at higher pH indirect PFOA oxidation via $\text{OH}\cdot$ is more likely than direct oxidation at anode.¹⁵ pH affects the degradation of PFOA due to the reactivity of the H^+ and OH^- ions in solution.³¹ Previous work has shown that electrochemical oxidation is preferred at an acidic pH.^{32,33} The acid dissociation constant (pKa) of PFOA is 0.5-3.8 so when the pH is 4 the molecule is in equilibrium with the carboxylate anion as shown in **Figure 5.8**.³⁴ As pH increases the equilibrium shifts to the right producing more anions in solution. When the pH becomes alkaline the OH^- ions in solution are likely to adsorb on the surface of the anode due to electrostatic interactions and this will hinder the surface area of active sites available to degrade PFOA.³⁵ This would explain why at a higher pH the amount of CO_2 produced was not the highest in the initial two hours since there were more competing OH^- ions than there were at pH 4.1. In contrast, if the pH of the solution is highly acidic it will produce excess amounts of H^+ ions and will hinder the production of the $\text{OH}\cdot$ needed for PFOA degradation.³⁶ Therefore the ideal pH for PFOA degradation is not extremely acidic or extremely alkaline rather a pH that is slightly higher than the pKa of PFOA (0.5-3.8) so as to minimize the concentration of H^+ ions in solution and generate enough $\text{OH}\cdot$ to increase PFOA degradation.

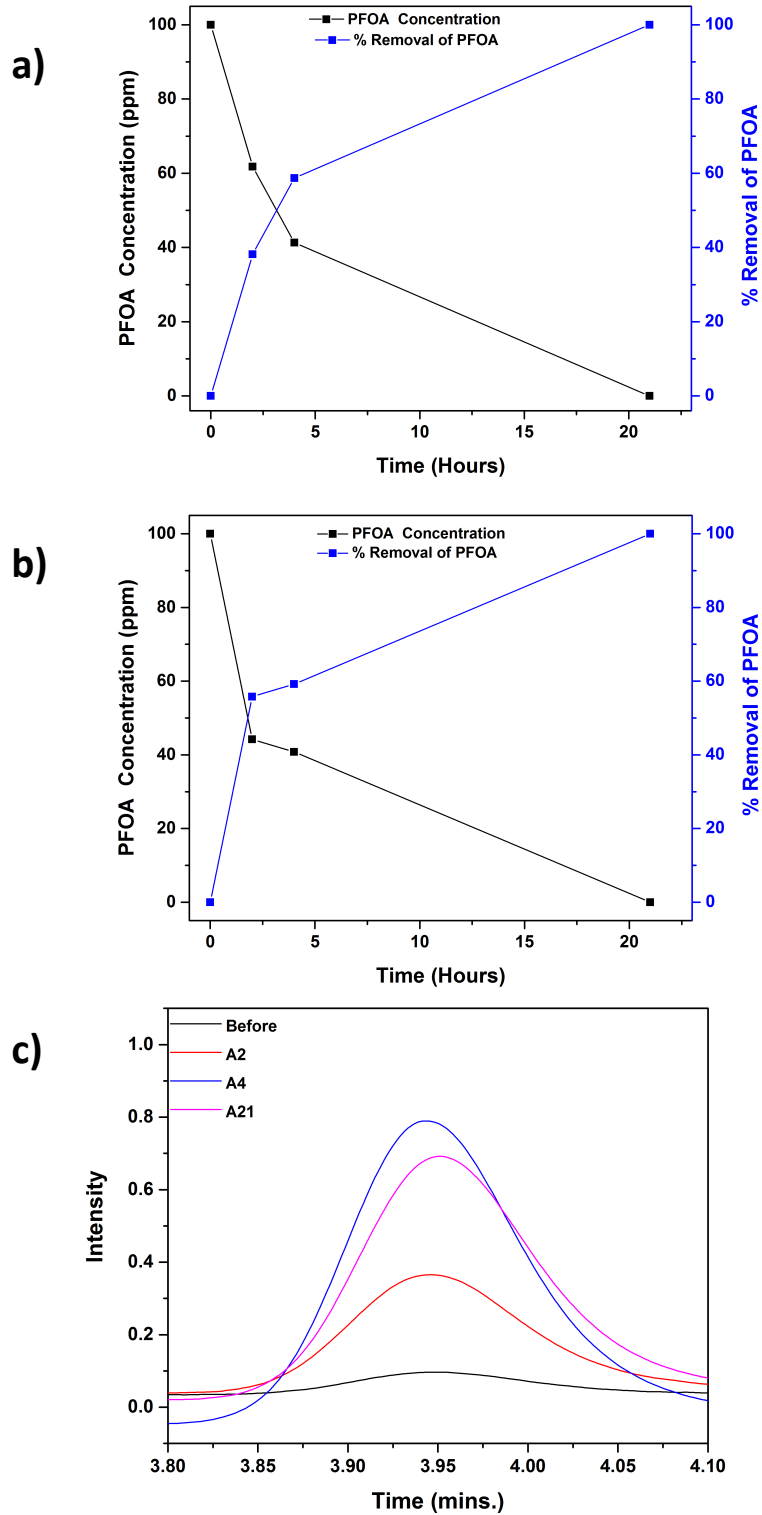


Figure 5.6 Results from electrochemical oxidation of 100 ppm PFOA in 0.1M Na₂SO₄ at a potential of 1.92V vs. Ag/AgCl at pH 5.1 using platinum for 21 hours by ¹⁹F NMR using liquid aliquot from a) working electrode compartment, b) counter electrode compartment, and c) gas chromatography of the headspace on the working electrode compartment.

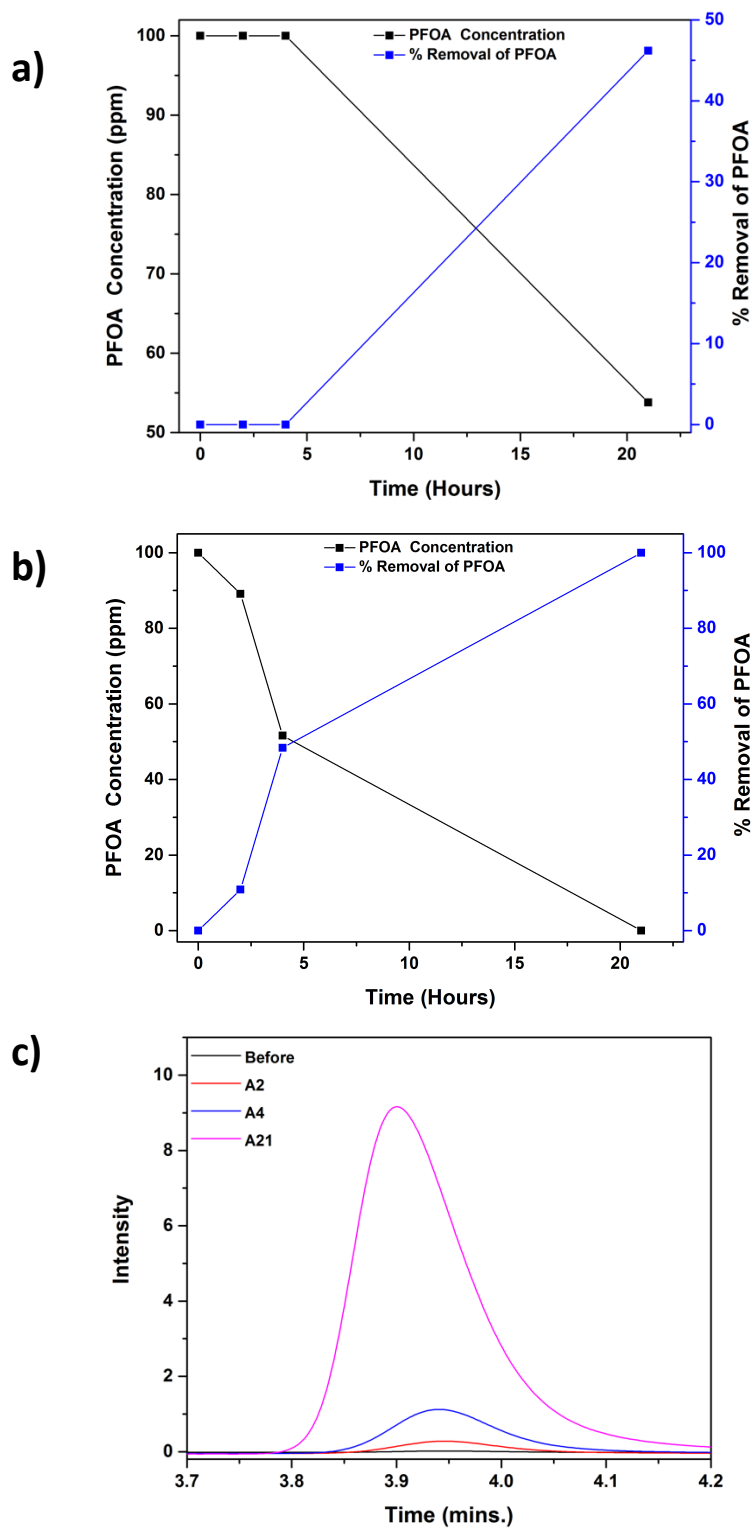


Figure 5.7 Results from electrochemical oxidation of 100 ppm PFOA in 0.1M Na₂SO₄ at a potential of 1.60V vs. Ag/AgCl at pH 5.1 using nickel for 21 hours by ¹⁹F NMR using liquid aliquot from a) working electrode compartment, b) counter electrode compartment, and c) gas chromatography of the headspace on the working electrode compartment.

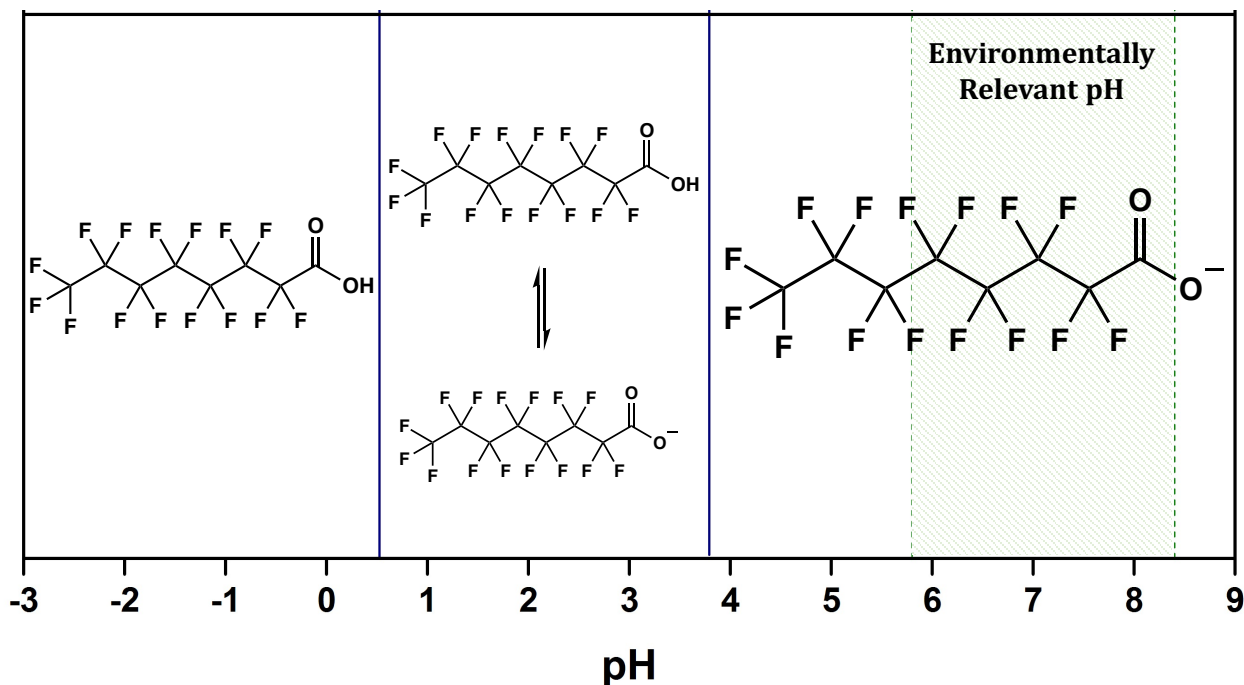


Figure 5.8 Description of PFOA molecule in solution as a function of pH. pK_a of PFOA is 0.5-3.8. At $\text{pH} < \text{pK}_a$ the molecule does not dissociate in solution, at $\text{pH} = \text{pK}_a$ the molecule is in equilibrium with the deprotonated anion, and $\text{pH} > \text{pK}_a$ the PFOA exists mostly as the deprotonated anion in solution.

As in the previous case, through analysis in the GC, the only gaseous product observed was carbon dioxide originating from the unzipping of the PFOA molecule. The fluoride ion selective electrode did not detect any fluoride ions in the anode or cathode compartment nor any HF. No other fluorinated species were detected in the ^{19}F NMR, so the fluorinated degradation products are yet to be determined. The limitation with ^{19}F NMR is the detection limit is low in the 10 ppm regime so lower concentrations of fluorinated degradation products may could not be detected.

Conclusions

In summary, this work aimed at benchmarking three anodes with different OER potentials for EO of PFOA. In terms of direct anodic oxidation of PFOA at pH 4.1 nickel had the highest removal efficiency at 58.7%, followed by platinum at 51.8%, and glassy carbon at 33.1%. As pH increases the amount of OH• available for PFOA electrochemical oxidation increases. Therefore at a pH of 5.1 using platinum as the anode 100% degradation of PFOA was observed at both the anode and cathode compartments. While using nickel at pH 5.1, 100% PFOA degradation was observed at the cathode and only 46.2% at the anode. This is due to the fact that at higher pH indirect oxidation of PFOA via OH• is more likely than direct oxidation at the anode. The gaseous degradation product detected was CO₂, however the fluorinated products could not be detected using current ¹⁹F NMR and Fluoride ion-selective electrode methods.

Future work for this project will involve developing more sensitive methods using LC-MS to detect fluorinated degradation products to be able to accurately determine the degradation mechanism. Through these preliminary results it would be possible to design future experiments that would allow us to take aliquots at shorter time intervals to determine the kinetics of the PFOA degradation. In addition, further method development is needed to determine quantitatively the amount of carbon dioxide produced.

Acknowledgements

I would like to acknowledge the California Department of Resources, Recycling, and Recovery (CalRecycle) award number DRR18040 for funding this project, and the University of California Davis for startup funding for this project. We would like to acknowledge support from the Cottrell Scholar program supported by the Research Corporation for Science Advancement (RCSA 26780) as well as the National Science Foundation Faculty Early Career Development program (DMR-2044403).

References

- 1 D. Renfrew and T. W. Pearson, The Social Life Of The “Forever Chemical,” *Environ. Soc.*, 2021, **12**, 146–163.
- 2 S. E. Fenton, A. Ducatman, A. Boobis, J. C. DeWitt, C. Lau, C. Ng, J. S. Smith and S. M. Roberts, Per- And Polyfluoroalkyl Substance Toxicity And Human Health Review: Current State Of Knowledge And Strategies For Informing Future Research, *Environ. Toxicol. Chem.*, 2021, **40**, 606–630.
- 3 K. Roth, Z. Imran, W. Liu and M. C. Petriello, Diet As An Exposure Source And Mediator Of Per- And Polyfluoroalkyl Substance (PFAS) Toxicity, *Front. Toxicol.*, , DOI:10.3389/ftox.2020.601149.
- 4 A. M. Temkin, B. A. Hocevar, D. Q. Andrews, O. V. Naidenko and L. M. Kamendulis, Application Of The Key Characteristics Of Carcinogens To Per And Polyfluoroalkyl Substances, *Int. J. Environ. Res. Public Health*, 2020, **17**, 1668.
- 5 S. Kurwadkar, J. Dane, S. R. Kanel, M. N. Nadagouda, R. W. Cawdrey, B. Ambade, G. C. Struckhoff and R. Wilkin, Per- And Polyfluoroalkyl Substances In Water And Wastewater: A Critical Review Of Their Global Occurrence And Distribution, *Sci. Total Environ.*, 2021, 151003.
- 6 Y. Li, T. Fletcher, D. Mucs, K. Scott, C. H. Lindh, P. Tallving and K. Jakobsson, Half-Lives Of PFOS, PFHxS And PFOA After End Of Exposure To Contaminated Drinking Water, *Occup. Environ. Med.*, 2018, **75**, 46–51.
- 7 C. Y. Tang, Q. S. Fu, A. P. Robertson, C. S. Criddle and J. O. Leckie, Use Of Reverse Osmosis Membranes To Remove Perfluorooctane Sulfonate (PFOS) From Semiconductor Wastewater, *Environ. Sci. Technol.*, 2006, **40**, 7343–7349.
- 8 H. Son, T. Kim, H.-S. Yoom, D. Zhao and B. An, The Adsorption Selectivity Of Short And Long Per- And Polyfluoroalkyl Substances (PFASs) From Surface Water Using Powder-Activated

- Carbon, *Water*, 2020, **12**, 3287.
- 9 P. Chularueangksorn, S. Tanaka, S. Fujii and C. Kunacheva, Adsorption Of Perfluorooctanoic Acid (PFOA) Onto Anion Exchange Resin, Non-Ion Exchange Resin, And Granular-Activated Carbon By Batch And Column, *Desalin. Water Treat.*, 2014, **52**, 6542–6548.
- 10 S. Huang and P. R. Jaffé, Defluorination Of Perfluorooctanoic Acid (PFOA) And Perfluorooctane Sulfonate (PFOS) By Acidimicrobium Sp. Strain A6, *Environ. Sci. Technol.*, 2019, **53**, 11410–11419.
- 11 T. F. Mastropietro, R. Bruno, E. Pardo and D. Armentano, Reverse Osmosis And Nanofiltration Membranes For Highly Efficient PFASs Removal: Overview, Challenges And Future Perspectives, *Dalt. Trans.*, 2021, **50**, 5398–5410.
- 12 Z. Liu, H. Meng, C. Li, T. Liu, J. Cao and Y. Lv, Catalytic Degradation Of Humic Acid By Mn-Cu/Al-MCM-41 Catalyst In Electro-Fenton/Chlorine Processes: Influencing Factors, Mechanisms, And Kinetics, *Water, Air, Soil Pollut.*, 2019, **230**, 230.
- 13 H. Lin, X. Zhong, C. Ciotonea, X. Fan, X. Mao, Y. Li, B. Deng, H. Zhang and S. Royer, Efficient Degradation Of Clofibric Acid By Electro-Enhanced Peroxydisulfate Activation With Fe-Cu/SBA-15 Catalyst, *Appl. Catal. B Environ.*, 2018, **230**, 1–10.
- 14 Y. Xu, E. Hu, D. Xu and Q. Guo, Activation Of Peroxymonosulfate By Bimetallic CoMn Oxides Loaded On Coal Fly Ash-Derived SBA-15 For Efficient Degradation Of Rhodamine B, *Sep. Purif. Technol.*, 2021, **274**, 119081.
- 15 S. Garcia-Segura, J. D. Ocon and M. N. Chong, Electrochemical Oxidation Remediation Of Real Wastewater Effluents — A Review, *Process Saf. Environ. Prot.*, 2018, **113**, 48–67.
- 16 B. N. Nzeribe, M. Crimi, S. Mededovic Thagard and T. M. Holsen, Physico-Chemical Processes For The Treatment Of Per- And Polyfluoroalkyl Substances (PFAS): A Review, *Crit. Rev.*

- Environ. Sci. Technol.*, 2019, **49**, 866–915.
- 17 C. S. Liu, C. P. Higgins, F. Wang and K. Shih, Effect Of Temperature On Oxidative Transformation Of Perfluorooctanoic Acid (PFOA) By Persulfate Activation In Water, *Sep. Purif. Technol.*, 2012, **91**, 46–51.
- 18 S. Sukeesan, N. Boontanon and S. K. Boontanon, Improved Electrical Driving Current Of Electrochemical Treatment Of Per- And Polyfluoroalkyl Substances (PFAS) In Water Using Boron-Doped Diamond Anode, *Environ. Technol. Innov.*, 2021, **23**, 101655.
- 19 B. P. Chaplin, The Prospect Of Electrochemical Technologies Advancing Worldwide Water Treatment, *Acc. Chem. Res.*, 2019, **52**, 596–604.
- 20 J. Qiao and Y. Xiong, Electrochemical Oxidation Technology: A Review Of Its Application In High-Efficiency Treatment Of Wastewater Containing Persistent Organic Pollutants, *J. Water Process Eng.*, 2021, **44**, 102308.
- 21 C. C. L. McCrory, S. Jung, I. M. Ferrer, S. M. Chatman, J. C. Peters and T. F. Jaramillo, Benchmarking Hydrogen Evolving Reaction And Oxygen Evolving Reaction Electrocatalysts For Solar Water Splitting Devices, *J. Am. Chem. Soc.*, 2015, **137**, 4347–4357.
- 22 S. A. Francis, J. M. Velazquez, I. M. Ferrer, D. A. Torelli, D. Guevarra, M. T. McDowell, K. Sun, X. Zhou, F. H. Saadi, J. John, M. H. Richter, F. P. Hylar, K. M. Papadantonakis, B. S. Brunshwig and N. S. Lewis, Reduction Of Aqueous CO₂ To 1-Propanol At MoS₂ Electrodes, *Chem. Mater.*, 2018, **30**, 4902–4908.
- 23 S. Kumari and R. N. Kumar, River Water Treatment Using Electrocoagulation For Removal Of Acetaminophen And Natural Organic Matter, *Chemosphere*, 2021, **273**, 128571.
- 24 E. B. Cavalcanti, S. G. -Segura, F. Centellas and E. Brillas, Electrochemical Incineration Of Omeprazole In Neutral Aqueous Medium Using A Platinum Or Boron-Doped Diamond Anode:

- Degradation Kinetics And Oxidation Products, *Water Res.*, 2013, **47**, 1803–1815.
- 25 F. Ghanbari and C. A. Martínez-Huitle, Electrochemical Advanced Oxidation Processes Coupled With Peroxymonosulfate For The Treatment Of Real Washing Machine Effluent: A Comparative Study, *J. Electroanal. Chem.*, 2019, **847**, 113182.
- 26 C. Fang, M. Megharaj and R. Naidu, Electrochemical Advanced Oxidation Processes (EAOP) To Degrade Per- And Polyfluoroalkyl Substances (PFASs), *J. Adv. Oxid. Technol.*, , DOI:10.1515/jaots-2017-0014.
- 27 J. Niu, H. Lin, C. Gong and X. Sun, Theoretical And Experimental Insights Into The Electrochemical Mineralization Mechanism Of Perfluorooctanoic Acid, *Environ. Sci. Technol.*, 2013, **47**, 14341–14349.
- 28 Q. Zhuo, S. Deng, B. Yang, J. Huang, B. Wang, T. Zhang and G. Yu, Degradation Of Perfluorinated Compounds On A Boron-Doped Diamond Electrode, *Electrochim. Acta*, 2012, **77**, 17–22.
- 29 S. Barisci and R. Suri, Electrooxidation Of Short And Long Chain Perfluorocarboxylic Acids Using Boron Doped Diamond Electrodes, *Chemosphere*, 2020, **243**, 125349.
- 30 H. Kim, D. B. Mitton and R. M. Latanision, Effect Of PH And Temperature On Corrosion Of Nickel-Base Alloys In High Temperature And Pressure Aqueous Solutions, *J. Electrochem. Soc.*, 2010, **157**, C194.
- 31 F. Wang and K. Shih, Adsorption Of Perfluorooctanesulfonate (PFOS) And Perfluorooctanoate (PFOA) On Alumina: Influence Of Solution PH And Cations, *Water Res.*, 2011, **45**, 2925–2930.
- 32 Y. Cong and Z. Wu, Electrocatalytic Generation Of Radical Intermediates Over Lead Dioxide Electrode Doped With Fluoride, *J. Phys. Chem. C*, 2007, **111**, 3442–3446.
- 33 C. A. Martínez-Huitle, M. A. Quiroz, C. Comninellis, S. Ferro and A. De Battisti, Electrochemical

- Incineration Of Chloranilic Acid Using Ti/IrO₂, Pb/PbO₂ And Si/BDD Electrodes, *Electrochim. Acta*, 2004, **50**, 949–956.
- 34 D. C. Burns, D. A. Ellis, H. Li, C. J. McMurdo and E. Webster, Experimental P K A Determination For Perfluorooctanoic Acid (PFOA) And The Potential Impact Of P K A Concentration Dependence On Laboratory-Measured Partitioning Phenomena And Environmental Modeling, *Environ. Sci. Technol.*, 2008, **42**, 9283–9288.
- 35 Q. Zhuo, Q. Xiang, H. Yi, Z. Zhang, B. Yang, K. Cui, X. Bing, Z. Xu, X. Liang, Q. Guo and R. Yang, Electrochemical Oxidation Of PFOA In Aqueous Solution Using Highly Hydrophobic Modified PbO₂ Electrodes, *J. Electroanal. Chem.*, 2017, **801**, 235–243.
- 36 Q. Ma, L. Liu, W. Cui, R. Li, T. Song and Z. Cui, Electrochemical Degradation Of Perfluorooctanoic Acid (PFOA) By Yb-Doped Ti/SnO₂–Sb/PbO₂ Anodes And Determination Of The Optimal Conditions, *RSC Adv.*, 2015, **5**, 84856–84864.